Planetary geodesy: Application to the gravity of the Martian system and The formation of the Martian moons.

Pascal Rosenblatt

Mémoire présentée à l'Université de Nantes
en vue d'obtenir une
Habilitation à Diriger des Recherches

Par Pascal Rosenblatt

Planetary geodesy: Application to the gravity of the Martian system and The formation of the Martian moons.

Soutenue le 25 janvier 2021 devant le jury composé de :

M. Christophe Sotin, Professeur, président
Mme Isabelle Panet, Directeur de recherche, rapporteur
M. Alessandro Morbidelli, Directeur de recherche, rapporteur
Mme Marianne Greff, Professeure, rapporteur
M. Georges Balmino, Emérite, examinateur
Mme Doris Breuer, Professeure, examinatrice.

Foreword

This manuscript is a synthesis of two aspects of my research work performed over the last twenty years.

The first aspect concerns the application of the space geodesy concepts and techniques to the reconstruction of the motion of deep space probes orbiting or flying by planets or moons. I have focused the manuscript on orbiters around Mars, especially on the NASA's Mars Global Surveyor and Mars Odyssey as well as on the ESA's Mars Express spacecraft. I will synthetise the precise orbit determination performed with the tracking data of these spacecraft and emphasise on the results in terms of the internal structure of Mars and its moons, Phobos and Deimos.

The second aspect concerns the modeling of the formation of the Martian moons. It is an application of models of moons and planets formation to the formation of the Martian moon system. This is a pioneering effort, never done before, which has provided an outstanding contribution to our understanding of the formation of the two small satellites of Mars.

At the end of each of the two aspects, I suggest paths of investigations for continuing this work in relation with the opportunities of geodesy experiment offered by the missions of the solar system exploration launched, in preparation or yet to be selected for the ten years to come.

Remerciements

Tout le monde sait que la page la plus lue d'une thèse ou d'une HDR est celle des remerciements. On pourrait donc s'y appliquer avec encore plus d'attention que pour le reste du manuscrit. Cependant, je crois que cette page doit juste témoigner de la personnalité de l'auteur et des relations qu'il entretient avec ses collaborateurs. Ce qui est pour moi la clé de la réussite d'un travail de recherche.

Je voudrais d'abord remercier le jury qui a accepté avec enthousiasme de lire ce résumé de mes recherches, et pour certain(e)s de rédiger un rapport. Je remercie Christophe Sotin pour la présidence et aussi pour l'écoute dont il a fait preuve à quelques moments de ma carrière. Un merci spécial à Isabelle Panet et Marianne Greff pour avoir accepté de porter un regard critique et constructif sur des recherches qui ne portent pas directement sur notre bonne vieille Terre. Je remercie également Doris Breuer pour sa participation, apportant ainsi l'éclairage des principaux utilisateurs des produits de géodésie planétaire que ce sont les modélisateurs de l'intérieur des planètes. Un grand merci à Alessandro Morbidelli qui a pris le temps de m'expliquer le sujet passionnant de l'origine du système solaire et avec qui toute échange n'a été que bénéfique et sympathique. Enfin, je voudrais tout particulièrement remercier Georges Balmino qui est un des pères de la géodésie spatiale en France et que j'ai eu la chance de croiser à certains moments clés de ma carrière. Je me souviens en particulier de notre première rencontre durant mon stage de DEA. Ce qui ne date pas d'hier ! A cette époque je ne me doutais absolument pas que j'allais attraper le virus de la géodésie pour lequel il est vain d'essayer de trouver un vaccin.

Je remercie évidemment beaucoup de collègues fréquenté(e)s au fil des congrès, workshops, projets et collaborations. En tout premier lieu les géodésiens de Toulouse avec qui j'ai appris beaucoup (et je continue aujourd'hui). Ils m'ont transmis beaucoup de leur savoir et de leur expérience dans une ambiance des plus décontractées (idéale pour transmettre les savoirs, justement). Même si je suis loin de les avoir tous convertis au planétaire, ils restent mes contacts privilégiés pour m'aider à perfectionner la géodésie planétaire avec les dernières méthodes et techniques acquises en géodésie terrestre. Merci donc à Franck, Julien, Félix, Jean-Michel, Sylvain, bien sûr à Jean-Charles et Georges, à Richard (qui nous a quitté trop tôt) et à Sean. Je tiens aussi à remercier les deux Nicole pour leur aide tant technique qu'administrative et surtout leur constante bonne humeur.

Je tiens aussi à remercier les collègues du laboratoire de géodynamique et planétologie de Nantes tant pour leur richesse humaine que scientifique. Dans le désordre : Benoit, Gabie, Gaël, Stéphane, Olivier, Antoine, Yann, Sabrina, et bien d'autres. Je remercie tout spécialement Caroline. Notre collaboration est particulièrement efficace et réciproque. C'est en fait assez rare de tomber sur une telle collaboration dans notre métier. J'espère qu'on pourra continuer longtemps à former cette belle équipe (Caroline, je vais essayer de réduire mon empreinte carbone à l'avenir ☺). Je remercie tout particulièrement Antoine Mocquet pour son accueil au laboratoire et son soutien tout au long de ma carrière. Une telle confiance m'a souvent motivé et aidé à traverser les passes difficiles (et ça continue encore aujourd'hui).

La recherche est faite d'une myriade de disciplines et particulièrement dans des domaines d'exploration comme celui de l'évolution et de la formation du système solaire. Cela constitue une vraie richesse mais paradoxalement cela rend difficile la construction d'une collaboration fructueuse tant les disciplines diffèrent les unes des autres. J'ai néanmoins eu la chance de pouvoir bâtir une telle collaboration avec

Sébastien Charnoz. Nous nous sommes tout de suite entendus sur notre base commune en physique, ce qui nous a permis de jeter un regard neuf sur la question de la formation des lunes de Mars. J'ai ensuite eu la chance de voir s'étendre cette collaboration à d'autres collègues Japonais Hidenori et Ryuki ainsi que Rennais Mariko et Kevin provenant d'un tout autre domaine : la physique atomique. Mariko et Kevin sont aussi devenus des amis fidèles et je les remercie pour leur soutien inestimable. Dans cette aventure nous avons eu aussi l'aide enthousiaste et efficace d'Antony. Soit ici chaleureusement remercié, Antony, ainsi que pour tout ce qu'on nous avons partagé jusqu'à présent. Je remercie aussi Francesco pour sa contribution à cette investigation sur l'origine des lunes martiennes.

Je veux aussi remercier d'autres collaborateurs nationaux de longue date à l'observatoire de Paris (Valery, Christophe, Nicolas, William, Florent, …) pour le travail effectué sur certains projets et surtout pour toutes les idées partagées qui ne demandent qu'à aboutir au travers de nouveaux projets. Je remercie aussi nombres collègues croisés au sein du GRGS et avec qui j'ai enrichi ma 'géodésie'. Je tiens à remercier tout particulièrement Thomas Widemann qui m'a permis de rentrer dans le projet EnVision m'offrant l'opportunité de revenir sur mes premières amours (mais pouvait-il en être autrement avec Vénus ?). Les collaborations internationales sont toutes aussi importantes dans la recherche et elles offrent des échanges culturels enrichissants. J'ai fait mes premières armes avec le groupe de radio-science de Cologne et je les remercie de m'avoir permis de grandir professionnellement. J'ai ainsi pu travailler sur des projets de l'ESA (Mars Express et Venus Express) avec quelques-uns de ses ingénieurs et scientifiques, et parfois forger des collaborations durables comme avec Olivier Witasse. J'ai aussi pu échanger de nombreuses fois avec le JPL et le GODDARD de la NASA qui sont les laboratoires de référence en géodésie planétaire outre-Atlantique. Je me suis enrichi à leur contact. Parmi tous les chercheurs internationaux que j'ai rencontrés jusqu'à présent, Jim Head tient une place très particulière et importante. C'est pour moi l'incarnation de l'exploration scientifique qui constitue le véritable moteur de ma motivation pour la recherche. Many thanks Jim !

Je voudrais enfin terminer par trois personnes importantes sur un point tout aussi personnel que professionnel. Félix que j'ai rencontré sur les bancs de l'Université Paul Sabatier, qui est né la même année que moi, qui a soutenu sa thèse le même jour que moi et avec qui nous partageons de nombreuses valeurs, à commencer par le bon goût du sud-ouest et le rugby ☺. Merci Félix de me rappeler souvent ces valeurs fondamentales et accessoirement de me révéler tous les secrets du GNSS. Il y a aussi Jimmy avec qui nous avons respectueusement défiés Poséidon à bord de son bateau. Je me souviens spécialement d'une traversée en mer Egée par un Melten force 6 établi, par bâbord travers. Je m'appuie souvent sur son amitié et son savoir inestimable en géodésie spatiale. Merci Jimmy pour ton amitié sans faille ☺. Et enfin Jean-Charles. Nous avons eu la même formation de physicien à Paul Sabatier, ce qui m'a aidé à comprendre, et lui à m'expliquer, plus facilement les concepts compliqués de l'orbitographie terrestre et planétaire, et à me repérer dans les méandres du logiciel GINS. Je ne peux que le remercier jusqu'à la fin de ma carrière pour sa patience à cet égard (je te promets très bientôt, Jean-Charles, de suivre une formation en Unix et fortran90 afin que tu puisses enfin utiliser mes codes sans devoir les réécrire ☺). Jean-Charles est surtout un ami sans qui je n'aurais pas persévéré dans ce métier. Je n'ai peut-être pas assez de cette vie pour le remercier.

Bien entendu je remercie ma famille et mes nombres autres amis pour leurs soutiens permanents.

A la mémoire de Richard Biancale.

Table of content

1 Improving the determination of the gravity of the Martian system

1.1 Introduction

Planetary geodesy aims to measure the dynamical characteristics of planets, such as gravity field and proper motion (spin and orientation variations). Measurements are performed using space tools, and in particular spacecraft orbiting the planets or landing on its surface. These dynamical characteristics are the result of the evolution of the interior of the planet as well as of the mass exchanges between the surface and the atmosphere inducing seasonal variations of gravity and spin.

Mars is an interesting target for planetary geodesy since its interior structure is not well known in the absence of seismic data[1], and significant amounts of CO_2 are exchanged between the atmosphere and the polar caps over the seasons. Mars also has two natural satellites, Phobos and Deimos, whose origin remains mysterious. A better knowledge of their interior may also help to understand the processes and conditions prevailing at their formation.

The basic techniques of planetary geodesy are to precisely monitor the motion of spacecraft (orbiter or lander) in order to determine the dynamical parameters of the planet (and its moons). These parameters are then used to constrain the models of the planet inner structure and physical properties. I have applied these techniques to the ESA's and NASA's spacecraft sent to Mars over the last two decades. I summarise in the following sections my achievements mainly based on the publications [PR5], [PR10], [PR12], [PR13], [PR14], [PR22], [PR26], and [P14] (see Section 4).

1.2 How does gravity field perturb the orbital motion of a spacecraft?

The basic principle to determine the gravity field from space is to monitor the free fall motion of a spacecraft in the gravity field of the planet[2]. The gravity field is then determined from the precise reconstruction of the orbital motion (e.g. Balmino et al., 1982; Konopliv et al., 1999, 2006, 2016; Lemoine et al., 2001; Marty et al., 2009, Smith et al., 2012; Genova et al., 2016, 2019; Konopliv et al., 2020). The monitoring of the spacecraft motion is performed using the telemetry radio link between the spacecraft and deep space antennas located on the Earth. In order to understand how the gravity field is determined from the radio tracking of the spacecraft motion, it is first necessary to understand the gravity field perturbs the orbital motion of the spacecraft.

[1] The mission InSight landed on Mars surface in 2018 is presently performing the first recordings of Mars seismic waves.

[2] It is the same principle used by absolute gravimeters to measure the Earth's gravity on the ground.

1.2.1 Representation of the gravity field

The gravity field of a terrestrial planet is derived from its gravitational potential $U(\vec{r})$. This potential represents the sum of the mass distribution inside the planet weighted by a factor proportional to the inverse of the square of the distance to the point $P(\vec{r})$ located at the exterior of the body[3]. This distribution is mainly radial, since the planet is large enough to allow only modest lateral variations of internal mass. A convenient representation of the gravitational potential is thus in terms of a spherical harmonics series as follows (Eq. 1):

$$U(r,\varphi,\lambda) = \frac{GM}{r} + \frac{GM}{r}\sum_{l=2}^{\infty}\left(\frac{R}{r}\right)^{l}\sum_{m=0}^{m=l} P_{lm}(\sin\varphi)[C_{lm}\cos(m\lambda) + S_{lm}\sin(m\lambda)]$$

where G is the gravitational constant, M is the mass and R the equatorial reference radius of the planet, C_{lm} and S_{lm} are dimensionless harmonic coefficients of degree l and order m, the P_{lm} are the Legendre functions of the first kind (associated Legendre polynomials with m=0), and r, φ, λ are the spherical coordinates of the point P in a reference system fixed with respect to the planet. The gravity field generated by this sum of spherical harmonics potentials corresponds to a superposition of anomalies of different wavelengths at the surface of the sphere with a radius equal to the equatorial radius R (Figure 1). Each wavelength is given as the ratio between the perimeter of the sphere and the degree l. The associated spatial resolution is half of the wavelength.

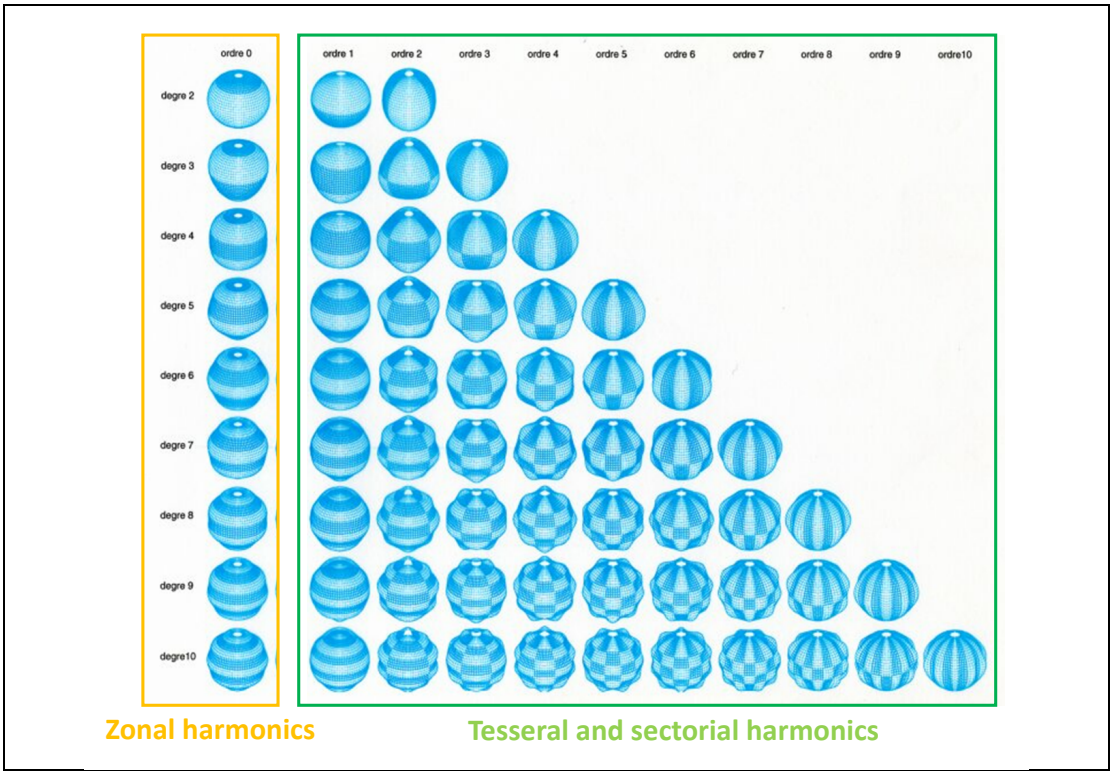

Figure 1 : Harmonics of the gravity field up to degree *l* and order *m* equal to 10. They are zonal for m=0, sectorial for m=l, otherwise tesseral.

[3] At any point P located outside the smallest sphere encompassing the entire mass distribution of the planet.

The first term in the right hand side of Eq. 1 represents the central term U_0 of the potential and the second term represents the perturbing potential U_p. This latter potential generates the velocity perturbations around the mean Keplerian orbital motion driven by the central term U_0 (see Appendix A)[4].

1.2.2 From the gravity field to the orbital velocity perturbations

The perturbations of the orbit (position and velocity) of the spacecraft can be assessed through the perturbations of the Keplerian or orbital elements. The Keplerian elements, shown in Figure 2, are the orbital plane inclination i and the longitude of the ascending orbital node Ω that gives the orientation of the orbital plane in space, the longitude of the periapsis ω giving the position of the ellipse within the orbital plane, the semi-major axis a and the eccentricity e corresponding to the size and the shape of the ellipse, and the mean anomaly M that places the spacecraft in the ellipse at any time (M is derived from the true anomaly v, see Appendix A). In the Keplerian motion only M varies with time and the spacecraft motion follows a perfect ellipse (see Appendix A).

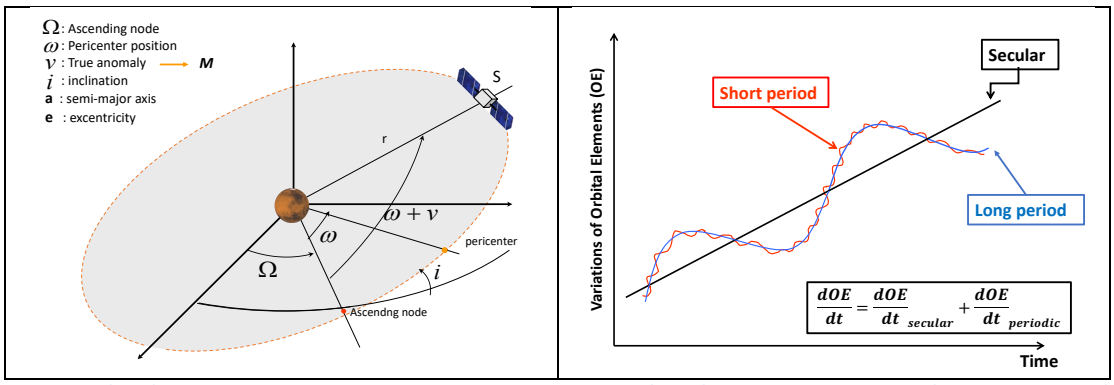

Figure 2 : (Left) orbital elements of the orbiting spacecraft and (right) their time variations (or perturbations) due to the gravitational potential of the planet (from Kaula's linear theory, see Annex B). The mean anomaly is obtained from the true anomaly (see Appendix A).

However, the non-sphericity of the planet and its non-uniform mass distribution vary the orientation, shape and position of this ellipse with time. As the gravity potential generates a conservative force, the Lagrange equations can be used in order to describe the variations of the orbital elements (see Appendix B). These equations have no analytical solutions, but to assess orbital perturbations with respect to the Keplerian motion, approximate solutions can be computed using perturbation theory. Kaula (1966) gave one of the most useful solutions. In his approach, the perturbing gravitational potential U_p is developed as a function of the Keplerian elements (see Appendix B), then introduced in the Lagrange equations that are solved in two steps: the first consists in solving for the secular variations and the second for the periodic variations of the orbital elements. These are shown superimposed to the secular solutions in Figure 2.

The secular variations correspond to the orbit precession, which induces a drift of the longitude of the ascending node Ω and of the periapsis ω as well as to some

[4] The Keplerian motion is the motion that the spacecraft would follow, if the planet was a sphere with uniform mass density.

extent of the mean anomaly *M* while the three others elements remain constant. The orbit precession is the major perturbation of the Keplerian motion. Only even zonal harmonics contribute to the secular variations of the orbital elements (see Annex B). On the other hand, periodic variations of the orbital elements manifest as small perturbations of the secular motion and affect all orbital elements. All gravitational harmonics contribute to these periodic variations. Their periods depend on the secular rates of the orbit precession and on the rotation rate of the planet, and their amplitudes are decreasing from longer to shorter periods (see Annex B).
From variations of orbital elements predicted by Kaula's linear theory, perturbations of the spacecraft velocity can be derived. An example is given in Figure 3 for Mars Global Surveyor (MGS) and Mars Odyssey (ODY) orbits (Table 1).

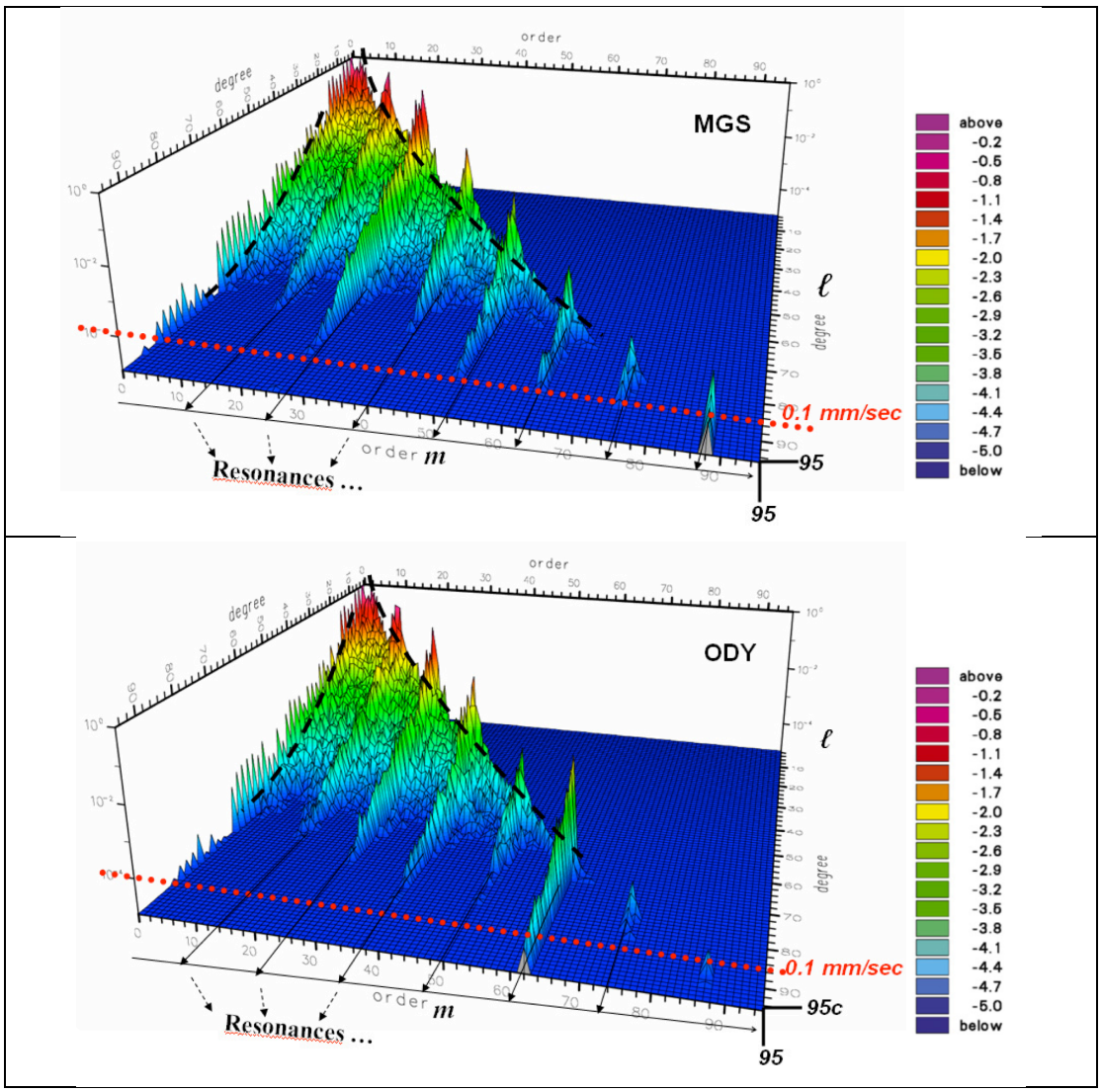

Figure 3 : Diagram of Mars gravity orbital effects on MGS and ODY (Kaula's linear theory), shown as velocity perturbations for pairs of C_{lm} and S_{lm}. The color scale corresponds to the decimal logarithm of the perturbation in m/s. The 0.1 mm/s dotted line corresponds to about twice the ultimate capabilities of the tracking system in X-band. Note the resonance bands which differ slightly between MGS and ODY as the order *m* increases, and the different perturbation amplitudes (adapted from Marty et al., 2009).

These velocity perturbations are of the order of a few mm/s and decrease with increasing degree and order (as depicted by the black dashed line in Figure 3), i.e. from long to short wavelength harmonics of the gravity field, due to the sharp decrease of the perturbing potential with increasing degree *l* (as $1/r^{(l+1)}$ in Eq.1). In addition, the

root mean square of pairs of C_{lm} and S_{lm} of degree l follows a A/l^2 power law with A depending on the planet, which is known as Kaula's law (Kaula, 1966).

Spacecraft	MGS	ODY	MRO	MEX
Altitudes (in kmxkm)	358x434	358x434	255x320	250x11500
Semi-major axis (in km)	3796	3796	3687	9355
Eccentricity	0.01	0.01	0.009	0.6
Inclination (in °)	92.9	93.1		86.5

Table 1: Orbital characteristics of MGS, ODY, MRO and MEX.

Kaula's theory can also be used to predict harmonics, which produce higher velocity perturbations at a particular degree l and order m. This corresponds to a phenomenon of 'resonance' involving the Ω, ω, and M secular rates and the rotation rate of the planet (see Appendix B). The few harmonics concerned by this phenomenon are clearly seen in Figure 3 at degree and order up to 90. It helps to define the maximum degree L for the spherical harmonics expansion (for instance, the solution using MGS tracking data are expanded up to degree 80 (Lemoine et al., 2001), and up to 95 (Konopliv et al., 2006; Marty et al., 2009) using additional ODY tracking data).

However, the velocity perturbations vanish for most harmonics after degree and order 60 (Figure 3), clearly showing that beyond, harmonic coefficients will be too affected by noise and therefore difficult to resolve[5]. This is expressed in the gravity solution as the degree strength (i.e. the degree beyond which the error on the gravity coefficients is larger than their values). The degree strength for Mars gravity solutions using MGS/ODY tracking data is about 60-70 (Lemoine at al., 2001; Konopliv et al., 2006; Marty et al., 2009).

The analytical solutions of the planetary Lagrange equations, such as Kaula's solution, shows how the orbital motion is perturbed by the harmonic coefficients of the gravity field. It emphasizes the importance of the orbit, which filters and resonates with several harmonics, so that each orbit senses differently the gravity field (Figure 3). From measurements of spacecraft velocity perturbations, harmonic coefficients C_{lm} and S_{lm} can be retrieved and the gravity field reconstructed given the mass and radius of the planet. A maximum degree L can in principle be reached, but the actual resolvable harmonics (degree strength) is lower and depends on the performance of the monitoring or tracking system (accuracy and spatial coverage).

1.2.3 From the orbital velocity perturbations to the gravity field

Based on Kaula's theory, one can perform a variance-covariance analysis of the gravity solution obtained by measuring spacecraft velocity perturbations. This analysis needs to compute the partial derivatives of the orbital velocity with respect to the harmonic coefficients C_{lm} and S_{lm} (Balmino and Perosanz, 1995). Assuming that the three components of the velocity are measured with the same accuracy and with a spatial coverage paving the entire surface of the planet, the theoretical uncertainty on each harmonic coefficient recovery can be computed. These assumptions are not

[5] The solution of Kaula also shows that each secular and each periodic perturbation does not depend on a single gravity harmonic but on a linear combination of several degree and order harmonics (called *lumped* harmonics, see Annex B). Therefore, given orbital characteristics, it is difficult to properly separate each harmonic, especially at high degree where the velocity perturbations are close to the precision of the velocity measurements (SNR=1).

realistic with regard to the tracking Doppler system (see section 1.3.3) but the quality of the gravity solution can be estimated as a function of the spacecraft orbit and the accuracy of the velocity measurements.

An example of this analysis is given in Figure 4 for the case of a Martian orbiter with a circular orbit at different altitudes. In this simulation an error of 0.05 mm/s is assumed for the velocity measurements. The degree strength corresponds to the intersection between the expected power spectrum of the gravity harmonics (A/l^2 Kaula's law) and the spectrum of the error (theoretical uncertainty). The dependency between the gravity field resolution and the orbital altitude is clearly visible: the lower the altitude, the better the spatial resolution. As a consequence, the spatial resolution of a gravity field solution varies at the surface of the planet according to the altitude the spacecraft above each latitude and longitude.

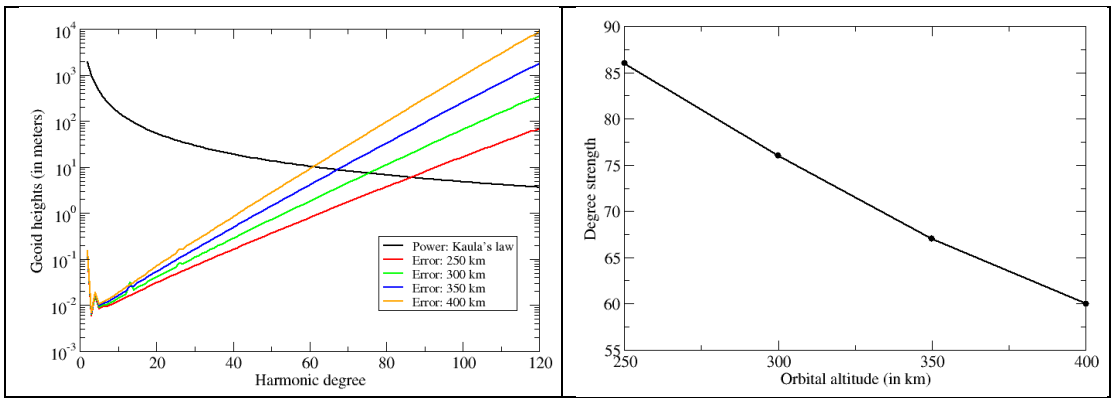

Figure 4 : Variance-covariance analysis of gravity field solutions obtained from velocity perturbation measurements: (left) expected power spectra (Kaula's law) and error spectra per harmonic degree for different orbital altitudes (250 to 400 km), (right) degree strength vs orbital altitude. Courtesy MANEGE CNES software.

However, Kaula's linear theory is an approximation and is not precise enough to process real measurements of velocity perturbations by Doppler tracking. In addition, this tracking is not continuous and orbits can be perturbed by other forces too. This is why a numerical approach is necessary to process the Doppler tracking data and derive gravity field solutions. It consists of numerically integrating the motion of the spacecraft taking into account all the forces driving the orbital motion, of computing Doppler tracking predictions, and of performing a least-squares fit of these predictions to real Doppler tracking data in order to derive the best gravity field solution. This process is called Precise Orbit Determination (POD) (see section 1.4) and relies on implementing a gravity experiment (see section 1.3).

1.3 How is a gravity experiment implemented?

A gravity experiment basically relies on recording at ground stations the carrier frequency of the radio signal sent by the spacecraft. Precise Doppler shift measurements of this frequency are performed by comparing the received frequency with a very stable reference frequency. The Doppler shift is then used to precisely reconstruct the spacecraft velocity perturbations. To ensure the required stability of the reference frequency, the radio link is a two-way link from the station to the spacecraft and back to the station (Figure 5). The experiment has a space segment aboard the spacecraft and a ground segment at the ground station.

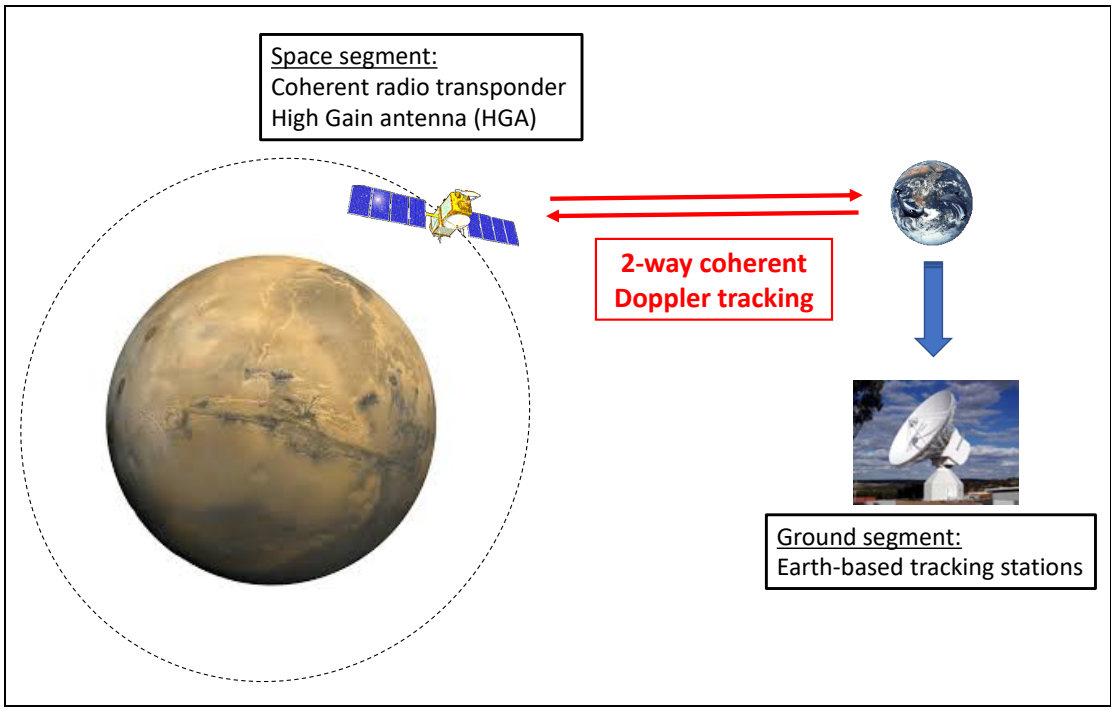

Figure 5 : Schematic representation of a planetary gravity experiment

1.3.1 Space segment

The stable reference frequency is produced at the ground station using atomic clocks and sent to the spacecraft via an uplink. To preserve this stability a dedicated electronic device, called coherent radio transponder, is onboard the spacecraft. This device receives the uplink frequency and generates the downlink frequency without modifying its phase[6]. A radio transponder is always aboard interplanetary spacecraft in order to perform radio navigation. A two-way link can thus always be established generally using X-band frequency on both uplink (7.2 GHz) and downlink (8.4 GHz)[7]. A parabolic High-Gain-antenna (HGA) tied to the spacecraft is used to receive the radio signal sent from Earth and to re-emit it back to Earth after passing through the radio transponder.

Spacecraft can also have an accurate clock device (called Ultra-Stable Oscillator, USO) that provides a stable reference frequency to perform radio-occultation of the atmosphere[8] (e.g. Liou et al., 2010). If the stability of the USO is as good as that required for radio transponders, tracking can be performed to determine gravity field.

[6] The stability of the radio transponder is expressed in terms of Allan Deviation (ADEV). For interplanetary spacecraft, it is better than 10^{-13} over 1 to 1000 seconds, meaning that the uplink frequency is kept with relative fluctuations lower than this ADEV value.

[7] Most recent missions like NASA's Cassini mission as well as ESA's Bepi-Colombo and JUICE missions have an additional radio transponder using Ka-band (uplink at 32 GHz and downlink at 34 Ghz) to perform very accurate Doppler measurements (Iess et al., 2014).

[8] In this case, the Doppler shift of the radio-signal propagating through the planetary atmosphere is dominated by the variations of the refractive index of this atmosphere. In turn, the Doppler measurements are used to determine this refractivity index from which profiles of temperature and pressure in the neutral atmosphere as well as of electron density in the ionosphere are derived.

The reference frequency is then generated aboard the spacecraft and driven by the USO. The tracking is performed in one-way mode since only the downlink is used. Such tracking has been successfully used for determining Mars gravity field with the MGS spacecraft (e.g. Lemoine et al., 2001; Konopliv et al., 2006, Marty et al., 2009; Genova et al., 2016).

1.3.2 Ground segment

The ground segment corresponds to Earth-based tracking stations. These are parabolic antennas dedicated to the tracking of deep space probes in the solar system[9] (Figure 6). The Deep Space Network (DSN) has been built by NASA as early as 1958 October 1st, and is still in development and improvement. The DSN currently comprises three sites well distributed in longitude in order to establish a radio-link with spacecraft at any time (Figure 6). Each site has several stations, most having a parabola dish with a diameter of 34 meters while one has a diameter of 70 meters[10] to process radio-signals with very low signal-to-noise ratio (strongly attenuated when propagating through planetary atmosphere or over very long distance throughout the solar system).

At the dawn of the twenty-first century, the European Space Agency (ESA) built its own network (Figure 6), named ESTRACK[11], in order to cover its own missions (MEX, VEX, Rosetta). Today, this network has three sites to continuously track any spacecraft in the solar system. Each ESTRACK site has one parabolic dish of 35 meters for deep space operations. This network is permanently updated and equipped for example by incorporating the Ka-band capability needed by the Bepi-Colombo and JUICE missions. Both ESA and NASA networks often collaborate to manage the numerous missions, especially for Mars (Holmes et al., 2008).

The downlink signal is received by the antennas and processed using a closed-loop device to remain lock on the downlink frequency to track the spacecraft as long as it can be viewed in the sky of the station. This device however requires a strong enough radio signal (at least 3 dB) to work. For lower level signals the station can record the phase of the radio signal in open-loop mode. In this case, the station does not provide the Doppler shift and the user must process the open-loop phase data autonomously. Software are available such as recently developed by the JIVE team using radio telescopes (Bocanegra-Bahamon et al., 2018).

[9] https://deepspace.jpl.nasa.gov
[10] Originally designated in the framework of the Apollo program
[11] https://www.esa.int/Enabling_Support/Operations/Estrack/Estrack_ground_stations

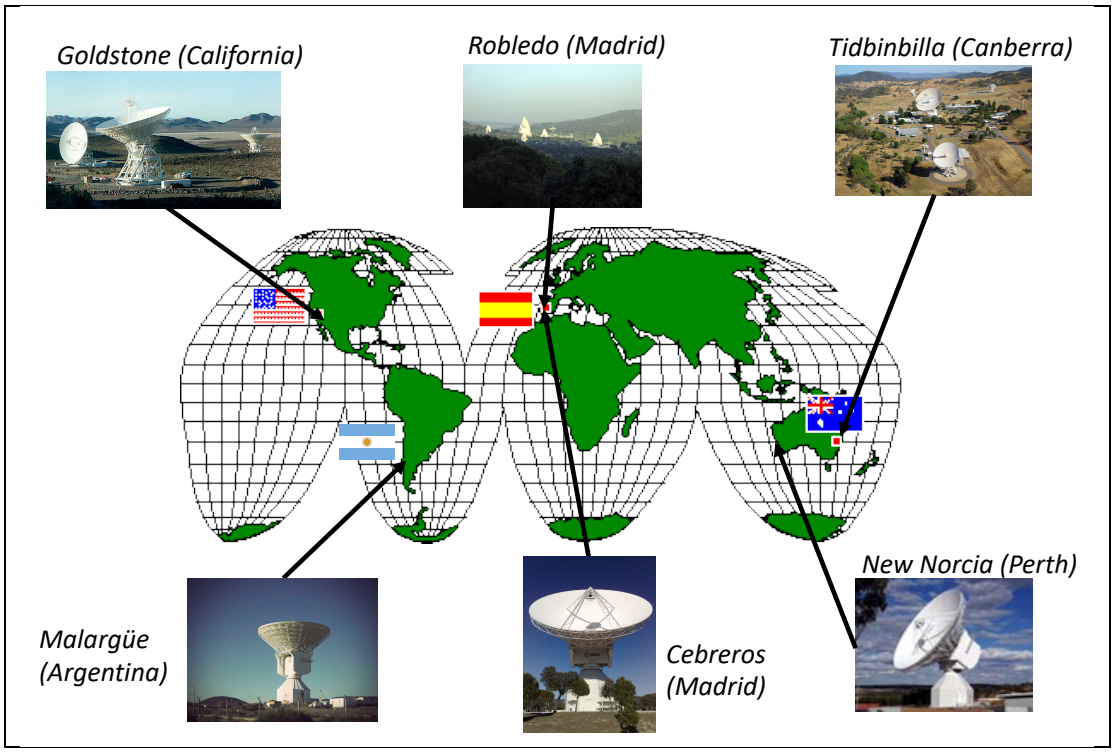

Figure 6: NASA's Deep Space Network (DSN) and ESA's ESTRACK network.

There are also deep space tracking stations located in one single country: The Soviet Deep Space Network[12] managed by the Russian space agency (ROSCOSMOS), the ISTRAC (ISRO Telemetry Tracking and Command Network)[13] managed by the Indian Space Research Organisation (ISRO), the Chinese Deep Space Network managed by the China Satellite Launch and Tracking Control (CLTC)[14], and the Usuda Deep Space Center[15] managed by the Japanese Aerospace Exploration Agency (JAXA). As of 2017, the CLTC was constructing an additional station in Argentina to extend the longitude coverage of its own network.

1.3.3 The tracking data

The Earth-based stations record the phase of the radio signal sent by the spacecraft, and the Doppler frequency shift is derived by counting the accumulation of the phase of this signal over a given count-time, called Doppler count time. A useful model of these Doppler tracking data can be found in Moyer (2000)[16].

Since the noise in the Doppler shift measurements increases for shorter count time, a trade-off must be found with the required gravity field resolution, especially the short period orbital perturbations due to the high degree harmonics. This count time is typically 10 seconds for the tracking of modern spacecraft orbiting terrestrial planets.

The Figure 7 is an example of the expected Doppler frequency shift of the radio link between a Martian spacecraft (with an MGS-like orbit, see Table 1) and a ground

[12] https://en.wikipedia.org/wiki/Soviet_Deep_Space_Network
[13] https://www.isro.gov.in/isro-telemetry-tracking-and-command-network-istrac-supports-astrosat-mission
[14] https://en.wikipedia.org/wiki/Chinese_Deep_Space_Network
[15] https://global.jaxa.jp/about/centers/udsc/index.html
[16] I invite any future user of tracking data to carefully read it.

station. The largest variations (peak-to-peak amplitude of 2×10^6 Hz) are actually due to the relative motion between the Earth and Mars. These variations can however be modeled with enough precision for Doppler shifts using planetary ephemerides. The gravity information is contained in lower frequency shift variations of up to 200 kHz (peak-to-peak) corresponding to a mean orbital velocity of the order of 3.4 km/s (MGS-like orbit, Table 1).

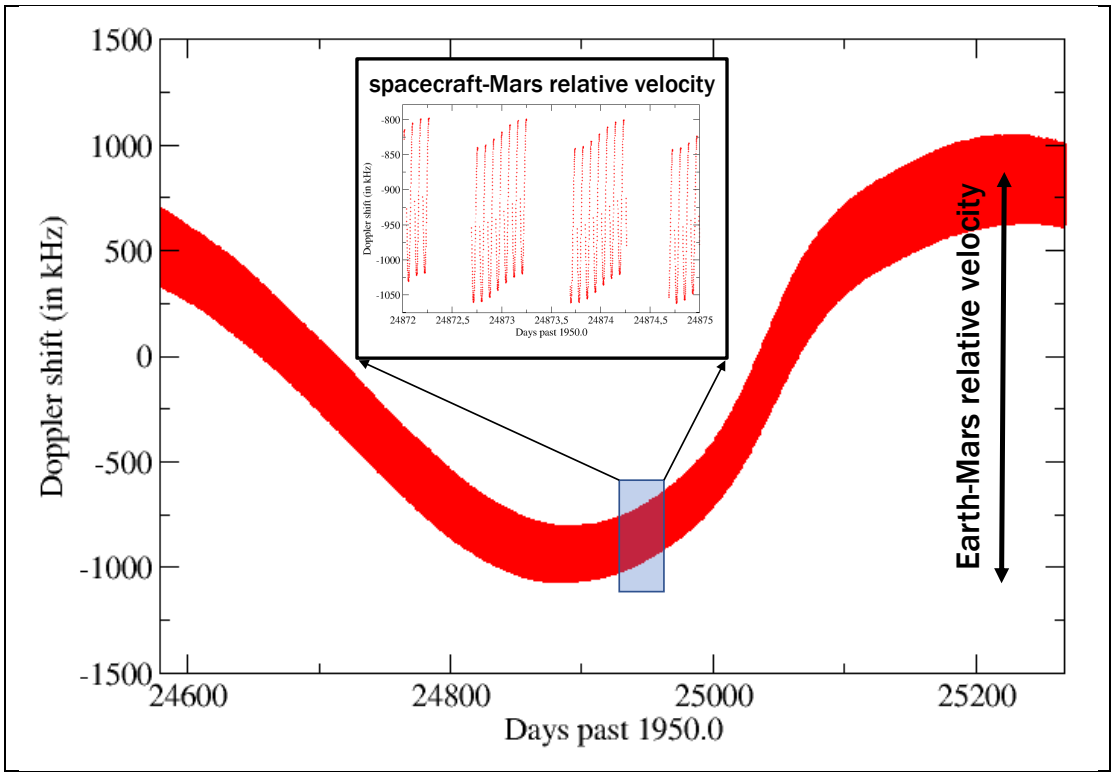

Figure 7: Predictions of Doppler frequency shift between a Martian spacecraft and a ground station (for a two-way link in X-band). The prediction runs over one Martian year.

The sources of noise on 2-way Doppler measurements are the radio link budget, the stability of the spacecraft transponder, the propagation through the Earth's troposphere, through the interplanetary or solar plasma and Earth's ionosphere, the frequency stability of the ground system transmitting and receiving the radio signal and mechanical noise of the ground antenna (e.g. Iess et al., 2014). The propagation noise (plasma and ionosphere) corresponds to dispersive effects on the phase due to fluctuations of the number of charged particles (phase scintillation, Ho et al., 2008) and to non-dispersive effects in the troposphere.

Each contribution to the noise budget has been computed using the best knowledge of these different sources of noise and compared with the 2-way X/X Doppler noise of the Rosetta spacecraft (Figure 8). It is found that the noise is dominated by the solar plasma contribution, which is larger than 0.1 mm/s around conjunction when the Sun is between the planet and the Earth (i.e. Sun-Earth-Probe, SEP, angles lower than about 15°, Figure 8). As a consequence, Doppler tracking data become useless for gravity purposes during periods of typically one month around the solar conjunction. The conjunction events repeat at each synodic period (Table 2)[17].

[17] The synodic period is the time required to retrieve the same Sun-Earth-Planet configuration. It is the composition of the revolution period of the Earth and of the planet.

Planet	Mercury	Venus	Mars
Synodic period (in Earth's year/day)	0.317 / 115,78	1.599 / 584	2.135 / 779.81

Table 2: The synodic period of the three terrestrial planets as viewed from the Earth.

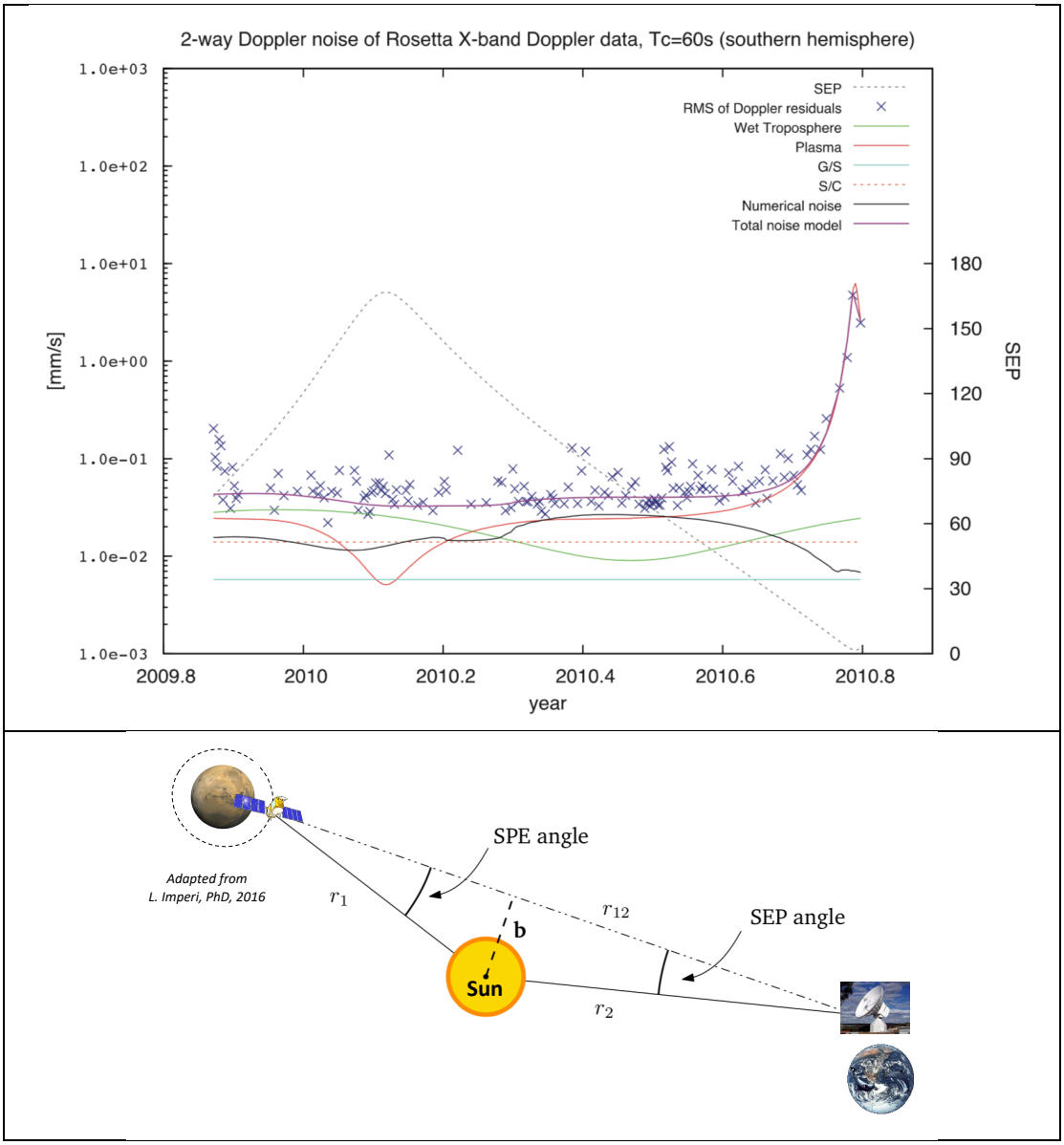

Figure 8: (top) breakdown of the Doppler noise budget compared with the Doppler noise of the 2-way X/X Doppler link of the Rosetta spacecraft (Iess et al., 2014). This is the noise level before any calibration is applied, (bottom) definition of Sun-Earth-Probe (SEP) angle and Sun-Probe-Earth (SPE) angle.

At larger SEP angles, tropospheric noise dominates (Figure 8), creating a delay of propagation of the radio-wave. This delay amounts to about 2 meters (in the zenith direction) and depends on temperature, pressure and humidity along the propagation path. The humidity contribution can reach 20 cm and depends on the season and location on Earth. The tropospheric noise increases as the spacecraft (or the planet) approaches the horizon of the site of the station since the radio-signal propagates through more atmosphere (0.035 mm/s and 0.06 mm/s at 60° and 30° elevation, respectively, Lee, 2002). This effect does not depend on the frequency band since the troposphere is a non-dispersive media.

The propagation noises must be calibrated as accurately as possible for POD and gravity field determination. The model used in Figure 8 provides the variance of the noise on the Doppler but not the value of the correction to apply. One method to calibrate solar plasma noise is to use higher frequencies since it is inversely proportional to the square of the frequency (DSN note 202, 2019). However, the radio transponder system onboard the spacecraft does not receive Ka-band uplink. Therefore, a Ka/Ka band radio transponder was developed (e.g. Iess et al., 2014) and carried onboard the Cassini, Bepi-Colombo and JUICE spacecraft in addition to the classical X/X radio transponder. The troposphere source of noise can be partly calibrated using either atmosphere measurements at the ground station[18] or meteorological models (Marty et al., 2009). An accurate calibration can be obtained using Media Calibration System using GNSS receivers at ground station (e.g. Bar-Sever et al., 2007; Graziani et al., 2013). The wet component however requires accurate calibration, especially when using Ka-band, since it becomes the dominant source of noise (Figure 8). It is performed using a dedicated Water Vapour Radiometer (WVR) at the station (e.g. Bar-Sever et al., 2017).

For a Doppler count time of 60 seconds, the end-to-end two-way X/X Doppler noise is 0.02 mm/s (Zuber et al., 2007) (or 0.05 mm/sec for 10 second count time)[19]. It is improved by a factor of two (0.01 mm/sec at 60 seconds) using an additional Ka/Ka link (Iess et al., 2014). Further investigations are being performed to calibrate the mechanical noise of the ground antenna caused by differential thermal dilatation or vibration of the large antenna structure (Notaro et al., 2020). This mechanical noise is just below 0.01 mm/s (ESOC pers. Comm., 2019) and becomes the leading source of noise after the best calibration of the propagation effects is performed.

The tracking station can also perform ranging measurements with the spacecraft (Moyer, 2000). These data have a precision better than 1 meter but they can be biased by 2-3 meters due to uncalibrated delays in the wires at the station. They are used to constrain the planetary ephemerides[20] (see also Section 1.4).

1.3.4 The orbit and tracking requirements for mapping the gravity field

The sections 1.2.2 and 1.2.3 have shown the importance of the orbital altitude to get a highly resolved gravity field. The spacecraft orbit has also to pave the entire sphere with a spatial sampling corresponding to the targeted spatial resolution. This sampling has to be even denser than the spatial resolution because the spacecraft velocity is perturbed not only by gravity anomalies just beneath the orbital track (along-track anomalies) but also by cross-track anomalies, which results in a mixing of different wavelengths (Beuthe et al., 2006) that prevents proper separation of each high degree harmonic. I found empirically, by simulating the EnVision gravity experiment, that the spatial sampling should be at least half the targeted spatial resolution to avoid this mixing among short wavelengths of the gravity field. In addition, to reach the expected resolution, tracking must be continuous, which is never the case since the spacecraft is

[18] Temperature, pressure and humidity measurements.
[19] The Doppler noise at 10 seconds can be deduced by multiplying the noise at 60 seconds by a factor equal to the square root of 60/10 (Genova et al., 2016).
[20] JPL ephemerides: https://ssd.jpl.nasa.gov/?planet_eph_export; INPOP ephemerides: https://www.imcce.fr/inpop

regularly occulted by the planet as seen from Earth[21]. This problem can however be solved for the duration of the mission by ensuring that the spacecraft flies over the entire sphere while it is tracked from Earth with the required spatial sampling.

The gaps in the tracking are however most often due to the fact that the spacecraft missions are not dedicated to the gravity field determination and a continuous tracking is not systematically scheduled. Furthermore, continuous tracking needs a steerable spacecraft antenna to point toward Earth as often as possible. Such an antenna is however more expensive than an antenna tied to the spacecraft, and so is not systematically implemented.

Doppler measurements do not provide the three components of the spacecraft velocity but its projection on the Line-Of-Sight (LOS) direction (Earth-spacecraft direction). The orientation of the orbital plane with respect to the LOS direction is therefore a constraint affecting the gravity solution. When the orbital plane is viewed face-on from Earth, the Doppler tracking data merely provide the component of the orbital velocity perpendicular to the orbital plane. Since most of the information about the gravity field arises from the in-plane orbital velocity component, this face-on geometry is of little interest for gravity field determination. On the other hand, the edge-on geometry (when the orbital plane is viewed edge-on from Earth) provides the richest geometry for gravity field determination. The orientation of the orbital plane with respect to the LOS direction is controlled by the drift of the ascending node and the relative position of the planet and Earth, such as shown in Figure 9 for Mars Global Surveyor. For Mars Express (MEX), it is mainly driven by the Earth-Mars relative position since its highly elliptical orbit makes its orbital plane drift negligible (Figure 9)[22].

In addition, Doppler tracking data are affected by propagation effects (see section 1.3.3), which will in turn degrade the gravity field solution, especially at short wavelengths which generate smaller spacecraft velocity perturbations. The accuracy of the gravity field solution also depends on the accuracy of the model of all the forces acting on the spacecraft (not only the gravitational attraction due to the planet itself). The inaccuracy of the knowledge of these forces affect the precision of the reconstructed orbit and so the accuracy of the gravity field (see section 1.4).

In summary, a low-altitude, near-circular and near-polar orbit tracked as often as possible is the most efficient orbit to map a gravity field with high spatial resolution. However, given the mis-knowledge of the full dynamics of the spacecraft (see section 1.4), the limitations of the Doppler measurements and the operational constraints from the other instruments on the spacecraft, defining a gravity experiment requires advanced simulations to assess the expected performance (Smith et al., 1990; Rosenblatt et al., 2019a,b; Rosenblatt et al., 2020a).

[21] When the orbital plane is viewed face-on from Earth the spacecraft is not occulted anymore, but this orbital plane orientation is of little interest for determining the gravity field.

[22] The secular drift of the ascending node is proportional to $(R^2/a^{7/2})$, a being the semi-major axis of the orbit and R the planetary radius (see Appendix B). As MEX orbit has a semi-major axis about two and half times larger than that of MGS (Table 1), its secular drift is about twenty-five times slower than for MGS.

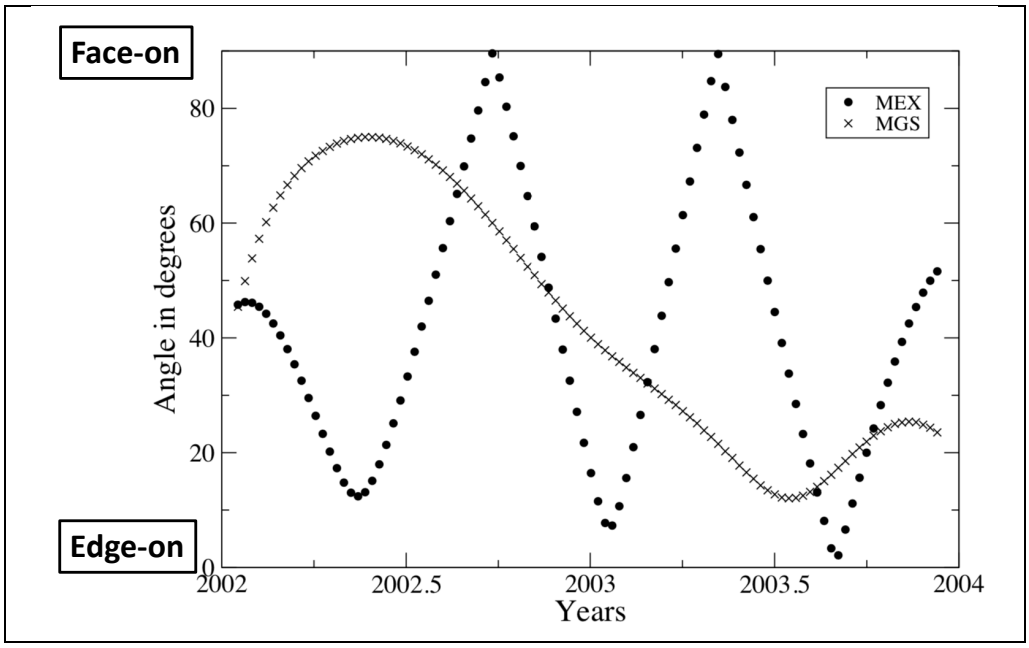

Figure 9: Orientation of the orbital plane with respect to the direction of Earth over one Martian year for Mars Global Surveyor (MGS) and Mars Express (MEX) orbits. Simulations performed with GINS software.

1.4 Precise Orbit Determination (POD)

Once the tracking data have been collected, they must be carefully processed to extract the gravity field solution. The process is called Precise Orbit Determination (POD), and consists in generating predictions of Doppler tracking data and in performing a least square fit to observed Doppler data (Figure 10)[23].

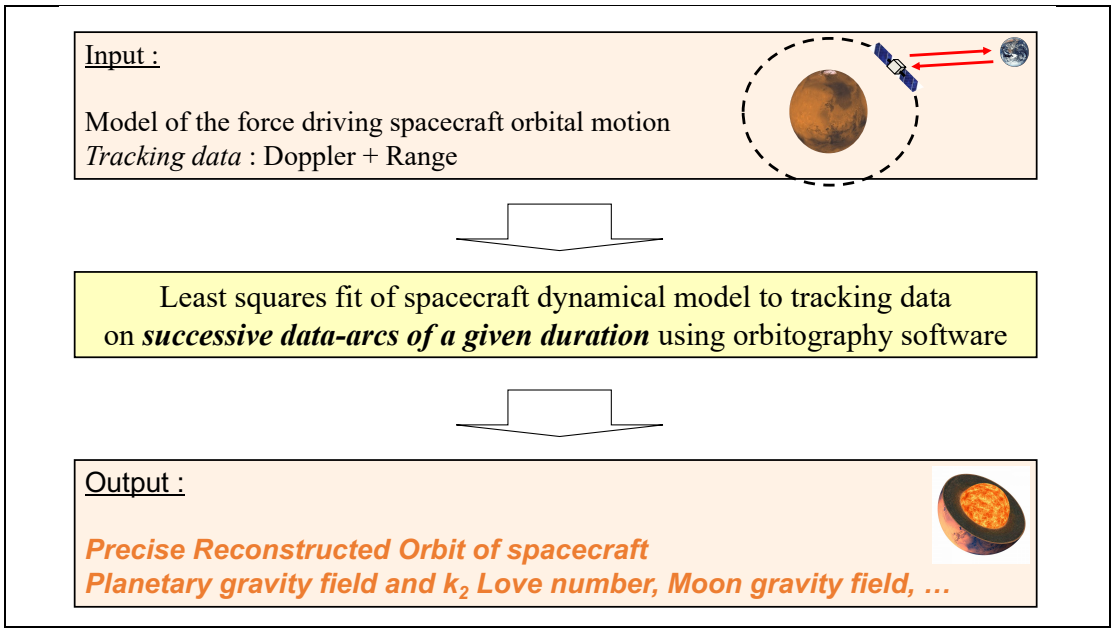

Figure 10: Precise Orbit Determination (POD) process

[23] The same approach is also used to compute the navigation orbit required for scheduling spacecraft payload observations and operations. However, it is less precise than for POD since the navigation purpose is not to improve the gravity field of the planet.

POD relies on software dedicated to accurate reconstruction of spacecraft orbits around celestial bodies. In my career I have used and contributed to the development of the GINS (Géodésie par Intégration Numérique Simultanée)[24] software developed by the French space agency CNES for terrestrial as well as planetary geodesy applications (Marty et al., 2009). On the NASA side, two software have been developed and extensively used for planetary geodesy applications: DPODP at JPL (Jet Propulsion Laboratory) (Moyer, 1971; Konopliv et al., 2006) and GEODYN at GSFC (Goddard Space Flight Center) (Pavlis et al., 2013). In Europe, the Italian software Orbit-14 has been used for NASA's JUNO mission around Jupiter (Serra et al., 2019), and in Germany a dedicated software has been used for ESA's MEX Phobos flyby and the Rosetta mission (Andert et al., 2010; Paetzold et al., 2016). Other developments are being implemented on the basis of pre-existing software used for terrestrial geodesy like the BERNESE in Switzerland (e.g. Arnold et al., 2015).

1.4.1 The force model

POD software numerically integrate the orbit of the spacecraft based on a force model. There are two different kinds of forces to take into account: the gravitational and non-gravitational forces. They are listed in Table 3 and briefly described hereafter[25].

Gravitational forces	Non-gravitational forces
Attraction by the gravity field of the planet	Atmospheric drag
Solid tides	Solar radiation pressure
Attraction by the Sun and others planets	Albedo and Infra-Red radiation pressure
Attraction by the gravity field of natural satellites	Thermal emissivity of the faces of the spacecraft
	Attitude maneuver (inertial wheel desaturation)

Table 3: List of the main forces driving the orbital motion of the spacecraft

Gravitational forces are computed from the most recent spherical harmonics solution of the gravitational potential of the planet since the goal of a gravity experiment is to improve the current solution. The solid tides are introduced following the IERS (International Earth Rotation and Reference Systems) conventions[26] as a tidal potential expressing the effect of tidal deformation on the gravitational potential, i.e. a scale factor of the second-degree gravity potential $(1+ k_2)$ with k_2 the tidal potential Love number (Marty et al., 2009).

The gravitational attraction of the Sun and others planets are modeled using a point mass representation, requiring only their masses and positions relative to the planet given by the planetary ephemerides. In the case of Mars, the gravitational attraction of

[24] https://www5.obs-mip.fr/wp-content-omp/uploads/sites/28/2017/11/GINS_Algo_2013.pdf
[25] The force model is described in detail for each orbitography software in e.g. Konopliv et al., 2006 for DPODP; in e.g. Genova et al., 2016 for GEODYN, and in Marty et al., 2009 for GINS. Each software however uses very similar model.
[26] https://www.iers.org/IERS/EN/DataProducts/Conventions/conventions.html

its moons, Phobos and Deimos, is also taken into account. The best available solution for their masses (Paetzold et al., 2014; Jacobson, 2010) and their positions relative to Mars (Lainey et al., 2007; Jacobson, 2010) are considered.

A general relativity correction is also applied to take into account the fact that the numerical integration of the motion is performed in the Newtonian approximation. The Schwarzschild effect is generally considered, but geodetic precession and Lense-Thirring effects can also be included (Marty et al., 2009).

Non-gravitational forces (except for inertial wheel desaturation events) are exerted on the faces of the spacecraft, which in turn requires a 'geometric' representation of the spacecraft. This representation is called *macro-model* or *box-and-wings* model (Figure 11). The surfaces are represented as flat plates (six for the bus and two for each solar panel, and a parabolic surface for the high gain antenna) with known areas and optical properties (averaged values of reflectivity, diffusivity and absorptivity coefficients). The macro-model needs to be oriented in space at any given time (i.e. with respect to the Sun and the planet for the radiation pressure forces, and to the along-track direction for the drag force). It is performed using quaternion datasets (of the bus and mobile parts such as solar arrays and steerable antenna) either predicted or reconstructed by the navigation team from onboard measurements. The error on the spacecraft orientation is typically a few milliradians, generating mismodeling of non-gravitational forces not larger than 1-3%. The thermal emission force also requires monitoring the temperature of the faces. However, this force is generally smaller than the other non-gravitational forces.

The atmospheric density at low orbital altitude is very small but the velocity of the spacecraft is of the order of a few km/s and hence generates a significant drag. An atmospheric drag force must thus be included in the force model, requiring a model for the density of the atmosphere at low orbital altitude. Density models are however affected by large errors which make the drag force one of the most poorly modeled of all the forces (e.g. Bruinsma and Lemoine, 2002; Justh et al., 2011).

The interplate self-shadowing of the spacecraft is also modeled for the radiation pressure and atmospheric drag surface forces.

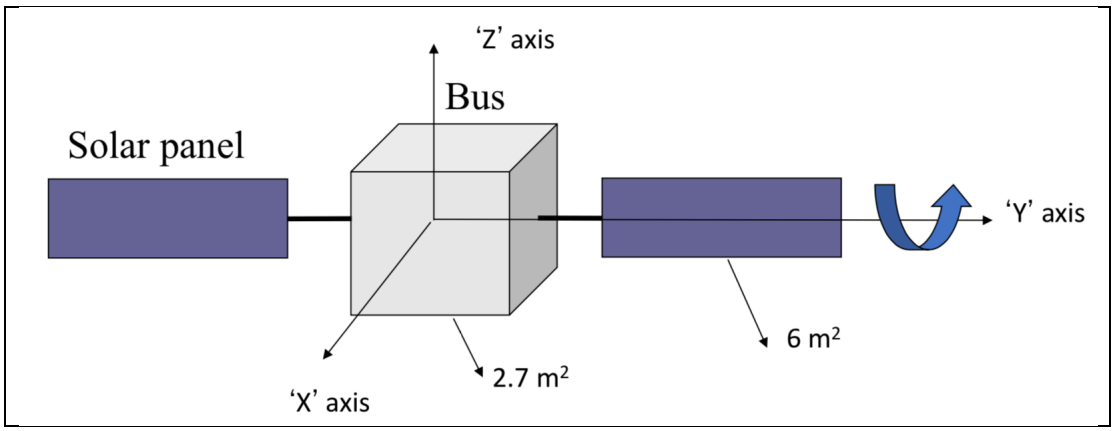

Figure 11: *Macro-model* or *box-and-wings* representation of the spacecraft (the high Gain Antenna is not shown). The *Macro-model* displayed here is the MEX model for which only solar arrays can move with respect to the bus (rotating around the Y-axis).

Modern spacecraft are 3D-stabilized, i.e. inertial wheels aboard control their attitude. Depending on the attitude changes, required for the scheduling of the different observations, these wheels become more or less rapidly saturated. A maneuver is then required, which consists of desaturating the wheels (Inertial wheel desaturation

event[27]). In order to maintain the spacecraft attitude during this maneuver, pairs of thrusters are burned to exert a counter-torque[28]. Unfortunately, the burns of the thruster pairs are imbalanced and a residual acceleration is imparted to the spacecraft, which must be taken into account in the force model (e.g. Smith et al., 1990; Lemoine et al., 2001). The epoch of each of these attitude maneuvers is provided by the navigation team, and a residual acceleration has to be added to the force model occurring at each desaturation event.

Since the orbit represents the motion of the center of mass of the spacecraft and Doppler measurements are performed between the center of phase of the HGA and Earth-based stations, one needs to correct for the shift between the position of the two centers. This information is provided by the mission before launch and is then monitored, as precisely as possible, by the navigation team. The position of the center of mass indeed changes due to mass movements inside the propellant tanks. The center of mass position can also change due to the orientation of solar panels and to some extent of the HGA such as for MRO (Genova et al., 2016). Depending on its amplitude and frequency it can have a detectable effect on the Doppler tracking data. The mass of the spacecraft must also be monitored since all these non-gravitational forces are proportional to the ratio between the surface (exposed to the force) and the mass of the spacecraft.

The macro-model, its orientation (quaternions), the epoch of each maneuver, the shift between both center of phase and center of mass, and the mass history of the spacecraft are the ancillary dataset, which is as important as the tracking dataset itself in order to perform POD.

From this force model, the trajectory of the spacecraft is numerically integrated over successive data-arcs. At the beginning of each arc, the initial state vector (position and velocity) of the spacecraft must be known. It can be either estimated from tracking data (Konopliv et al., 2006) or taken from a navigation orbit solution (Rosenblatt et al., 2008; Marty et al., 2009). Each arc has a typical duration of a few days (2 to 7) depending on the spacecraft orbital period, the mismodeling of the force model, the tracking coverage and the orbit control maneuvers (OCM)[29].

The numerical integration provides the modeled position and velocity of the spacecraft in a given planet-centered Inertial Body frame (Figure 12). The most useful frame is an inertial frame defined as the inertial position of the equator plane of the planet at the J2000 epoch.

Since the forces are computed in a reference frame tied to the planet (Body-Fixed frame[30], Figure 12), it is necessary to model the rotation matrix from this Body-Fixed frame to the Inertial Body frame, which is most often defined on the basis of the IAU (International Astronomical Union standards[31], Figure 12). This matrix corresponds to

[27] also named Angular Momentum Desaturation (AMD) and Wheel off Loading (WoL) maneuver for NASA and ESA spacecraft, respectively.
[28] These maneuvers consist actually of a series of small thrusts (typically 0.1 second duration) over a couple of minutes in order to control the attitude of the spacecraft during the maneuver.
[29] Perturbing accelerations generated by OCMs are much larger than those due to inertial wheel desaturation maneuvers, and hence are more difficult to determine accurately. Consequently, the data-arcs are chosen to avoid the OCMs in order to preserve an accurate calculation of the orbit.
[30] The reference frame in which the gravity field is expanded in spherical harmonics.
[31] https://www.iau.org/news/announcements/detail/ann07013/

the modeling of the orientation and rotation of the planet[32]. The mismodeling of this matrix can have a detectable effect on the Doppler tracking data and so on the reconstructed orbit.

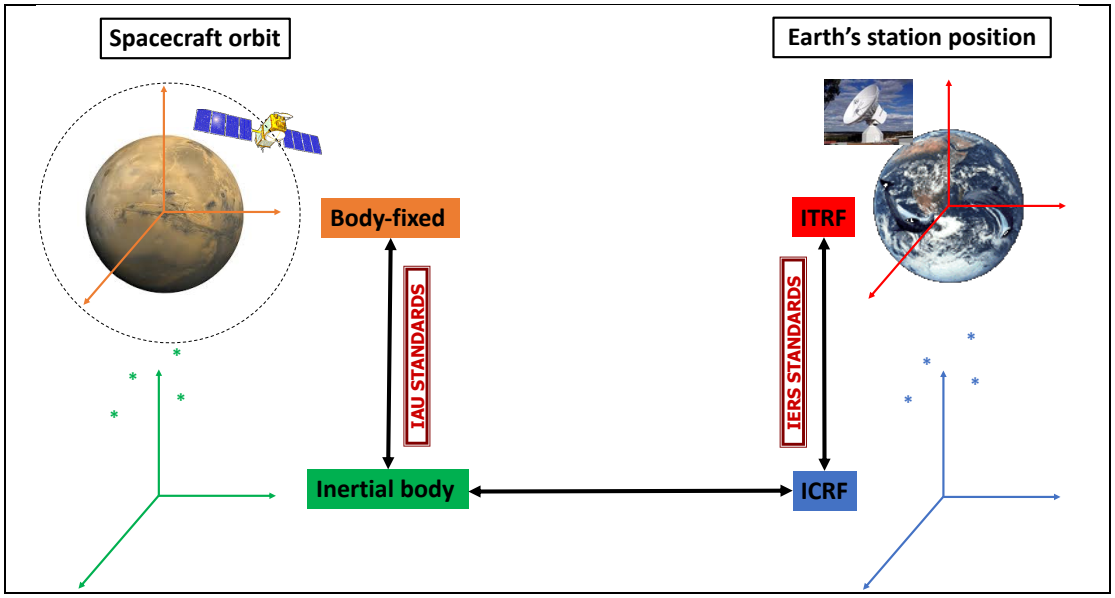

Figure 12: Reference frames used for POD.

1.4.2 Least squares fit to tracking data

A least-squares fit of the predicted data to the observed data[33] is performed in order to estimate the parameters of the force model. These predictions correspond to the range between the spacecraft and the tracking station and its variations over the Doppler count time (range-rate, Figure 13). This is a physical modeling of the tracking data in contrast to the engineering modeling by Moyer (2000). The range-rate is the difference between the spacecraft-station round-trip range at the start Doppler count time t_1 and end time t_2, more precisely: $\rho_2 + \rho_4 - \rho_1 - \rho_3$ (Figure 13). This, when divided by the Doppler count time, provides the predicted 2-way Doppler shift or predictions of Doppler tracking data.

The positions of the tracking stations are provided by the deep space network in a terrestrial reference frame such as the ITRF (International Terrestrial Reference Frame) from which the positions at any time in the ICRF (Inertial Celestial Reference Frame) can be deduced. This approach, used in the GINS software, relies on the IERS standards[34] (Figure 12), which are accurately established and regularly updated, hence providing planetary applications with the best estimations of the positions of the Earth-based deep space stations. The Earth's solid tides displacement and to a lesser extent the oceanic loading effect on these station positions are also computed (Marty et al., 2009). The ICRF can be easily transformed into the Inertial Body frame in which the spacecraft orbit is computed (see section 1.4.1).

[32] Konopliv et al. (2006) were the first authors to introduce a rotation matrix more complex than IAU standards by adding the spin rate variations and the nutations of the rotation axis of Mars
[33] Whenever possible corrections of propagation error on the tracking data are also performed by the software.
[34] https://www.iers.org/IERS/EN/Home/home_node.html

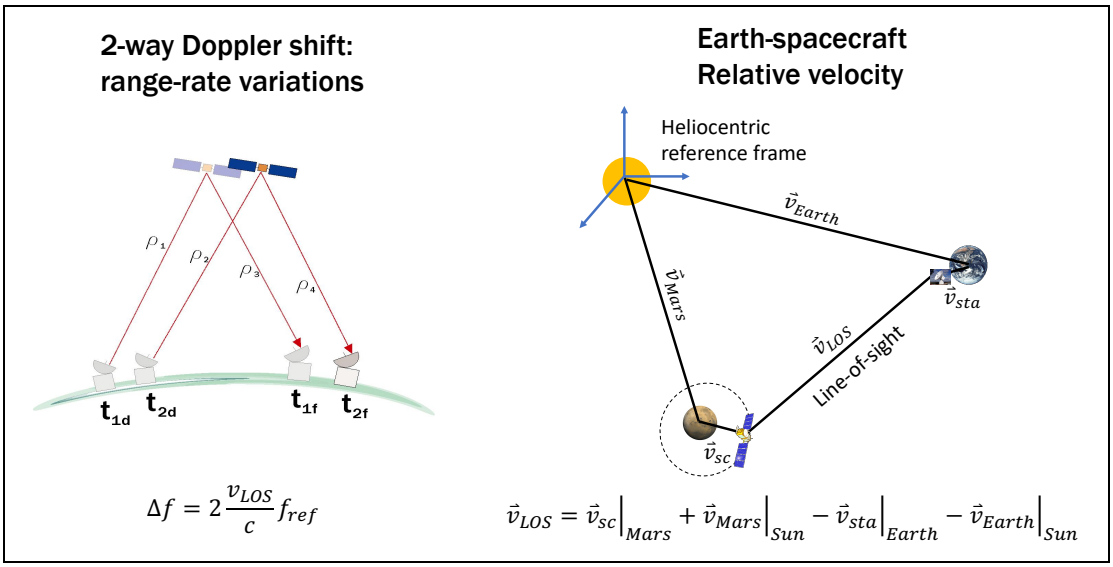

Figure 13: Physical model of the Doppler tracking data using the spacecraft orbit and the tracking station position. The term V_{LOS} is the projection of V_{rel} (spacecraft velocity relative to the Earth) on the Line-Of-Sight (LOS) direction between the spacecraft and the Earth.

The predicted tracking data are then fit to the observed tracking data in order to adjust the parameters of both the force model and the tracking data. The fit is a least squares batch which assumes that the tracking data have a Gaussian noise. In addition, auto-correlation between successive tracking data is not taken into account. A priori constraints on the parameters can also be applied depending on the a priori knowledge of these parameters. They are typically applied when the time period over which the force is exerted is not covered by the tracking data, for example during inertial wheel desaturation events.

Two kinds of parameters are fitted: the local and the global parameters (Table 4). The former concern individual data-arcs while the latter are common to all arcs. The least squares fit for each data-arc generates a normal matrix formed with the partial derivatives of the Doppler and Range observables with respect to each parameter.

Local parameters	Global parameters
The initial state vector at the beginning of the arc	The gravity field: C_{lm} and S_{lm} including the low-degree time variations
Scale factors of the radiation pressure and atmospheric drag forces	The low-degree tidal potential such as the k_2 Love number
The acceleration produced by each inertial wheel desaturation event	Seasonal variations of the orientation and spin of the planet
Biases on the tracking data: Doppler and Range	The mass and gravity coefficients of the natural satellites (in the case of Mars)

Table 4: Parameters fit to tracking data in the POD process.

The inversion of this normal matrix gives the solution for the local parameters, and a new orbit that is the precise reconstructed orbit. The global parameters are obtained by inverting the global normal matrix formed by stacking together all the individual normal matrices (i.e. by summing all the partial derivatives of the global parameters

over the period covered by all the data-arcs). The local parameters are solved for by GINS and the global parameters by another software called DYNAMO also developed by CNES.

Since the high degree C_{lm} and S_{lm} coefficients of the gravity solution have a signature in the orbital velocity perturbations of the order of the noise in the tracking data, they cannot be properly resolved and Kaula's power law (see Section 1.2.2) is applied as a priori constraint to stabilize the inversion of the global normal matrix. In practice, the effect of this constraint is to flatten the spectrum of the error on the coefficients at high degree. However, at the highest degrees, the constrained gravity solution corresponds only to Kaula's power law.

A priori constraints can also be used for others parameters but the philosophy followed with GINS and DYNAMO is to introduce as few as possible a priori constraints in order to extract the information actually contained in the tracking data. For instance, loose constraints are applied to the acceleration generated at each inertial wheel desaturation event. This explains why empirical forces are not used in the GINS approach unlike in the DPODP or GEODYN approaches (e.g. Konopliv et al., 2006; Genova et al., 2016)[35].

1.5 The gravity field of the Martian system

The first spherical harmonics solution of Mars gravity field was expanded up to degree and order 12 (Christensen and Balmino, 1979)[36] using the tracking data of the Mariner-9 spacecraft (the first ever artificial satellite of Mars in 1972). Later, a model up to degree and order 18 was produced, using the additional Doppler tracking data of the NASA's Viking 1 & 2 orbiters (Balmino et al., 1982). As for Mariner-9, these Doppler data were in the S-band (2.3 GHz), hence noisier than the present X-band data. In addition, the orbits of these spacecraft were not suitable for gravity field mapping (i.e. neither polar nor circular). However, the degree 18 at Mars corresponds to a spatial resolution of 600 km, similar to the resolution of the Earth's gravity solution obtained at the same time with the tracking of artificial satellites (the GRIM3-S solution had a spatial resolution of 550 km, Reigber et al., 1985)[37].

The Balmino et al.'s (1982) solution was the best until modern spacecraft with X-band tracking data and orbits more suitable for gravity were launched to orbit around Mars, i.e. MGS, ODY and MRO (Figure 14). They collected data to greatly improve the spatial resolution and the accuracy of Mars' gravity field including the tidal potential component and the seasonal variations of the lowest degree zonal harmonics (see Section 1.5.2).

MEX is the first ESA spacecraft orbiting a planet. It was launched in 2003 and arrived near Mars on Christmas day of the same year (Figure 14). It especially improved the determination of the mass of the largest natural satellite of Mars, Phobos (see Section 1.5.3). As for almost all interplanetary missions, the gravity field was not a goal of the MEX mission, but a radio science team existed and I was involved in it to participate to the gravity investigations that could be realized with MEX tracking data.

---

[35] These authors fit additional forces in along, radial and normal directions to absorb imperfections of their force model. This fit is in general tightly constrained.

[36] A model was previously obtained but only up to degree and order 2 (Lorrel et al., 1973).

[37] The gravity field of the Earth had however a better resolution at places where ground measurements of the gravity were done (especially over the continents).

I thoroughly studied these data and performed POD of MEX, implementing ESA's tracking and ancillary data and MEX macro-model into GINS. In parallel, I participated to the collection and pre-processing of ancillary data (quaternions, maneuver epochs, macro-model, …) for ODY and MRO.

Figure 14: Martian spacecraft used for the determination of the gravity field of Mars and of its moons: Mars Global surveyor (MGS), Mars Odyssey (ODY), Mars Reconnaissance Orbiter (MRO) and Mars Express (MEX).

1.5.1 POD of Mars Global Surveyor, Mars Odyssey and Mars Express spacecraft

1.5.1.1 Non-continuous tracking coverage of Mars Express (MEX)

The MEX spacecraft has a high-gain antenna fixed to it, which prevents tracking during nadir pointing to the planet to realize other observations, especially at pericenter (periapsis) passes. The tracking is thus non-continuous, and covers from 20 to 80 percent of the time every week, with an average of 40 percent over the 2004-2007 period (Rosenblatt et al., 2008). It represents on average one third of the pericenter covered by tracking data. As MEX's pericenter is at low altitude (250 km, Figure 15), the drag acceleration is twice as large (8×10^{-8} m/s^2) as the drag acceleration for MGS/ODY at 400 km altitude (4×10^{-8} m/s^2, Figure 15). This first computation already indicates that MEX's orbit could be less precise than that of MGS or ODY because of

the larger drag force and the lack of tracking especially at pericenter passes when the drag force is maximum.

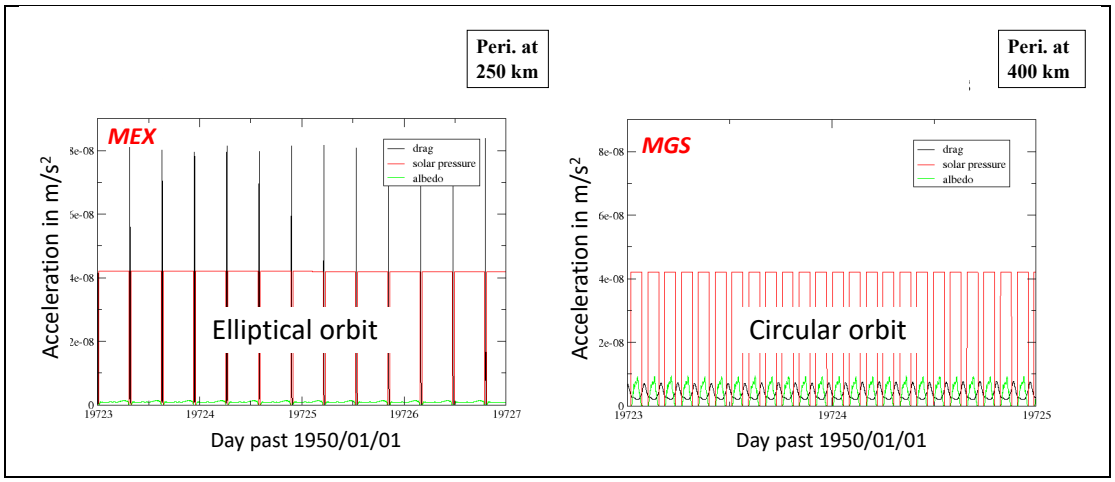

Figure 15: Comparison of non-gravitational acceleration for MEX and MGS. Computation performed with GINS

1.5.1.2 POD of MEX, MGS and ODY

A first assessment of the quality of the POD is provided by the Doppler and range post-fit residuals (Figure 16). MEX Doppler rms values are around 1-2 mHz (0.015-0.03 mm/s)[38] and those for MGS and ODY are around 2-5 mHz (0.03-0.075 mm/s). All spacecraft show two periods with larger rms values, corresponding to the two solar conjunction periods (September 2004 and October 2006, Figure 16).

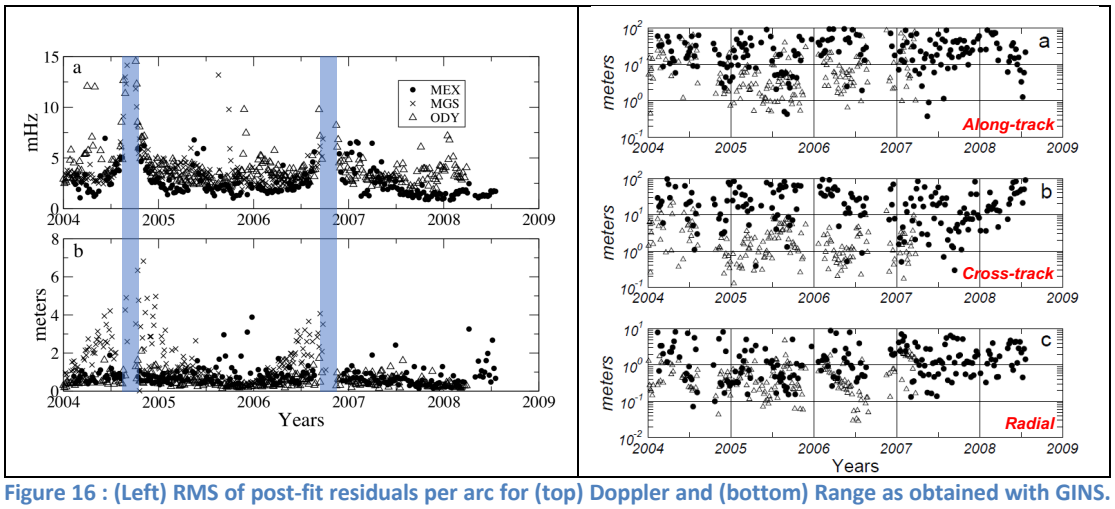

Figure 16 : (Left) RMS of post-fit residuals per arc for (top) Doppler and (bottom) Range as obtained with GINS. Two solar conjunctions occur in the period covered by this study (blue shaded columns). (Right) Orbit overlap comparison MEX vs ODY. The MGS overlap differences are comparable to the ODY ones (Marty et al., 2009), hence not shown in the figure for readiness. Adapted from Rosenblatt et al. (2008) and Marty et al. (2009).

The Doppler post-fit residuals values are close to the Doppler noise level (off conjunction, see section 1.3.3), implying that the least squares fit has extracted all the

[38] The MGS and ODY Doppler data are at 10 seconds count time while MEX data are at 60 seconds count time. The MEX residuals should thus be multiplied by the square root of the count time ratio (i.e. sqrt(60/10)) to be compared with 10 seconds count time Doppler data. That corresponds to MEX residuals between 0.035 and 0.07 mm/s, which are comparable to MGS/ODY ones.

orbit information contained in the Doppler tracking data. However, it does not necessarily mean that this information has been properly distributed among the dynamical parameters.

The average of the range rms values are less than one meter for all spacecraft corresponding to the average precision of the spacecraft position relative to the tracking stations (see Section 1.3.3). They indicate that there are no large biases in the dynamical modeling of spacecraft motion, but not necessarily that all spacecraft orbits are determined with the same precision. Note that a range bias per data-arc has also been estimated to correct errors in the planetary ephemeris (Figure 19).

The error on the reconstructed orbit is estimated on the basis of spacecraft position differences between overlapping arcs (it is a test of internal coherency of the reconstructed orbit). The overlapping time period is one orbital period for MGS and ODY (~2 hours, Konopliv et al., 2006; Marty et al., 2009) and three orbital periods for MEX (~21 hours, Rosenblatt et al., 2008). The MEX overlapping differences in all three cross-track, along-track and radial directions are about 10 times larger than the MGS/ODY differences (Figure 16). This larger error on the MEX orbit is due to the non-continuous tracking, which has crucial consequences when the MEX pericenter passes within a data-arc are not tracked (Figure 17). In that case, the drag scale factor becomes negative, implying that the atmospheric density is negative, which is obviously impossible. The ideal value of this drag scale factor should be equal to one if the drag force was perfectly modeled (i.e. spacecraft orientation, density of the thermosphere, drag coefficient were perfectly known, e.g. Rosenblatt et al. (2012), and if it was not correlated with other parameters). In fact, density of the thermosphere is not so well known and due to correlations between the drag scale factor, the adjusted accelerations generated by the inertial wheel desaturation maneuvers (WoL events) and the initial state vector, the drag scale factor absorbs information from these other forces. This situation occurred in particular for six periods around mid-2004, at the end of the first quarter of 2005, at the first quarter of 2006, at the end of 2006, at the third quarter of 2007, and in 2008 (Figure 17). This result clearly illustrates that the absence of tracking data at low-altitude pericenter passes significantly degrades the accuracy of the reconstruction of an elliptical orbit.

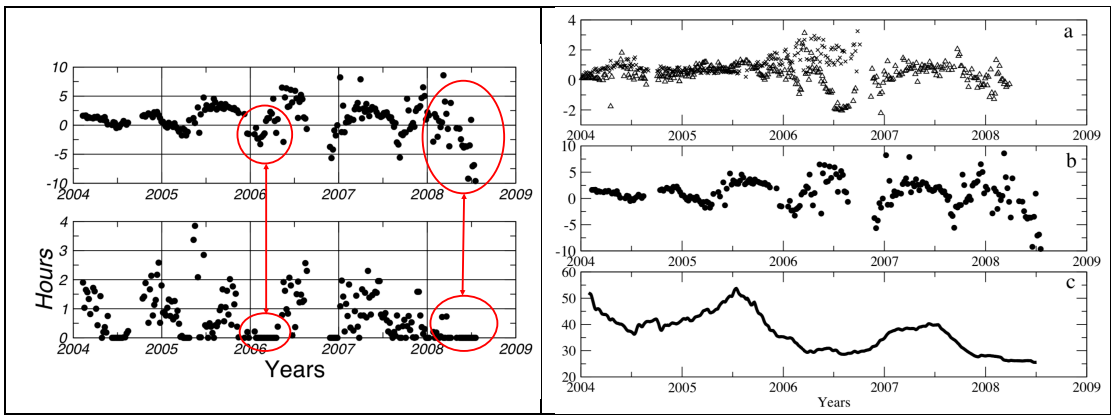

Figure 17: (Left): (top) Drag scale factor estimation for Mars Express (MEX), (bottom) tracking coverage at pericenter passes (altitude < 700 km). Red circles indicate examples of the match between negative values of drag scale factor and the absence of tracking data at pericenter passes. (Right): Drag scale factor values for (a) MGS (crosses) and ODY (triangles), (b) MEX drag scale factor (see left panel), and (c) solar flux at 10.5 nm wavelength at Mars. Adapted from Rosenblatt et al. (2008) for MEX and Marty et al. (2009) for MGS/ODY.

The behavior of the MEX drag scale factor is not observed for MGS/ODY (Figure 17) since the tracking is quasi-continuous and the orbits are near-circular so that the drag acts continuously on the spacecraft and not only in the lower altitude part as for MEX. However, negative values of MGS/ODY drag factors were observed in 2006 and to a lesser extent at the end of 2007 and the beginning of 2008 for ODY (Figure 17). For the 2006 period the MEX drag scale factor values are not systematically negative but they strongly vary over the data-arcs. One possible explanation for the difficulty to determine the drag scale factor for the three spacecraft is that these periods coincided with solar flux minima at 10.5 nm wavelength (Figure 17). As the solar flux was significantly reduced, the atmospheric density is lower than usual, thus reducing the drag acceleration, and making it difficult to separate from other perturbing forces such as those generated by the inertial wheel desaturation maneuvers (WoL or AMD events), particularly for their component in the along-track direction.

The MEX solar pressure scale factor shows a linear trend over the 2004-2006 period and stabilizes afterwards at around the value of 1.17 (Figure 18). Like for the drag scale factor, this solar pressure scale factor should be equal to one if the radiation pressure force would be perfectly modeled[39]. A similar trend is observed for the MGS solar pressure scale factor at the beginning of the mission (from 1999 to 2002, see Figure 18), but not for ODY over the whole 2002-2008 period. This trend could result from the variations of physical properties of the faces of the spacecraft such as temperature variations or the darkening of these faces with time, but we have no information to verify these hypotheses. The ODY solar pressure scale factor presents peaks (up to 1.5) at the first quarter of each year from 2003 to 2007 (Figure 18). Such a behavior is also observed with DPODP POD processing but with ten times smaller amplitude (A. Konopliv, pers. comm., 2012).

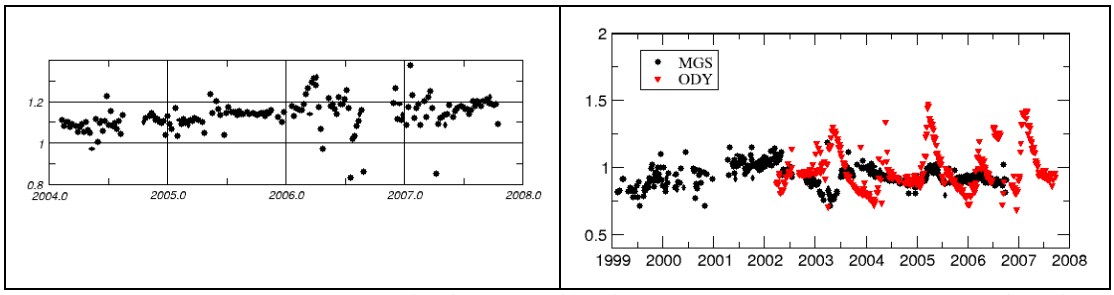

Figure 18: Solar pressure scale factor for (left) MEX and (right) MGS and ODY. From Rosenblatt et al. (2008) and Marty et al. (2009).

The correction of the residual acceleration at each MEX WoL event is on average 10 percent of the initial value provided by the navigation team for the along-track direction but at least one hundred percent for the two other directions, which have however ten times smaller amplitudes (Rosenblatt et al., 2008). This is due to the fact that these events are not systematically tracked from Earth, and thus not constrained by tracking data. For MGS/ODY, the corrections on the AMD residual acceleration are much smaller and do not exceed 60 percent of the initial value in the three cross-track, along-track and radial directions (Marty et al., 2009). This is certainly due to the quasi-continuous tracking supporting regular corrections of the force model at each AMD residual acceleration.

[39] The value of the optical properties of the MEX spacecraft were not properly calibrated, and a more realistic value of about 1.15 should be applied to correct it (ESOC, pers. comm., 2007).

The position of the orbiting spacecraft relative to the Earth-based tracking stations is affected by errors on the position of Mars provided by planetary ephemerides such as the JPL DE414 (Rosenblatt et al., 2008; Marty et al., 2009). Therefore, a bias on the range is estimated per data-arc for the three spacecraft with very similar values around 1-2 meters for periods before April 2005 (Figure 19). After this date, the range bias values vary with a peak-to-peak amplitude up to 80 meters. It actually reflects residual errors in the DE414 ephemeris for which no range data from spacecraft have been introduced after April 2005 (Standish, 2006). When we recomputed this bias for MEX and ODY using a more recent ephemeris (DE421, Folkner, 2007), which integrates spacecraft ranging residuals after April 2005, the large fluctuations after that date disappeared (Figure 19). A clear signature however remains with a period close to the Earth-Mars synodic period and an amplitude of about 2 meters. Such a signature at the synodic period could be due to insufficient correction of the interplanetary plasma effect on the range data in our GINS software (W.M. Folkner, private communication, 2012) or due to inaccuracy in the calculation of Mars ephemeris caused by the poor knowledge of asteroid masses in the neighboring main belt. Whatever the explanation, this result emphasizes on the importance of the spacecraft range data for constraining planetary ephemerides, especially in the case of Mars. It is not only required for the purpose of POD but also for the preparation and accurate planification of solar system exploration missions.

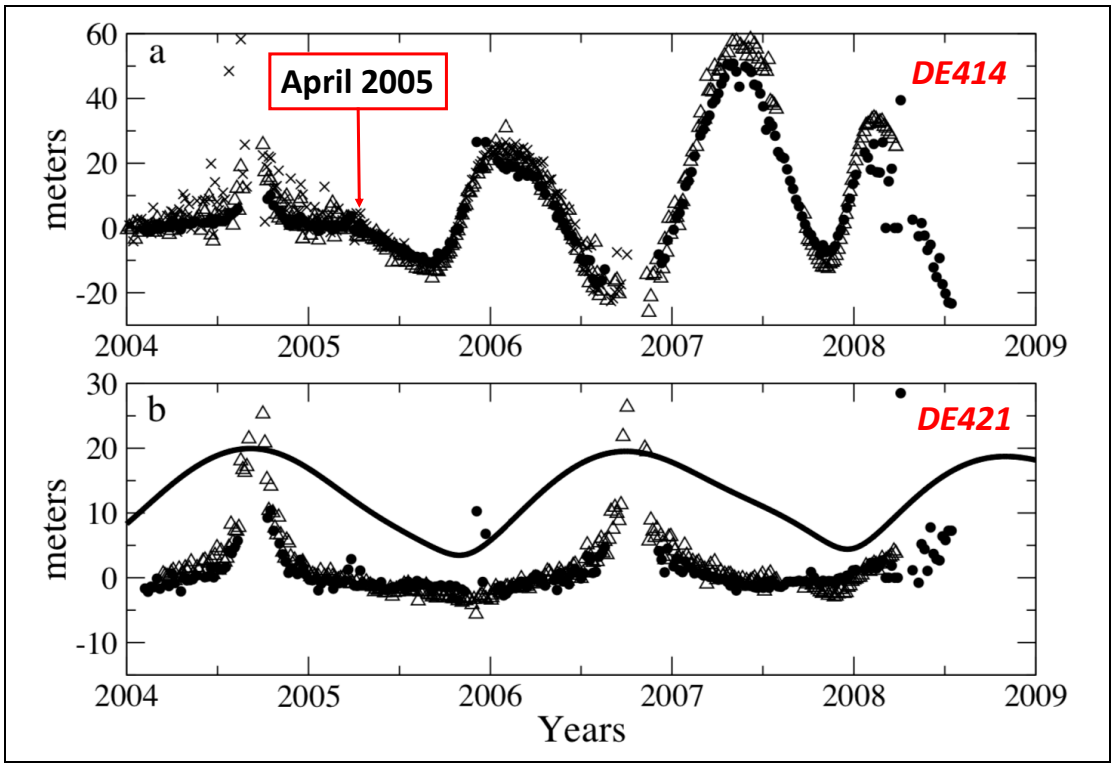

Figure 19: Spacecraft range bias estimates: (a) from MGS (crosses), ODY (open triangles) and MEX (closed circles) ranging data, using the JPL-DE414 planetary ephemeris for orbit computation, (b) ODY (open triangles) and MEX (closed circles) range bias estimates using the JPL-DE421 planetary ephemeris for orbit computation. The solid line is the Earth-Mars distance from DE421, and it has been scaled to fit into the diagram. Adapted from Rosenblatt et al. (2008) for MEX and Marty et al. (2009) for MGS and ODY.

The lack of MEX tracking data at the WoL events and at many pericenter passes (two-third on average) limits the accuracy of the reconstructed orbit. In addition to the

highly elliptical orbit, this limited accuracy hinders improvement of the spatial resolution of the gravity field of Mars. An alternative would be to use a local approach instead of a global harmonic approach (e.g. Barriot et al., 1998), but there are not enough tracking passes covering the pericenter to improve locally the gravity field (Beuthe et al., 2012).

1.5.2 Mars Gravity field, its seasonal variations and k_2 Love number

The gravity field of Mars (including the tidal component and seasonal variations) have been improved using the MGS and ODY tracking data (e.g. Lemoine et al., 2001; Yoder et al., 2003; Konopliv et al., 2006; Marty et al., 2009; Lemoine et al., 2006). Contact with MGS was lost at the end of 2006, but ODY is still in activity and tracked while MRO has started its mission in 2007 and is still being tracked. Processed tracking data are regularly updated and the gravity solutions are refined (e.g. Marty et al., 2013; Konopliv et al., 2011; 2016; Genova et al., 2016).

1.5.2.1 Mars static gravity field

The MGS and ODY dataset have been processed by three different software and teams: GINS at CNES/GRGS for the MGGM08A solution (Marty et al., 2009), DPODP at JPL for the MGS95J solution (Konopliv et al., 2006), and GEODYN at GSFC for the MGM1041c solution (for which only MGS data were processed, Lemoine et al., 2006). All solutions were developed up to degree and order 95 except for MGM1041c which was truncated at degree 90. The spatial resolution of these three different solutions is however very similar, of the order of 150 km for degree strength 70 as shown in Figure 20.

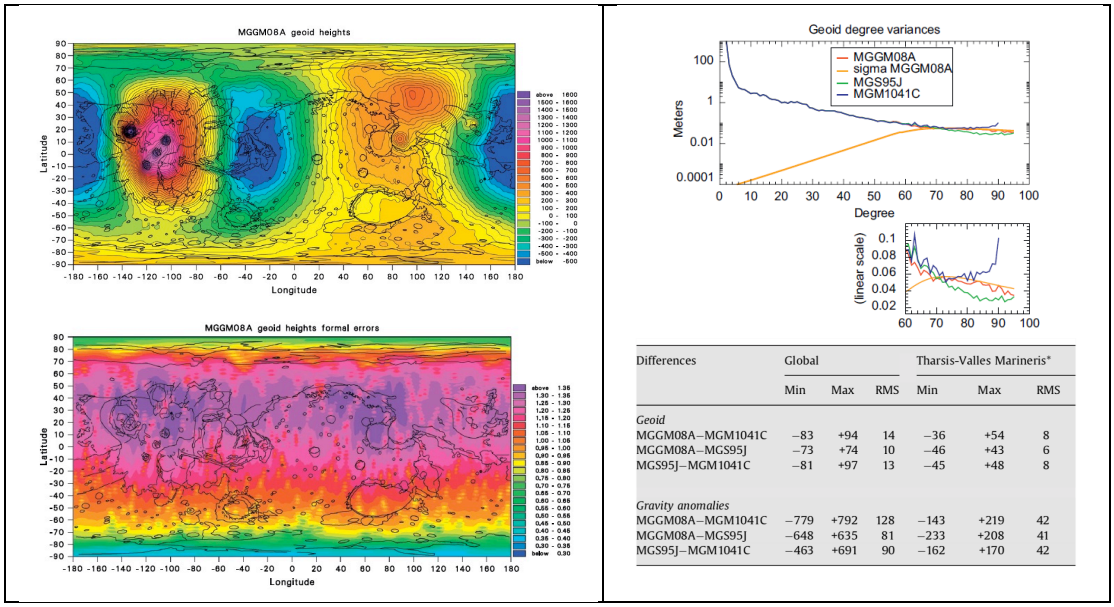

Differences	Global			Tharsis-Valles Marineris*		
	Min	Max	RMS	Min	Max	RMS
Geoid						
MGGM08A–MGM1041C	−83	+94	14	−36	+54	8
MGGM08A–MGS95J	−73	+74	10	−46	+43	6
MGS95J–MGM1041C	−81	+97	13	−45	+48	8
Gravity anomalies						
MGGM08A–MGM1041C	−779	+792	128	−143	+219	42
MGGM08A–MGS95J	−648	+635	81	−233	+208	41
MGS95J–MGM1041C	−463	+691	90	−162	+170	42

Figure 20: (left top) Mars geoid heights (in meters) of the solution MGGM08A obtained with GINS/DYNAMO processing of MGS and ODY tracking data, (left bottom) Map of MGGM08A geoid formal uncertainty (1-sigma). (right top) Comparison of power spectra of MGGM08A, MGS95J, and MGM1041c with the error spectra of MGGM08A, (right bottom) statistics of comparison between the geoid and gravity maps of the MGGM08A, MGS95J, and MGM1041c. Adapted from Marty et al. (2009).

The formal uncertainty on the MGGM08A geoid is between 30 cm and 1.30 meters (Figure 20), but the rms of the differences between the three different Martian solutions is 6-8 meters (corresponding to 41-42 mGal in gravity anomalies, Figure 20), suggesting some biases between the different solutions. The error is not uniformly distributed at the Martian surface because of the geographical distribution of the lowest altitude of the spacecraft orbits tracked from Earth and also the convergence of the tracks at polar areas.

Mars Reconnaissance Orbiter (MRO) has an orbit with altitude (255 x 320 km) lower than that of MGS/ODY (400 x 400 km). Although the larger drag force has limited its expected performance for gravity measurements, MRO gravity solutions are developed up to degree and order 120 (MRO120D from JPL, Konopliv et al., 2016, and GMM-3 from GSFC, Genova et al., 2016). The degree strength is at degree 95 (112 km, for GMM3) and 100 (107 km for MRO120D). As for MGGM08A, both solutions have geographically variable resolution with a degree strength at 100 (GMM3) and 115 (MRO120D) over the South pole areas (see figure 6 in Genova et al., 2016 and in Konopliv et al., 2016). An updated solution is in preparation using GINS (Marty et al., 2013).

1.5.2.2 k_2 Love number

The gravitational pull of the Sun deforms the planet inducing a slight redistribution of mass inside and modifying its gravitational potential. It is expressed as a scale factor $(1+k_2)$ of the second-degree gravitational potential with k_2 the tidal potential Love number (Love, 1909). This Love number is tightly related to the deep interior structure of the planet (e.g. Rivoldini et al., 2011). A highly deformable interior will yield a larger redistribution of the internal mass, and so a larger modification of the gravitational potential, i.e. a larger Love number k_2. Large tidal measurements made on Earth in the nineteenth century were interpreted as the presence of fluid layers inside (evidence for a fluid core was obtained a couple of years later using seismic data). As there are no seismic data for terrestrial planets so far, the k_2 Love number is the most common measurement of the state and size of the core. Using MGS tracking data, Yoder et al. (2003) found a value in agreement with a fluid core. The k_2 value has been refined since, with values from 0.12 (Marty et al., 2009) to 0.17 (Konopliv et al., 2016; Genova et al., 2016). It supports a large fluid core up to 53-55% the size of the planet (Figure 21), which is similar to the relative size of Earth's fluid core (54.7%).

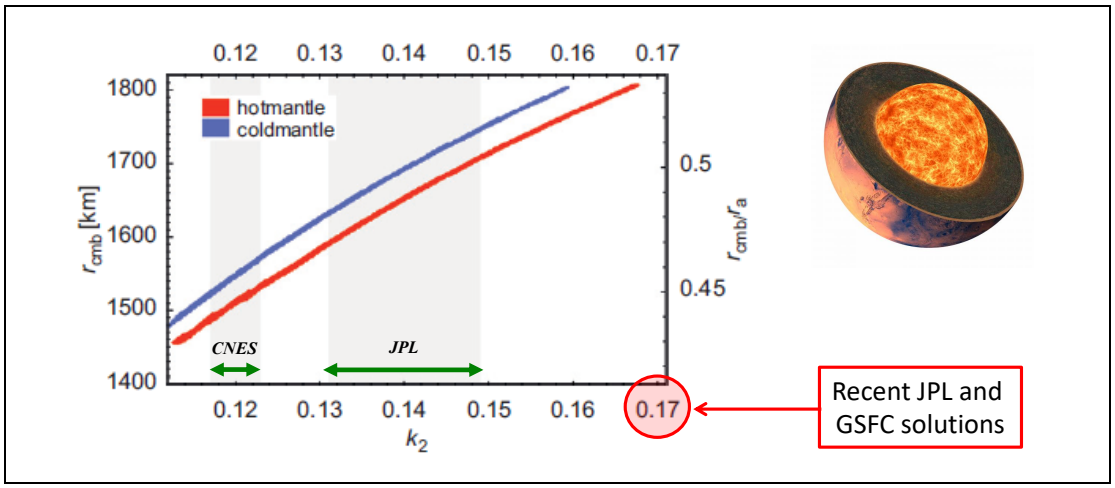

Figure 21: Theoretical predictions of Mars k_2 Love number as a function of the size of the fluid core and mantle temperature (adapted from Rivoldini et al., 2011) compared to estimation from MGS and ODY tracking data: gray shaded areas represent solutions and associated uncertainties (CNES from Marty et al., 2009, and JPL from Konopliv et al., 2006). Most recent solutions are also shown, using additional MRO tracking data by JPL (Konopliv et al., 2016) and GFSC (Genova et al., 2016), both with a 1-sigma error better than 0.01 (not shown in the figure).

1.5.2.3 Seasonal variations of the gravity lowest degree zonal harmonics

The high resolution gravity solutions are however challenged by the detection of the small signal due to Mars CO_2 seasonal mass transport between the polar caps and the atmosphere. The frozen CO_2 completely sublimates at the northern cap in summer and condensates at the southern cap (which is then in the winter season). The expected total mass of CO_2 involved in this seasonal cycle is about 25% of the atmosphere mass, yielding to seasonal gravity variations (Chao and Rubicam, 1990; Smith et al., 1999). The CO_2 seasonal mass budget has been estimated from the gravity seasonal variations determined with MGS and ODY tracking data (Smith et al., 2009, see Figure 22).

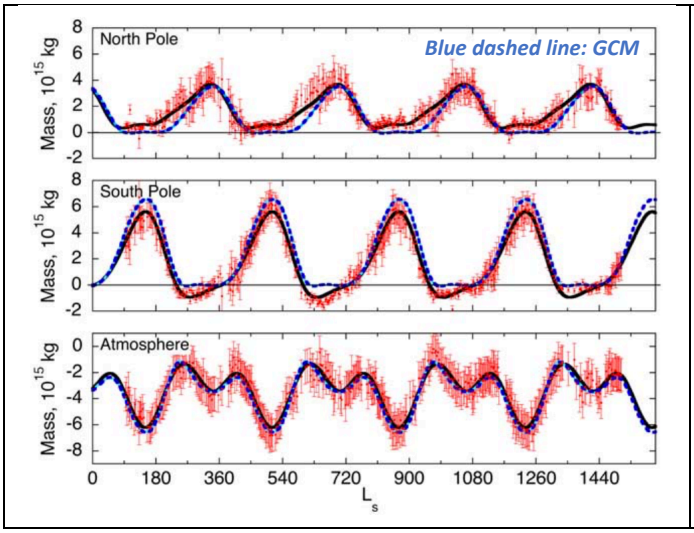

Figure 22 : Mars seasonal CO_2 mass budget derived from the seasonal variations of the gravity field determined with MGS and ODY tracking data (Smith et al., 2009). Red dots with error bars are time series determined every 5 days, the black solid line is the best fit of annual and sub-annual variation, and the blue dashed line corresponds to predictions from Global Circulation Model (GCM) simulations (Haberle et al., 1999). L_s is the angular position of the Sun over the course of one Martian year (L_s=0° at Northern Spring/Southern fall season).

This mass budget estimation from measurements of the gravity variations show a deficit of mass deposits at the South pole (winter) and an accumulation of CO_2 ice at the North pole (fall), which occurs sooner than predicted by Global Circulation Models (GCM) (Forget et al., 1999; Haberle et al., 1999) of the Martian atmosphere (Figure 22). However, this slight discrepancy between tracking data and GCMs is just at the limit of the error bars on the seasonal mass budget estimate at polar caps (Figure 22), preventing a better constraint of the GCMs (Haberle et al., 2008). These error bars arise from the fact that the even zonal harmonics variations are not resolved from the tracking data (e.g. Konopliv et al., 2006, Marty et al., 2009, see Figure 23). This lack of resolution is due to the error of the reconstructed orbit (1-2 meters, see Figure 16 and Section 1.5.1.2), which prevents to detect the very weak signal of these gravity variations on the orbit (5 cm, see Figure 23). These small orbital perturbations are also due to the fact that the even zonal harmonics generate perturbations proportional to the cosine of the inclination, and are thus particularly attenuated for a polar orbit (see Appendix B). On the other hand, the odd zonal harmonics orbital perturbations are proportional to the sine of the inclination (see Appendix B), thus yielding seasonal orbital perturbations variations of up to 70 cm (Figure 23), which are detectable with an orbital error of around 1-2 meters.

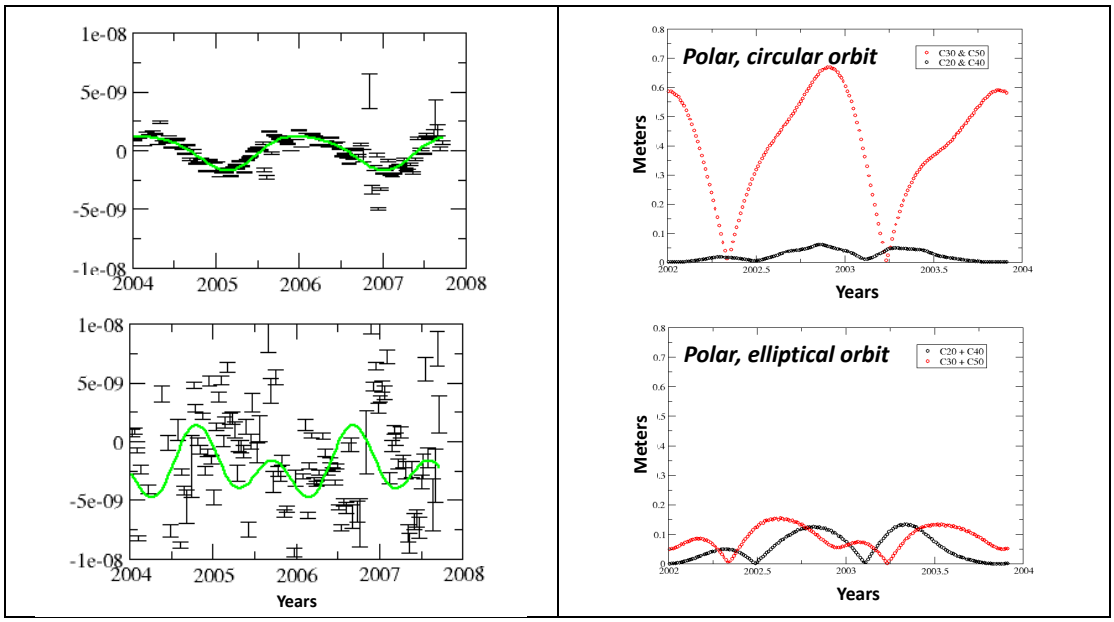

Figure 23: (Left) time series of seasonal variations of the odd (top) and even (bottom) zonal harmonics from MGS and ODY tracking data (similar results are obtained by Konopliv et al. (2006)). Adapted from Marty et al. (2009). (Right) orbital perturbations expected from the seasonal variations of the first two even (C_{20} and C_{40}) and odd (C_{30} and C_{50}) zonal harmonics for (top) an MGS-like orbit and for (bottom) a MEX-like orbit over one Martian year. Simulations performed with GINS.

I tried to improve the solution of the seasonal gravity variations by adding the tracking data of MEX but the orbital signal of these seasonal variations has an amplitude of 10 cm (Figure 23), which is obviously due to the larger semi-major axis *a* of the MEX orbit which reduces the signature of the zonal harmonics (proportional to $(R/a)^l$, see Section 1.2.2 and Appendix B). It is obviously impossible to detect these small orbital perturbations with a MEX orbit error of 20 meters on average (see Figure 16 and Section 1.5.1.2). The poor sensitivity of the MEX orbit to gravity seasonal variations especially corresponds to periods when the pericenter is not tracked (i.e. the uncertainty on zonal harmonics variations significantly increases for these periods, Figure 24). This "non-result" perfectly illustrates the importance of tracking the low-altitude pericenter passes of a spacecraft on an elliptical orbit in order to retrieve the small gravity signal.

More recently, the MRO tracking data have been used to improve the solutions of the seasonal gravity field since the semi-major axis of MRO is lower than those of MGS and ODY (Table 1). But the even harmonics variations still remain unresolved (Marty et al., 2013; Genova et al., 2016).

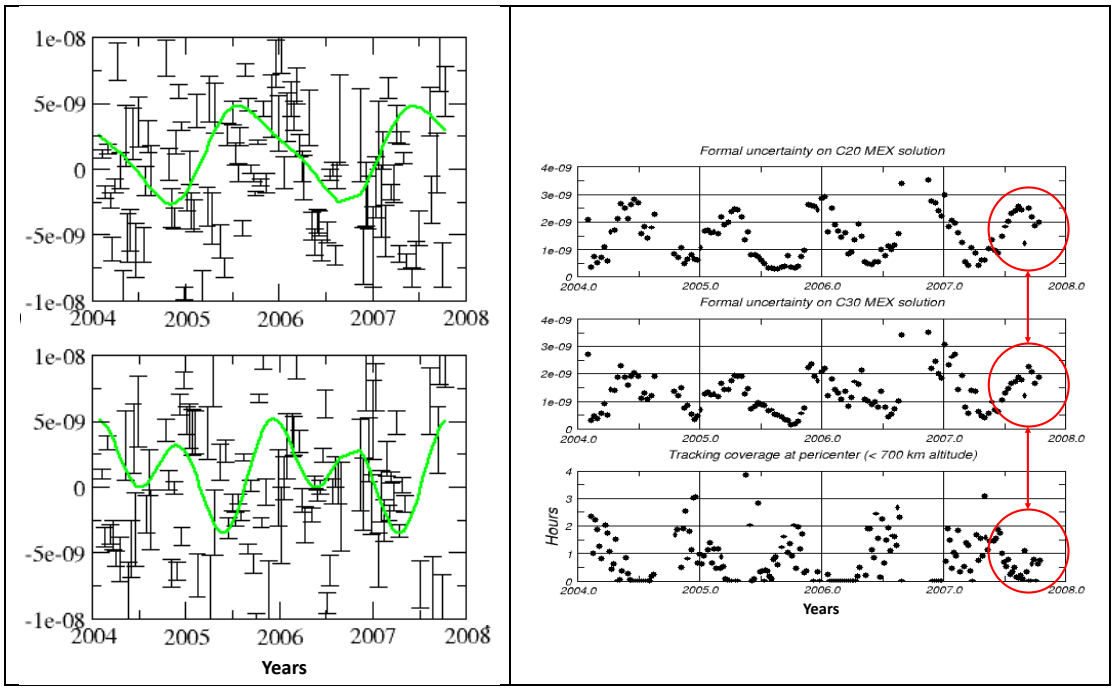

Figure 24: (Left) time series of odd (top) and even (bottom) zonal harmonics obtained with MEX tracking data (adapted from Rosenblatt et al., 2008). (Right) uncertainty of time series of even C_{20} (top) and odd C_{30} (middle) zonal harmonics from the MEX tracking data compared to the availability of tracking at pericenter passes (bottom). Red circles show an example of degradation of the uncertainty when periods without tracking at pericenters occur.

1.5.3 The gravity field of Phobos and Deimos

The mass of Phobos has been estimated using either flyby or secular approaches. The first approach consists in tracking the spacecraft along its Martian orbit when moving close to Phobos and the second consists in accumulating the tracking data of the Martian spacecraft while moving further away from Phobos. In that case, the gravitational pull of Phobos on the spacecraft is very weak but can be retrieved from the stacking of numerous data-arc normal matrices (like the gravity field of the planet, see section 1.5.2.1).

The mass of Phobos was not well determined from the tracking data of previous spacecraft (Mariner-9, Viking-1 and Phobos-2, Figure 25) using both approaches (all the solutions differ by about 40%, Figure 25). Although Viking-1 performed several flybys of Phobos at close distance (as close as 90 km), significant discrepancies arose among different authors (Christensen et al., 1977; Tolson et al., 1977; Williams et al., 1988)[40] (Figure 25). In addition, these flyby solutions disagree either with the secular solution from Smith et al. (1995)[41], using Viking 1 & 2 and Mariner-9 tracking data or from Yuan et al. (2001) using additional MGS tracking data, as well as with the solution from Kolyuka et al. (1990) and Berthias (1990) using Phobos-2 tracking data. The Russian spacecraft orbited Mars, during a couple of days in 1989, on a quasi-

[40] We have shown with GINS simulations that these discrepancies come from the noisy S-band data used to track Viking-1 (Kudryashova et al., 2015).
[41] It was the first attempt to get a Martian moon mass solution from the spacecraft secular orbit perturbations.

synchronous orbit with Phobos so that it flew at about 190 km from the largest moon of Mars[42].

The mass of Deimos was actually determined by one single very close flyby of Viking-2 (30 km from the surface, Hildebrand et al., 1979: Williams et al., 1988).

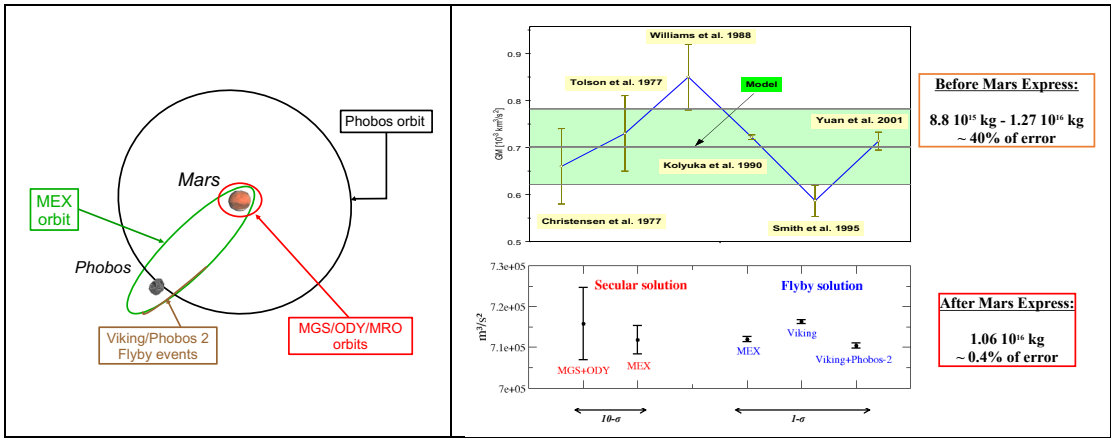

Figure 25: (Left) Orbits of Phobos and of the Martian spacecraft used to determine its mass. All spacecraft have a polar orbit except Phobos-2, which orbited Mars in the equatorial plane as does Phobos, and Viking-1 which orbited in a plane inclined at 40° above the equator. (Right top) the determination of the mass (GM) of Phobos before MEX (Courtesy V. Lainey) and (right bottom) after MEX. The MGS+ODY secular and Viking flyby solutions are from Konopliv et al. (2016), the Viking+Phobos-2 flyby solution is from Jacobson (2010), the MEX secular and flyby solutions are from Rosenblatt et al. (2008) and Andert et al. (2010), respectively.

Modern spacecraft are tracked with less noisy X-band frequencies, and on average, the highly elliptical orbit of MEX comes closer to Phobos and Deimos than the tighter orbits of MGS, ODY and MRO (Figure 25). The orbit of MEX is thus more perturbed by the gravitational attraction of the Martian moons than the orbit of MGS, ODY and MRO[43]. As a consequence, a more accurate determination of the Martian moons' masses is possible by stacking MEX's data-arcs. I thus implemented into GINS software the partial derivatives of the Doppler tracking data with respect to the GM of the moons. I validated it with the MEX tracking data to (re)-determine the mass of Phobos and Deimos (Rosenblatt et al., 2008).

The MEX secular solution yielded a major improvement in the determination of the mass of Phobos since the error was reduced by at least two orders of magnitude in comparison to previous estimates (Rosenblatt et al., 2008, Figure 25). MEX also performed a couple of close flybys dedicated to gravity (Andert et al., 2010), which yielded a new flyby value of Phobos mass in agreement with the secular solution within the respective error bars (Figure 25). This improvement of Phobos mass determination is not only due to the X-band tracking data but also to a new and more precise Phobos ephemeris (Lainey et al., 2007). Indeed, as Phobos is a third body in the orbit computation of the spacecraft, its position must be known with enough accuracy to not bias the determination of the mass (Rosenblatt et al., 2008). Viking 1 & 2 and Phobos-2 tracking data were thus re-processed using a new ephemeris and a new flyby solution of Phobos mass was found (Jacobson, 2010). This solution is in closer agreement with both secular and flyby solutions of MEX than the MGS/ODY and Viking solutions

[42] Like a "permanent flyby".

[43] By applying Kaula's method to the third body gravitational potential, one can show that the mass of the moons perturbs the orbit of any Martian spacecraft mainly as secular drift of their ascending node, their argument of the periapsis and to some extent their mean anomaly. This orbital secular perturbation is proportional to $a^{3/2}$, a being the semi-major axis of the orbit.

from Konopliv et al. (2016) who used a less accurate ephemeris (Figure 25). All recently published solutions of Phobos' mass are summarized in Paetzold et al. (2014) and are about 1.06×10^{16} kg (Table 5), corresponding to a GM value of 7.11×10^5 m^3/s^2 (Rosenblatt et al., 2008), which is also the last MGS/ODY/MRO secular solution (Konopliv et al., 2016).

The MEX secular solution for Deimos' mass is in agreement with the solution from the re-processed Viking-2 flyby data (Jacobson, 2010) but its error bar is significantly larger (Rosenblatt et al., 2008). This is due to the uncertainty in MEX' orbit which prevents accurate determination of the mass of the most distant moon of Mars. The Viking-2 flyby value thus remains the best estimate (Table 5).

Images taken by MEX during its numerous flybys also helped to improve the determination of Phobos' volume (Willner et al, 2014). Improving mass and volume estimates yielded a more accurate estimation of the bulk density (Table 5). This density is lower than both Martian material and most meteoritic material (Rosenblatt, 2011), suggesting that Phobos interior is inhomogeneous with a significant amount of porosity (Andert et al., 2010; Rosenblatt, 2011) and/or some light elements like water ice (Murchie et al, 1991; Rosenblatt, 2011). The presence or absence of porosity and volatiles is a precious information to constrain the scenario of formation (e.g. Rosenblatt and Charnoz, 2012; Pignatale et al., 2018).

Bulk properties	Phobos	Deimos
Mass (in 10^{16} kg)	1.066 +/- 0.013 (1.2%)[(1)]	0.151 +/- 0.003 (1.2%)[(2)]
Volume (in km^3)	5742 +/- 35[(3)]	1017 +/- 130[(4)]
Density (in g/cm^3)	1.856 +/- 0.034	1.48 +/- 0.22

Table 5: Bulk properties of Phobos and Deimos. [(1)]Paetzold et al., (2014); [(2)]Jacobson (2010); [(3)]Willner et al. (2014); [(4)]Thomas (1993); the density is obtained from the mass and volume in the rows above.

The bulk density alone does however not indicate whether the interior of Phobos is heterogeneous or not. The knowledge of additional bulk properties is necessary, such as the amplitude of libration[44], which is slightly influenced by the mass heterogeneity inside Phobos (e.g. Rambaux et al., 2012; Le Maistre et al., 2013). Libration was measured using MEX images but its value, within its error bar of 15%, can be explained by a homogeneous Phobos interior (Oberst et al., 2014). Precise measurements of the non-sphericity coefficients of the gravity field are required, in addition to the libration amplitude, to better constrain mass heterogeneities inside Phobos (e.g. Rosenblatt and Rivoldini, 2009; Rosenblatt et al., 2010, Le Maistre et al., 2019). The second-degree harmonic coefficients C_{20} and C_{22}, and the libration amplitude, are indeed related to the principal moments of inertia of Phobos, and thus to its internal mass distribution (Borderies and Yoder, 1990).

The most recent two closest flybys of Phobos dedicated to gravity (at a distance of 90 km and 58 km) have been used to derive first estimates of C_{20} and C_{22}. They support a heterogenous Phobos interior (Yang et al., 2019) but their uncertainties (25% on the C_{20} and almost 100% on the C_{22}) are not small enough to constrain models of possible mass distribution inside Phobos (a few to ten percent of variation with respect to the homogenous value of -0.1 is indeed required by these models for the C_{20} harmonic coefficients, Rosenblatt et al., 2010; Le Maistre et al., 2019). Yang et al. (2019) also

[44] Variations of the spin rate of Phobos due to the eccentricity of its orbit around Mars.

found a GM value of 7.0765 10^5 m^3/s^2 with an uncertainty of 0.1%, which significantly differs from the previous value (Table 5).

The error on the ephemeris of Phobos can significantly bias the value of the gravity coefficients obtained with tracking data acquired during the flyby events. Indeed, using GINS, I found a C_{20} value of -0.32 with an uncertainty of 0.6% (Figure 26) which differs from the homogeneous value of -0.1 by 220%. It suggests a strong heterogeneity inside Phobos which is difficult to explain by models of its interior (e.g. Rosenblatt et al., 2010), besides it has not been detected in the libration amplitude value (Oberst et al., 2014). I also found a GM value very close to the previous value of 7.11x10^5 m^3/s^2 but with an improved uncertainty of 0.02% (against 1.2%, Table 5). The discrepancy of my solution with the one by Yang et al. (2019) may be due to the fact that they used an additional close flyby (at 90 km) and a priori constraints to adjust the gravity coefficients while I did not.

A possible explanation for the large C_{20} value, I found, is that it is strongly biased by the error in Phobos ephemeris. Indeed, the bias on the C_{20} estimate is even larger when another ephemeris is used (ESPaCE-IMCCE, Figure 26), suggesting that the error in Phobos ephemeris has a significant effect on Phobos C_{20} gravity coefficient estimate (and also on the GM).

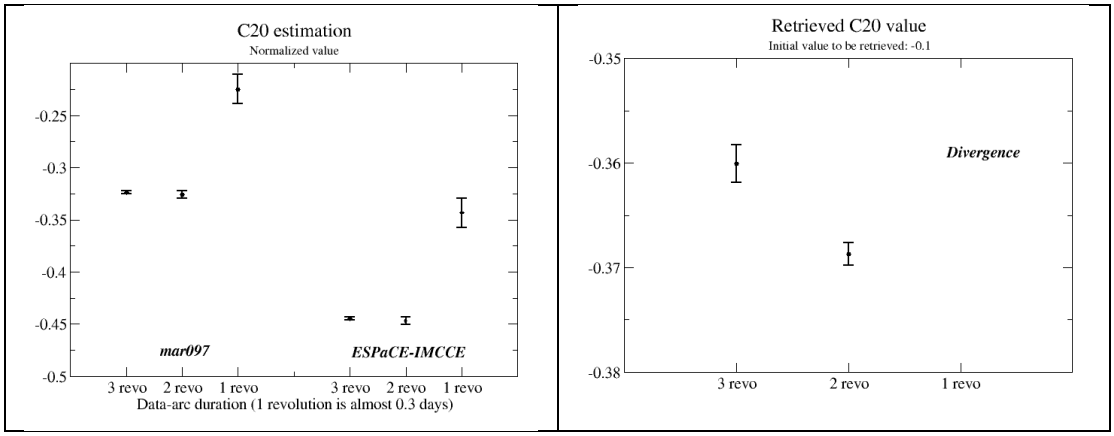

Figure 26: (Left) estimation of the C_{20} harmonics of Phobos gravity field from the MEX close flyby (58 km). Different data-arc durations have been considered (1, 2 or 3 MEX orbital revolutions). The tracking is continuous. GINS software was used. (Right) Simulation of the Phobos C_{20} estimation from the MEX close flyby configuration. Phobos position was perturbed by 1 km. Simulations performed with GINS.

In order to check this explanation, I simulated with GINS the tracking data of the MEX flyby using the observed noise on the 2-way X-band data. I used initial values of Phobos GM as given in Table 5 and of Phobos C_{20} value (homogeneous value). Then, I fitted the values of Phobos GM and C_{20} from these simulated tracking data but I included a bias of 1 km in the Phobos ephemeris, which is the estimated error on Phobos mar097 ephemeris at the time of the flyby (Jacobson, 2010). I obtained simulated values of GM, which is slightly different (0.1%) from the initial value, and of C_{20} as -0.36 or -0.37, depending on the data-arc duration (Figure 26). This simulated estimate differs by 260% from the initial value of -0.1. The result of this simulation is very similar to the result obtained with the true data, strongly suggesting that indeed the Phobos position is not known accurately enough to get an accurate solution for Phobos' gravity field with only one close flyby.

I performed the same simulation by reducing the bias on Phobos ephemeris and found that an ephemeris error better than 10 meters is necessary in order to reduce the bias on the C_{20} to less than 1%, which is the error needed to better constrain internal

models of Phobos interior (e.g. Rosenblatt et al., 2010). The 10 meters level of error on the ephemeris of Phobos is however a very challenging goal to reach with astrometric observations (V. Lainey, pers. Comm., 2014).

1.6 Conclusion on the gravity of the Martian system

The perturbations on the spacecraft trajectory due to the gravity field of a planet depends on its orbit. In order to improve the planet gravity field solution, the choice of the spacecraft orbit is thus as important as the accuracy and the coverage of the tracking data. A low-altitude, near-circular and near-polar orbit tracked as often as possible is the most efficient implementation to map a gravity field with high spatial resolution and accuracy. Mars has benefited, and still does, of NASA's spacecraft with such orbit and tracking to achieve a spatial resolution of 110 km, which is an improvement by a factor of six with respect to the gravity maps determined with the first Martian orbiters. This gravity map is being used to probe shallower interior of Mars in order to provide new constraints on the local structure of the crust and lithosphere (see Wieczorek 2007, for a useful review).

The determination of the k_2 Love number of Mars from tracking data of NASA's orbiting spacecraft is the most important result brought by planetary geodesy to understanding the interior structure of this planet and the consequences on its evolution (e.g. Rivoldini et al., 2011). A fluid core today has several implications about its thermodynamics state and especially the presence of light elements such as sulfur which delays the formation of the inner core, which is consistent with the absence of magnetic dipole today. The k_2 Love number does however not help to conclude whether there is an inner core (whose formation would have ceased) at the center of Mars or not.

The use of ESA's MEX tracking data has been particularly useful in improving our knowledge of Phobos' mass. It was confirmed that the density of the moon is low compared to the density of the rocky materiel it could be composed of. At the beginning of the 2010's, questions about the actual nature of Phobos motivated me to lead a collaborative research project on the formation of the Martian moon system (see Section 2).

I have participated to the processing of NASA's spacecraft tracking data and have especially worked on ESA's spacecraft tracking data, extending the ability of the GINS software to analyze them. In this manuscript, I have not presented my work using ESA's Venus Express tracking data to determine the density of the thermosphere at altitudes between 160 and 180 km above the North pole of Venus (Rosenblatt et al., 2012). Although accelerometer onboard spacecraft provide a richer dataset for atmospheric density at low orbital altitude (Mueller-Wodarg et al., 2016), POD provides useful information for long-term monitoring of the exosphere (up to 400 km for Mars, Bruinsma et al., 2014).

1.7 Perspectives and research project

My research project for the next decade is related to the missions offering opportunities for planetary geodesy (Figure 27). In what follows I describe some of these planetary geodesy studies aiming to improve the time variable gravity of Mars (on Exomars2016 mission, not shown on Figure 27) as well as the rotation and orientation of Mars (on ExoMars2020 mission), also aiming to improve the gravity field of Venus (on EnVision candidate mission) and of Phobos (on MMX mission), and aiming to determine the gravity of a binary asteroid system (on HERA mission).

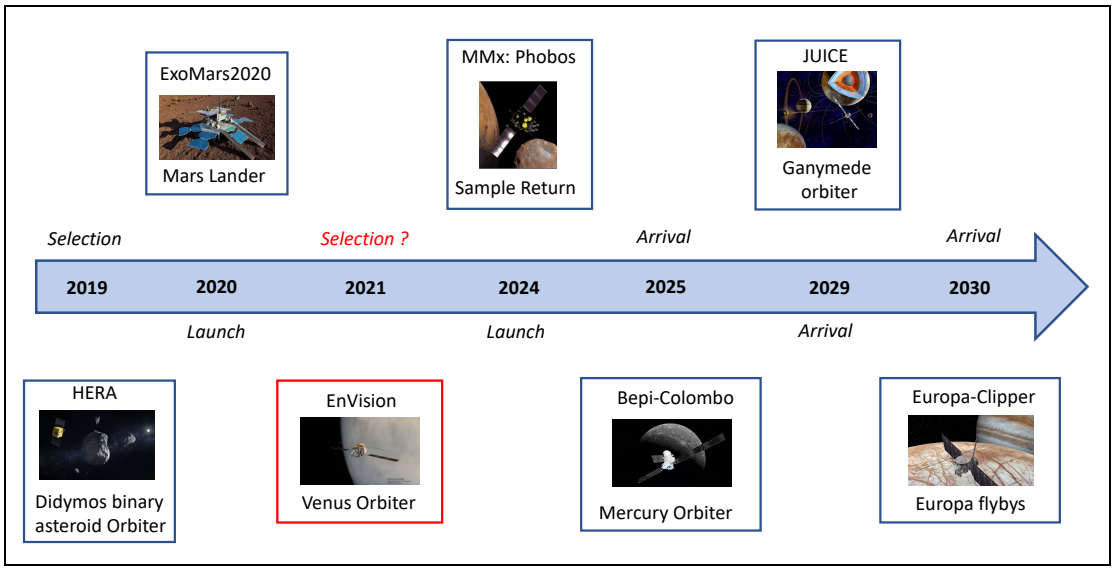

Figure 27: Solar system exploration missions with opportunities for geodesy experiments over the coming decade.

1.7.1 Mars seasonal gravity variations

We saw that the seasonal even zonal harmonics are poorly resolved by the polar orbit of the current Martian spacecraft (see section 1.5.2.3). A non-polar orbiter, with altitudes similar to those of MGS, ODY or MRO, would be very useful to improve the situation. ESA's Exomars2016 (TGO) spacecraft has a near-circular orbit at an altitude of 400 km and an inclination of 74 degrees[45]. The orbital signature of the even zonal harmonics should be enhanced by roughly a factor of five because of this inclination with respect to the polar orbits[46]. As for MGS and MEX-like orbits, I simulated with GINS this orbital signature on a TGO-like orbit (Figure 28).

[45] NASA's MAVEN spacecraft has also an inclination of 74° but an elliptical orbit which unfortunately prevents to accurately determine even harmonics variations. As for TGO this inclination has been chosen to remotely sensed the atmosphere of the planet at various local times.
[46] i.e. the ratio of the cosine of TGO and MGS orbit inclinations (see Appendix B).

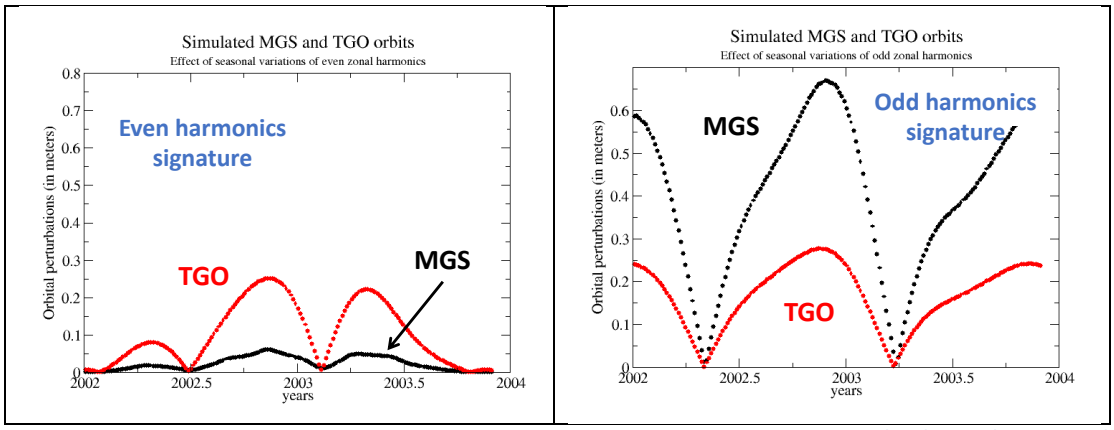

Figure 28: Orbital perturbations due to the expected seasonal variations of the first two (left) even (C_{20} and C_{40}) and (right) odd (C_{30} and C_{50}) zonal harmonics for an MGS and TGO-like orbit. Simulations performed with GINS.

The orbital perturbations due to the seasonal variations of the even zonal harmonics on an TGO-like orbit are up to 25 cm compared to about 5 cm for an MGS-like orbit. This enhanced signal will help improving the current solution of the even zonal harmonics, although an orbit error of 1 meter or even better is required. The odd harmonics signature is however five times weaker than on an MGS-like orbit[47], and the normal matrix of TGO tracking data should be merged with those of MGS/ODY/MRO to improve the seasonal variations of the Mars gravity field. If all the conditions are met, it will be the first ever merging of precise orbits with different inclinations for Mars gravity field.

This is a high-standing challenge for POD, and I am currently working on it using the GINS software. My position of Guest Investigator on the TGO science investigation team gives me the access to the tracking and ancillary data needed to reach my goal of improving Mars seasonal gravity variations.

The gravity field of planets, including their time variations, are modeled using the spherical harmonics approach. Detecting very fine time variations of the lowest zonal harmonics of the Mars gravity field is however very challenging given the state-of-the-art POD. Alternatively, we could use a spatial approach like the LOS inversion of numerous tracking passes (e.g. Barriot et al., 1998) or the *mascon* approach (Lemoine et al., 2007). Such approaches seem promising for the variations of the CO_2 mass deposits at polar caps. The convergence of the polar orbiter tracks over the poles indeed offers a tight spatio-temporal sampling of the polar caps with tracking passes. The mass variations could be monitored with a much better sampling rate than possible by the spherical harmonics approach. I will use the mascon method and will adapt to Mars the software developed for Earth (e.g. Schrama et al., 2014; Scanlon et al., 2016; Parisi et al., 2020).

The goal is to challenge the GCM in their ability to reproduce CO_2 condensation/sublimation at finer time and spatial scales (than allowed by the lowest zonal harmonics and seasonal scales) by focusing at the polar caps. The condensation/sublimation rates are indeed not driven only by the atmospheric temperature and pressure over the polar caps but also by the thermal inertia of the underlying soil and to some extent by the diurnal cycle (Haberle et al., 2018).

[47] The ratio of the sine of the inclination of the two orbits (see Appendix B).

1.7.2 Mars rotation and orientation variations

Planetary geodesy also aims to measure the variations of the rotation rate and orientation of the rotation axis of the planet, i.e. its proper motion. These variations are the response of the planet to external gravitational sollicitations. The internal mass distribution however modulates the response, which can be used in turn to probe the interior of the planet (in addition to the gravity field). So far, only the precession rate of Mars rotation axis was measured using a direct radio link between a lander and Earth's stations (e.g. Folkner et al. 1997, Le Maistre et al., 2012, Kuchynka et al., 2014). As shown in section 1.4.1 (Figure 12), POD can provide estimation of this parameter as well (e.g. Konopliv et al., 2006; 2016). Konopliv et al. (2016) even merged both lander and orbiter tracking data to achieve the best precession rate estimation of Mars rotation axis. The precession rate is related to the principal moment of inertia (MOI), which reflects the radial mass distribution inside the planet. In particular, its value is related to the density of the core. Using both precession rate and k_2 Love number it is hence possible to more tightly constrain the deep interior structure of Mars (e.g. Rivoldini et al., 2011).

A step forward in probing the deep interior of Mars is with both InSight (Folkner et al., 2018) and Exomars2018 (Dehant et al. 2020) missions[48]. Both landers are equipped to establish a direct 2-way radio link in X-band over at least one Martian year. The goal is to precisely measure the nutations of the rotation axis of the planet in order to better constrain the state (presence or absence of an inner core), size and shape of the core, and also mantle properties (e.g. Verhoeven et al., 2005; Le Maistre, 2013). The basic method is to monitor the position of a lander on Mars surface with respect to Earth's stations, which are accurately positioned in the inertial reference frame (ICRF). However, the relative positioning of a Martian reference point has to be as precise as 1 cm over annual and sub-annual periods in order to detect the expected signature of the Martian core on the nutations (e.g. Le Maistre, 2013). It is again a very challenging planetary geodesy experiment.

Merging with POD may help to improve further the lander solution (as done for precession), although nutations have not yet been retrieved from POD (e.g. Konopliv et al., 2006). However, there is a project to implement this option into GINS in order to take advantage of stacking tracking data from MGS to TGO. The very long period (at least ten Martian seasons) should help detecting very tiny seasonal signals in the reconstructed spacecraft orbits.

1.7.3 The gravity field of Venus (EnVision)

The mission designs to Venus are under study at both NASA and ESA in the framework of their programme: VERITAS and DaVinci on NASA side and EnVision on ESA side. Similar to VERITAS, EnVision is a spacecraft that will orbit the planet while DaVinci will probe the atmosphere of the planet. The goals of EnVision are to improve the knowledge of the surface, interior and atmosphere of Venus to understand its geological and climatic evolution and to detect possible geological activity today (Ghail et al., 2020). The interior will be probed using a planetary geodesy experiment consisting in tracking the EnVision spacecraft from Earth as done for the Martian

[48] The Exomars2018 mission launch has been recently postponed to 2022.

spacecraft. The goal is to improve the spatial resolution of the gravity field obtained with NASA's Magellan and PVO spacecraft (Konopliv et al., 1999) in order to study the possible variations of the crust and lithosphere thicknesses for various geological features (e.g. Anderson and Smrekar, 2006). The current gravity solution contains indeed large areas of very poor resolution (Figure 28) preventing the detection of the possible geographical variations in the gravity anomalies. In addition, the k_2 Love number has an error of 22%, which prevents concluding whether the core is liquid, partially liquid or even solid (Dumoulin et al., 2017, see Figure 28).

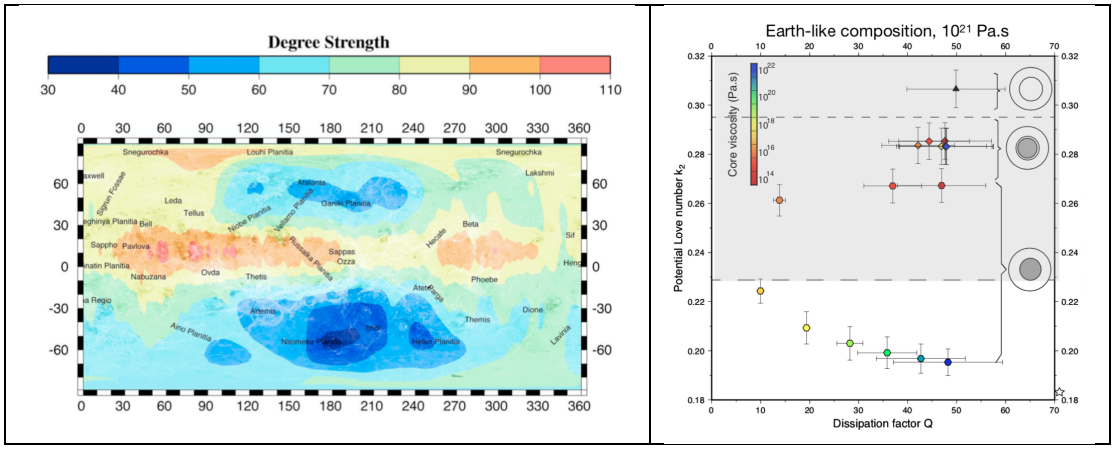

Figure 28: Current knowledge of Venus gravity field: (left) map of the degree strength of the current Magellan's gravity solution. The best spatial resolution is 110 km (red colors) and the worst 620 km (blue colors) (from Anderson and Smrekar, 2006), (right) Venus interior models and the k_2 Love number constraint with an error of 22% (gray shaded area on the figure) (adapted from Dumoulin et al., 2017).

The proposed gravity experiment aims to map the gravity field with a spatial resolution of about 200 km (degree strength of 90) everywhere and to get a k_2 Love number solution with an error better than 3% (Dumoulin et al., 2020).

I thus performed numerical simulations using GINS and DYNAMO to study the feasibility of this gravity experiment in the framework of the Phase-A studies of the EnVision project (Rosenblatt et al., 2019a,b; Rosenblatt et al., 2020).

The two important points for a successful gravity experiment are the choice of the orbit and the tracking coverage and accuracy (see section 1.3.4). The foreseen orbit for EnVision is near-polar (88° inclination) and slightly elliptical (220x470 kmxkm) with a periapsis position located around latitude 65° South. The best gravity resolution is therefore expected in the southern hemisphere and the worst in the northern hemisphere. The tracking is a 2-way link with a X-band uplink and a dual frequency X-Ka downlink. This Ka-band downlink is foreseen for high-rate downloading of the other instrument data. It offers however the opportunity to remove the solar plasma noise on the downlink by combining both X and Ka bands (since the plasma noise depends on the frequency of the radio signal, JPL note 202, 2019).

I performed an end-to-end Doppler noise budget and found an expected noise level as low as 0.045 mm/s at 10 seconds count time at inferior conjunction and rising up to 2 mm/s at superior conjunction (Figure 29). These periods of very noisy Doppler signal occur every 584 days (synodic periods, see Table 2) so that they are unexploitable during one month around these events. There are two such events over the mission science phase of 4 Venusian days (each Venusian day is 243 Earth's days) (Figure 29). In spite of the X-Ka downlink, the solar plasma is the dominant source of noise because of both the X-band uplink and the angular proximity of Venus to the Sun as seen from Earth (Figure 29).

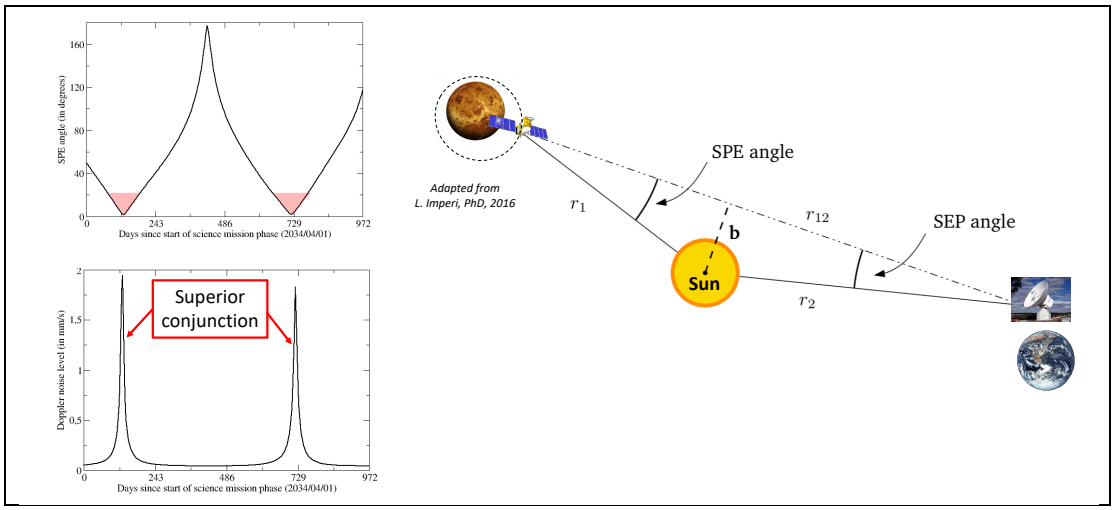

Figure 29: Doppler noise budget for EnVision gravity experiment simulations (2-way X/X-Ka Doppler link): (left top) Sun-Earth-Probe (SEP) angle vs time, (left bottom) Doppler noise level vs time, (right) representation of the Earth-Sun-Probe configuration (not at scale).

The tracking will be performed during the downlink telemetry of the instruments of the payload for at least 7 hours per day. As the orbital period is about 1.5 hours, the tracking will cover almost half of the orbital revolutions per day sufficient to sample the surface with a resolution of at least 70 km (i.e. maximum cross-tracks separation).

I simulated Doppler data on the basis of the EnVision orbit and of my Doppler noise budget for the science phase mission. I used as initial value, the Magellan's gravity field and the associated k_2 Love number (i.e. 0.295, Konopliv and Yoder, 1996). I then fit these simulated tracking data as done with true tracking data. I used as an a priori gravity field a version modified from the initial Magellan's solution by adding noise on each harmonic, and by changing the k_2 value from 0.295 to 0.1. I also added one inertial wheel desaturation event per day with a residual acceleration of about 5×10^{-6} m/s^2 (corresponding to a velocity impulse of 1 mm/s). This event occurs however twenty minutes before the beginning of a tracking pass in order to better constrain the generated acceleration with tracking data. I performed this fit to the noisy simulated Doppler data over successive four days data-arcs covering the entire science mission phase (four Venusian days). I then stacked together the individual normal matrices of each data-arc to obtain the global normal matrix as for the reconstruction of the gravity field with true data (see section 1.5.1). I finally inverted the global matrix to derive a simulated gravity and k_2 Love number solution that I compared with the initial values to assess the ability of the EnVision gravity experiment to improve the determination of the gravity field of Venus. The results of these simulations are summarized on Figure 30.

The spatial resolution of the Venus gravity field is significantly improved with an average degree strength of 100 (190 km) against 70 (270 km) for the current Magellan's solution (Figure 30). As usually done with true data, I applied a Kaula's constraint to stabilize the inversion of the global matrix. It can clearly be seen in the error spectra that this constraint influences the solution above harmonic degree of 80, meaning that all degrees below 80 are only solved from the information contained in the tracking data. Beyond the harmonic degree of 100 all the information on the harmonic coefficients are derived from Kaula's constraint (Figure 30).

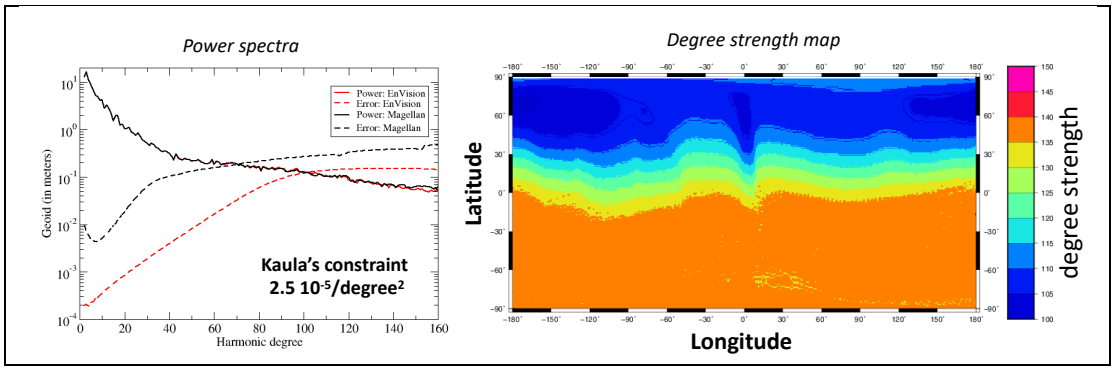

Figure 30: Results of the simulation of Venus gravity field recovery with EnVision tracking data: (left) comparison of power and error spectra per harmonic degree between the initial Magellan's and the simulated EnVision solutions, (right) map of the degree strength of the simulated EnVision solution.

The degree strength map shows that the poorest resolved areas are in the northern hemisphere corresponding to the highest altitude part of the orbit. This corresponds however to the harmonic degree of 90, which is the goal to be reached by the EnVision gravity experiment. The best resolved areas (up to harmonic degree of 140) cover all the southern hemisphere (Figure 30). The spatial sampling of 70 km is however expected to limit the spatial resolution to harmonic degree of 135 (see section 1.3.4). The drift of the orbital plane actually shifts the orbital tracks by 30 km in longitude every Venusian day. This shift helps to partly compensate the gaps created by the spatial sampling of 70 km, thus improving the expected spatial resolution of the gravity solution.

Such a high resolution of the EnVision gravity map would for the first time allow to detect the gravity signature of Coronae (average size of 300 km), which are puzzling geological features only observed at Venus surface. The initial value of the k_2 Love number is retrieved with an error of 0.15% which is well within the required error of 3% in order to better constrain the state and size of the core.

These results will not be significantly affected if the Doppler noise is increased by considering a single X-band on the downlink because a favorable Doppler geometry covers all the globe and the spacecraft orbit is mainly perturbed by the gravity field. The EnVision case perfectly illustrates that the orbit is as important as the tracking coverage and accuracy to retrieve a highly resolved gravity field. Changing this orbit (by increasing the semi-major axis or changing the inclination and the position of the latitude of the pericenter) would have serious consequences on the performance of the gravity experiment. The EnVision mission is still under Phase-A studies. The gravity experiment needs further simulations to take into account the effect of non-gravitational forces, especially the drag at the lowest altitude part of the orbit, which perturbs the recovery of the highest harmonics that generate small orbital perturbations (see section 1.2).

Envision is currently in competition with two other candidates, and the final selection will be announced in June 2021. If selected the EnVision mission will be launched in 2032 and should begin its science phase on April 1st 2035.

1.7.4 The gravity field of Phobos (MMX)

In Section 1.5.3 we saw that the gravity field of Phobos is difficult to obtain with a few flybys (even at close distance) because the ephemeris of Phobos is not accurate enough. A new opportunity to fix this issue will occur soon with the Mars Moon eXplorer (MMX) mission that JAXA plans to launch in 2024 (Usui et al., 2020). This ambitious mission aims to bring back to Earth a sample from the soil of Phobos.

During the different phases of the mission, the spacecraft will spend several months in a quasi-synchronous orbit with Phobos at a very close distance of about 50 km with the possibility of performing flybys as close as 2 km. It offers the opportunity to determine accurately the gravity field of Phobos by performing adjustment of both gravity field and ephemeris. The spacecraft payload will also have a LIDAR (Usui et al., 2020), which could be used to have a range measurement between the spacecraft and the surface of Phobos in order to better separate the ephemeris error perturbation and the gravity signal in MMX spacecraft POD. Such an ambitious gravity experiment requires simulations, given the mission operation constraints, in order to assess the performance that could be reached on the determination of the gravity field of this small body.

The mission will also perform several close flybys of Deimos allowing the improvement of estimations for its mass and thus to check its bulk density value. This density is lower than Phobos density, which raises the question whether Deimos might have a different origin compared to Phobos (Witasse et al., 2014).

1.7.5 The binary asteroid Didymos (HERA)

A binary asteroid system (the Didymos system) will be visited for the first time by a spacecraft (Figure 27). The scientific objectives of this mission are to understand the formation of such binary systems (e.g. Walsh et al., 2008). The knowledge of the internal structure is needed such as the porosity content in the secondary (Didymoon) since formation models predict high porosity inside the secondary if formed from material of the primary (Didymain) (Walsh et al., 2008). Didymoon bulk density is thus an important parameter of the system to understand its formation.

The mass of the Didymos system can be estimated from Earth's based measurements of the Didymoon orbital motion, but the mass ratio between the Didymain and Didymoon cannot be determined with high precision. The most direct way to improve the situation is to implement a radio science experiment in order to precisely measure the mass of Didymoon (Michel et al., 2016). This experiment could simply use the radio transponder of the navigation system to perform 2-way tracking of the spacecraft, nominally in X-band as for modern spacecraft. This experiment needs however the best spacecraft orbit in order to get a precise estimation of the mass of Didymoon.

The problem is far from easy as orbiting around each body of the system is too risky for a spacecraft given the distance of about 1 km only between them (Michel et al., 2016). Even orbiting the system seems difficult without frequent maneuvering given the low density of the two asteroids (see Table 2, in Michel et al., 2016). It is a problem similar to the Rosetta spacecraft around the comet 67P/Tchourioumov-Guerassimenko.

The easiest trajectory to study the system would be to follow it with the spacecraft at a relatively large distance and to perform repeated flybys at closer distances. Following this strategy, I performed a first dimensioning of the flyby problem of the Didymos system by estimating the possible precision on the mass estimation when flying by Didymain or Didymoon (Figure 31). I used the formula given in Paetzold et al. (2001), which provides the relative error on the GM estimation of a body as a function of the flyby distance and velocity, and the error on the Doppler tracking data (Equation 2):

$$\frac{\sigma_{GM}}{GM} = \frac{v_0 d}{GM}\sigma_v$$

where σ_v is the Doppler error, d is the flyby distance at closest approach, v_0 is the flyby spacecraft velocity (relative to the body), G is the gravitational constant and M the mass of the body. The Doppler noise is assumed to be 0.02 mm/s at 60 seconds count time (which is the state-of-the-art in 2-way X-band tracking, see section 1.3.3). Three values of the flyby velocity were assumed: 20, 25, 30 cm/s (Figure 31).

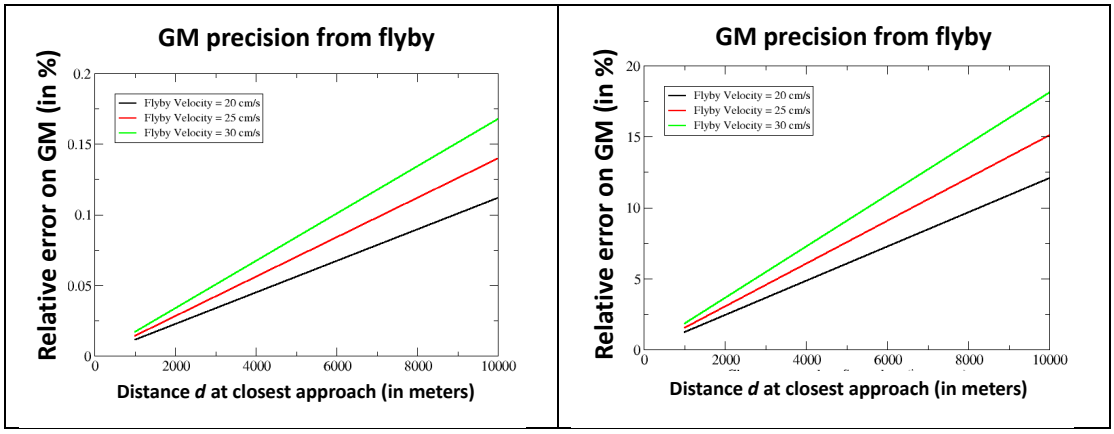

Figure 31: Estimation of the relative error on the GM determination from the tracking of a spacecraft performing a flyby of a body of the mass of (left) Didymain and (right) Didymoon. Estimation deduced from Equation 2.

When flying by Didymain, the relative error on the determination of its GM is up to about 0.17% and 0.03% at 10 km and 1 km closest approach, respectively (Figure 31). If the mass of the system is known with the same precision (from astrometric methods), it would result in a relative error on the GM of Didymoon of 40% and 6% for 10 km and 1 km flyby distance of Didymain, respectively. However, flying by Didymoon at 1 km distance would reduce the relative error on the determination of its GM to 3% (Figure 31).

This first assessment of the problem reveals the interest to target Didymoon to accurately determine its mass instead of improving the mass of Didymain.

Multiple flybys (even at 10 km distance) will improve again the determination of the mass and gravity field of the Didymos system as well as the orientation of both asteroids and the orbit of Didymoon (Zannoni et al., 2018). These authors have also shown that additional optical data of the asteroids performed during flybys will help to get accurate gravity solutions, because they reduce the biases induced by the error in the asteroid positions (as done with the asteroid Eros with the NEAR spacecraft, Konopliv et al., 2002).

1.7.6 A 'local' Doppler link?

We have seen the importance of Doppler geometry with respect to the velocity perturbations we want to measure (see section 1.3.3.). This problem of geometry is also important for the direct link from a Martian lander to Earth (the planet is indeed moving slowly in the sky of Earth-based stations offering an almost frozen geometry during the tracking pass). This problem could be avoided with a 'local' Doppler link for instance between Martian lander(s) and an orbiting spacecraft (Barriot et al., 2001). The tracking of the lander by the spacecraft would indeed offer a richer Doppler geometry at each pass. Such an experiment requires however a precise spacecraft orbit in order to extract the expected nutation signal (Duron et al., 2003; Rosenblatt et al., 2004) from the lander-spacecraft and Earth-spacecraft tracking data. Such a 'local' link also requires a precise reference frequency and clock generated aboard the spacecraft as well as a lander antenna with a sufficient gain to perform precise Doppler measurements with the spacecraft.

This 'local' link is however promising for many other geodesy experiments such as very close flybys of Phobos (Figure 32), or the Didymos system. Very close flybys pose indeed serious risks of losing the spacecraft. Cubesats could then be used to perform very close flybys, and tracking them from the spacecraft would allow precise geodesy experiments to be performed. However, as for the Martian Lander-spacecraft experiment, a precise reference frequency (and clock for dating the Doppler measurements) onboard the spacecraft is needed as well as a sufficiently good telecommunication system onboard the cubesats (i.e. high gain antenna and radio transponder) to perform precise Doppler tracking. Technical studies are still required for the adaptation of both high gain antenna and transponder to cubesats. Such an idea would offer exciting opportunities to improve the knowledge of dynamics of multiple body system.

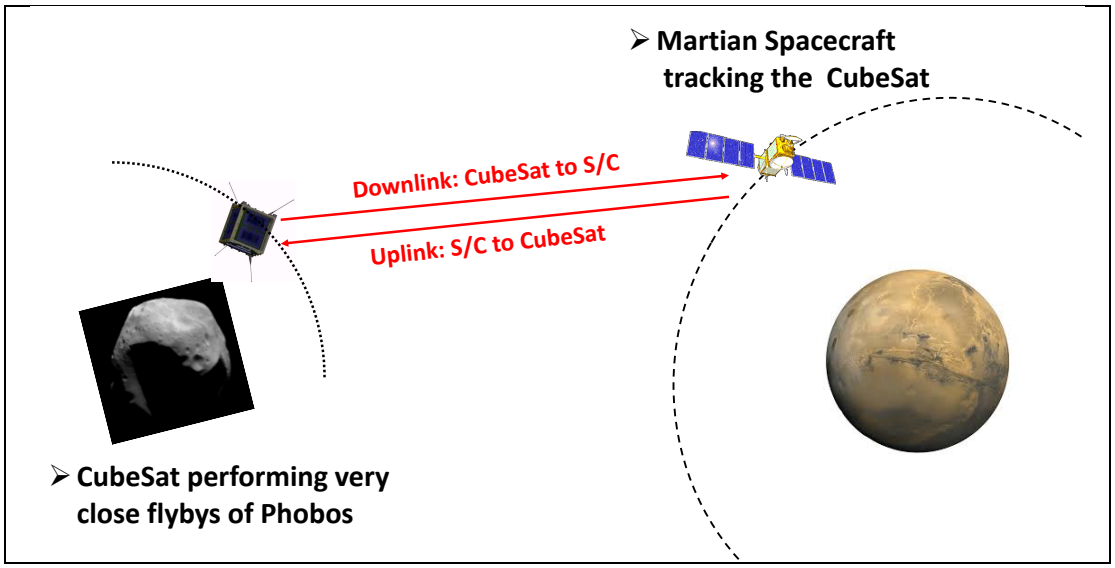

Figure 32: Illustration of a Doppler 'local link' between a spacecraft orbiting Mars and a cubesat performing very close flybys of Phobos.

1.8 Appendices.

1.8.1 Appendix A: The Keplerian motion

In the 2-body problem (point mass representation of both planet and spacecraft), the spacecraft and the planet orbit each other around the center of mass the system (or mass barycenter). The mass of the spacecraft *m* is negligible with respect to the mass of the planet *M*, so that the mass barycenter corresponds to the center of mass of the planet (or planetary center). Therefore, the spacecraft orbits around this center, following an ellipse or Keplerian trajectory. This center corresponds to one of the foci of this ellipse (Figure A-1). At any given time, the angular position of the spacecraft with respect to the planetary center is given by the true anomaly *v* counted from the periapsis position (Figure A-1). The radial distance between the planetary center and the orbiting spacecraft *r* is related to the true anomaly *v* as follows (Equation A-1):

$$r = a\frac{1-e^2}{1+e\cos(v)}$$

where *a* is the semi-major axis, *e* the eccentricity of the Keplerian ellipse and *v* is the true anomaly (Figure A-1).
The true anomaly *v* is related to the eccentric anomaly *E* as follows (Equation A-2):

$$\tan\frac{v}{2} = \sqrt{\frac{1+e}{1-e}}\tan\frac{E}{2}$$

and the eccentric anomaly *E* is related to the mean anomaly *M* (see figure A-1) through the Kepler's equation (Equation A-3):

$$E - e\sin E = M$$

The mean anomaly gives the spacecraft position at any given time *t* elapsed since the periapsis pass t_0 as follows (Equation A-4):

$$M = n(t - t_0)$$

where *n* is the mean motion which related to the orbital period *T* as follows (Equation A-5):

$$n = \frac{2\pi}{T}$$

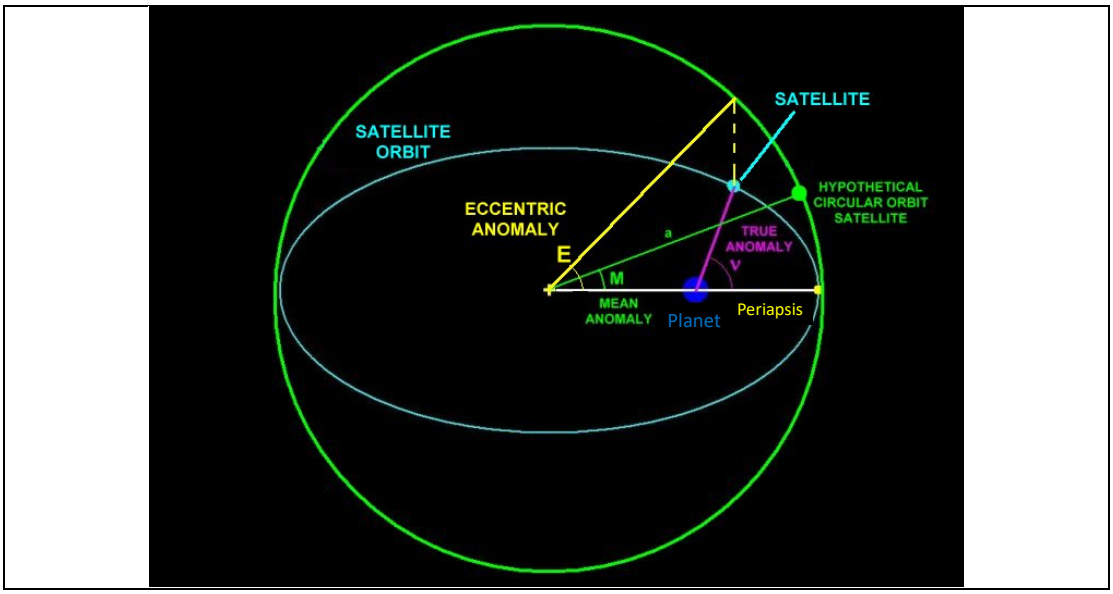

Figure A-1: Representation of the Keplerian ellipse (satellite orbit) followed by the spacecraft (satellite) orbiting the planet. The true anomaly *v* is the angular position of the satellite with respect to the center of mass of the planet counted from the periapsis position (orbital position closest to the planet). The planet is located at one of the foci of the ellipse. The eccentric anomaly *E* is the angular position of a hypothetical satellite position with respect to the center of the ellipse. The hypothetical satellite is the projection of the actual satellite position on a hypothetical circular orbit with a radius encompassing the ellipse.

The Keplerian orbital motion can be simply described as a linear relationship between the mean anomaly and the time. The third law of Kepler shows that the mean motion n is related to the semi-major axis a and the mass of the planet M (Equation A-6):

$$n^2 a^3 = GM$$

where G is the gravitational constant.

Note that for a planet with moons the mass barycenter of the system may not correspond to the planetary center. The difference in position between the two centers can significantly varies with time as a function of the orbits of the moons. For instance, this position difference can reach 90 km for the Jovian system due to the mass and the orbit of the four Galilean satellites while it reaches only a few millimeters for Mars. Typically, POD must take into account this position difference for the case of Jupiter.

1.8.2 Appendix B: The perturbed Keplerian motion (Kaula's linear solution)

1.8.2.1 The perturbing gravitational potential

The Keplerian motion is an accurate representation of the orbit of a spacecraft if the planet is spherical with a uniform density in its interior (i.e. a point mass representation can be applied). Of course, this is not the case, and a useful representation of the gravitational potential due to the mass distribution inside the planet is a spherical harmonics expansion (see Eq. 1 in section 1.2.1, and rewritten as Equation B-1):

$$U = U_0 + U_p$$

with U_0 and U_p the central and perturbing potential, respectively. U_p is due to the non-spherical component of the gravitational potential U (Equation B-2):

$$U_p = \frac{GM}{r}\sum_{l=2}^{\infty}\left(\frac{R}{r}\right)^l \sum_{m=0}^{m=l} P_{lm}(\sin\varphi)[C_{lm}\cos(m\lambda) + S_{lm}\sin(m\lambda)]$$

This perturbing potential impacts the spacecraft motion (i.e. the orbital elements: a,e,i,ω,Ω,M, see Section 1.2.2). In order to assess how the orbital elements are impacted, Kaula (1966) has re-written the perturbing gravitational potential as a function of the orbital elements (instead of the spherical coordinates of a point P outside the planet) as (Equation B-3):

$$U_p = GM\sum_{l=2}^{l\to\infty}\sum_{m=0}^{m=l}\frac{R^l}{a^{l+1}}\sum_{p=0}^{p=l}F_{lmp}(i)\sum_{q\to-\infty}^{q\to+\infty}G_{lpq}(e)\,S_{lmpq}(\omega,M,\Omega,\theta)$$

where $F_{lmp}(i)$ and $G_{lpq}(e)$ are the inclination and eccentricity functions, respectively (see Table 1 p. 34 and Table 2 p. 38, respectively, in Kaula, 1966), and S_{lmpq} is given by (Equation B-4):

$$S_{lmpq}(\omega,M,\Omega,\theta) = \left[\frac{C_{lm}}{-S_{lm}}\right]_{l-m\ odd}^{l-m\ even}\cos[\psi_{lmpq}] + \left[\frac{S_{lm}}{C_{lm}}\right]_{l-m\ odd}^{l-m\ even}\sin[\psi_{lmpq}]$$

and Ψ_{lmpq}, which is called the argument of Kaula (Equation B-5):

$$\psi_{lmpq} = (l-2p)\omega + (l-2p+q)M + m(\Omega-\theta)$$

with θ the celestial position of the longitude reference attached to the planet. It is related to a uniform spin rate of the planet as (Equation B-6):

$$\theta(t) = \theta(t_0) + \dot{\theta}(t-t_0)$$

This expression of the perturbing potential depends on the orbital altitude through the semi-major axis a, and on the inclination i and the eccentricity e through the inclination and eccentricity functions, respectively. It depends on the spherical harmonics coefficients C_{lm} and S_{lm} of degree l and order m and on two additional indices l and q, related to inclination and eccentricity functions, respectively.

1.8.2.2 The planetary Lagrange equations

As the gravitational force derives from a potential, on can describe the time variations of the orbital elements using the Lagrange equations (also called planetary Lagrange equations, Equation B-7):

$$\frac{da}{dt} = \frac{2}{na}\frac{\partial U_p}{\partial M}$$

$$\frac{de}{dt} = -\frac{\sqrt{(1-e^2)}}{na^2 e}\frac{\partial U_p}{\partial \omega} + \frac{1-e^2}{na^2 e}\frac{\partial U_p}{\partial M}$$

$$\frac{di}{dt} = \frac{-1}{na^2\sqrt{1-e^2}\sin(i)}\frac{\partial U_p}{\partial \Omega} + \frac{\cos(i)}{na^2\sqrt{1-e^2}\sin(i)}\frac{\partial U_p}{\partial \omega}$$

$$\frac{d\Omega}{dt} = \frac{1}{na^2\sqrt{1-e^2}\sin(i)}\frac{\partial U_p}{\partial i}$$

$$\frac{d\omega}{dt} = \frac{\sqrt{1-e^2}}{na^2 e}\frac{\partial U_p}{\partial e} - \frac{\cos(i)}{na^2\sqrt{1-e^2}\sin(i)}\frac{\partial U_p}{\partial i}$$

$$\frac{dM}{dt} = n - \frac{2}{na}\frac{\partial U_p}{\partial a} - \frac{1-e^2}{na^2 e}\frac{\partial U_p}{\partial e}$$

When U_p, the perturbing potential is equal to zero, one retrieves the Keplerian motion driven by the central term of the gravitational potential U_0. When U_p, is not equal to zero, these equations have no analytical solution but approximate solutions can be found following the perturbations approach, i.e. U_p generates perturbations of the Keplerian motion. Kaula (1966) has proposed a solution consisting of secular perturbations on which periodic perturbations superimpose (see Figure 2 of section 1.2.2). Thus, each orbital element (*OE*) varies as a function of the values of the others elements and of the spherical harmonics coefficients C_{lm} and S_{lm}, as (Equation B-8):

$$\frac{dOE}{dt} = F(a, e, i, \omega, \Omega, M, C_{lm}, S_{lm})$$

Hereafter, is summarized the steps to follow the computation of secular and periodic perturbations from Kaula's solution.

1.8.2.3 The secular perturbations of the orbital elements

The secular perturbations are obtained for $\Psi_{lmpq} = 0$, for all possible values of ω, Ω, and M. This is obtained for the following index values:

- m=0 (i.e. zonal harmonics only),
- l-$2p$=0 (i.e. even zonal harmonics only)
- q=0

Therefore, only the even zonal harmonics $C_{2p,0}$ generates secular variations of the orbital elements. The expression of S_{lmpq} (see Eq. B-4) becomes (Equation B-9):

$$S_{2p,0,p,0} = C_{2p,0}$$

And U_p (see Eq. B-3) becomes (Equation B-10):

$$U_p = GM \sum_{p=1}^{p\to\infty} \frac{R^{2p}}{a^{2p+1}} F_{2p,0,p}(i) G_{2p,p,0}(e) C_{2p}$$

This U_p potential only depends on the *a, e, i* orbital elements (as well as *R*, *GM* and C_{20}). Therefore, replacing this U_p expression into the Lagrange equations (Equation B-7) shows that only the ω, Ω, *M* elements vary with time, the three others elements *a, e, i* do not vary. Thus, the time derivative of ω, Ω, *M* does not depend on time *t* (so their variation depends linearly on *t*), i.e. it is a secular or precession variation of these three orbital elements). One can summarise the Lagrange equations as (Equation B-11):

$$\frac{da}{dt} = \frac{de}{dt} = \frac{di}{dt} = 0$$

and

$$\frac{d\Omega}{dt} = K_1, \frac{d\omega}{dt} = K_2, \frac{dM}{dt} = K_3$$

where K_1, K_2, and K_3 are constant that only depends on *a, e,* and *i*

then, the solution is (Equation B-12):

$$a = a_0, e = e_0, i = i_0, \Delta\Omega = \Omega_s(t - t_0), \Delta\omega = \omega_s(t - t_0), \Delta M = M_s(t - t_0)$$

where Ω_s, ω_s and M_s are the secular drifts of the so-called precessing orbit.

If one only keeps the largest and lowest degree zonal harmonics, C_{20} ($p=1$), one gets the easiest expression of U_p (Equation B-13):

$$U_p = GM \frac{R^2}{a^3} F_{201}(i) G_{210}(e) C_{20}$$

with

$$F_{201}(i) = \frac{3}{4}\sin(i)^2 - \frac{1}{2} \; ; \; G_{210}(e) = (1 - e^2)^{-3/2}$$

Placing this perturbing potential in the Lagrange equations (Equation B-4) for the ascending node Ω gives its precession rate as (Equation B-14):

$$\Omega_s = \frac{3n\cos(i)}{2(1 - e^2)^2} \left(\frac{R}{a}\right)^2 C_{20}$$

where *n* is the mean motion. The ascending node secular motion corresponds to the precession of the orbital plane around the rotation axis of the planet (i.e. the z-axis of the frame where is written the spherical harmonics expansion). As $n^2a^3=GM$ (third Kepler's law), one gets that this secular drift varies as $1/a^{7/2}$ (therefore, it slows down

with increasing semi-major axis). The precession rate Ω_s is also proportional to C_{20} and to the cosine of the inclination, so that the polar orbit has $\Omega_s=0$, which makes it not suitable to detect the C_{20} coefficient from the reconstructed variations of the spacecraft orbital velocity (see section 1.5.2.3). One can similarly compute the secular rate ω_s and M_s and shows that there also proportional to C_{20} (Kaula, 1966).

For higher degree l, the computation follows the same approach and eventually the secular drifts of the precessing orbit are proportional to a linear combination of the $C_{2p,0}$ even zonal harmonics C_{even}, also called *lumped* even zonal harmonics. The coefficients of this linear combination depend on *a, e, i* and each is proportional to $(R/a)^{2p}$ so that the effect of each higher degree even zonal harmonics on the secular drift values decreases with increasing degree. In other words (Equation B-15):

$$C_{even} = \sum_{p=0}^{\infty} F_{2p}(e,i)\left(\frac{R}{a}\right)^{2p} C_{2p,0}$$

For instance, for e~0, $F_2(0,i) = 1$ and $F_4(0,i) = \frac{5}{8}(7\sin(i)^2 - 4)$, both for Ω_s (Yoder et al., 2003).

In turn, it implies that one can only retrieve this *lumped* harmonic from the reconstructed orbit of the spacecraft, i.e. not to properly separate each even zonal harmonic. This is particularly true for the high degrees for which the associated orbital velocity perturbations are at the level of the noise of the Doppler tracking data.

1.8.2.4 The periodic perturbations of the secular motion

In the Kaula's solution, the periodic variations are obtained for $\Psi_{lmpq} \neq 0$ and superimpose on the secular variations (Figure 2 in section 1.2.2). Thus, it is assumed that only variations with time of the elements on the right side of the Lagrange equations are the secular rates (and the spin rate) (Kaula, 1966). The integration of the Lagrange equations then provides the following solutions for the periodic variations of the orbital elements (Equation B-16):

$$\Delta(a,e,i)_{lmpq} = \frac{K_{a,e,i}(a,e,i)S_{lmpq}}{\frac{d\psi_{lmpq}}{dt}}$$

$$\Delta(\omega,\Omega,M)_{lmpq} = \frac{H_{\omega,\Omega,M}(a,e,i)\left[\int S_{lmpq}\right]}{\frac{d\psi_{lmpq}}{dt}}$$

where $K_{a,e,i}(a,e,i)$ and $H_{\omega,\Omega,M}(a,e,i)$ are function of *a, e, i* for each corresponding orbital element and $\int S_{lmpq}$ is the integral of S_{lmpq} with respect to its argument, and (Equation B-17):

$$\frac{d\Psi_{lmpq}}{dt} = (l-2p)\omega_s + (l-2p+q)M_s + m(\Omega_s - \dot{\theta})$$

where Ω_s, ω_s and M_s are the secular drifts of the precessing orbit and $\dot{\theta}$ the spin rate of the planet (see Eq. 3.76 in Kaula, 1966).

This solution of the periodic variations of the orbital elements show that the amplitude of these variations is proportional to their periods: The longest the period, the larger the amplitude of the periodic variations. In addition, resonances can appear for any possible combinations of the indexes *l,m,p,q* which make $\frac{d\Psi_{lmpq}}{dt} = 0$ (see Figure 3 in Section 1.2.2).

I give hereafter the steps to follow to get the periodic variations of the longest period induced by the first zonal harmonics:

The periodic variations are obtained for $\Psi_{lmpq} \neq 0$. As one looks at the longest periods and zonal harmonics, we have the following values for the *l,m,p,q* indexes:

- *m*=0 (i.e. zonal harmonics only),
- *l-2p*≠0 (i.e. odd zonal harmonics only)
- *l-2p+q=0* (long period only) → *q=2p-l*

We only consider the largest odd zonal harmonics C_{30} (i.e. *l=3*). As the index *p* is ranging from 0 to *l,* the values of the *p,q* indexes become:

- *p*=0, q=-3
- *p=1, q=-1*
- *p=2, q=+1*
- *p=3, q=+3*

As we want only the longest periods, so the smaller values of Ψ_{lmpq} we only keep:

- *p=1, q=-1*
- *p=2, q=+1*

That corresponds to the following possible values of Ψ_{lmpq} (Equation B-18):

$$\psi_{301-1} = +\omega$$
$$\psi_{302+1} = -\omega$$

and of $S_{l,0,p,2p-l}$ (Equation B-19):

$$S_{3,0,1,-1} = C_{30}\sin(\omega)$$
$$S_{3,0,2,1} = C_{30}\sin(-\omega)$$

yielding to the following expression of the potential *Up* for periodic variations with the longest period induced by the odd zonal harmonics C_{30} (Equation B-20):

$$U_p = GM\,\frac{R^3}{a^4}\Big(F_{301}(i)G_{3,1,-1}(e) - F_{302}(i)G_{321}(e)\Big)\,C_{30}\sin(\omega)$$

Thanks to the following property of the inclination and eccentricity functions (B-21):

$$F_{l,0,p}(i) = -F_{l,0,p+1}(i)$$
$$G_{l,p,-q}(e) = G_{l,p+1,q}(e)$$

this U_p expression becomes (Equation B-22):

$$U_p = -2GM\,\frac{R^3}{a^4}\left(F_{302}(i)G_{321}(e)\right)C_{30}\sin(\omega)$$

with

$$F_{302}(i) = -\frac{15}{16}\sin(i)^3 + \frac{3}{4}\sin(i)\,;\; G_{321}(e) = e(1-e^2)^{-5/2}$$

This expression of Up is then replaced into the Lagrange equations to obtain the periodic variations of the orbital elements. For instance (Equation B-23):

$$\frac{d\omega}{dt} = \frac{3n\sin(i)}{2e(1-e^2)^3}\left(\frac{R}{a}\right)^3\left[\frac{5}{4}\sin(i)^2 - 1 + \left(\frac{1}{\sin(i)^2} - \frac{35}{4} + \frac{35}{4}\sin(i)^2\right)e^2\right]C_{30}\sin(\omega)$$

$$\frac{de}{dt} = \frac{3n\sin(i)}{2(1-e^2)^2}\left(\frac{R}{a}\right)^3\left(1 - \frac{5}{4}\sin(i)^2\right)C_{30}\sin(\omega)$$

with n the mean motion ($n^2a^3=GM$). The amplitude of those periodic variations is proportional to $1/a^6$, thus lower than the amplitude of the secular variations proportional to $1/a^{7/2}$ (see Eq. B-14).
For near-circular orbit e~0, the $d\omega/dt$ expression diverges. In order to overcome this problem, we introduce the eccentricity vector such as: $p = e\ exp(-j\omega_s)=e(cos(\omega_s)-jsin(\omega_s))$ with e is the eccentricity, ω_s the secular drift of the argument of the periapsis of the precessing orbit, and j^2=-1. Then, combining the $d\omega/dt$ and de/dt expressions (see Eq. B-21), one obtains the following expression (Equation B-24):

$$\frac{dp}{dt} + j\dot{\omega}_s p = -\frac{3n\sin(i)}{2(1-e^2)^3}\left(\frac{R}{a}\right)^3\left[\left(\frac{5}{4}\sin(i)^2 - 1\right) + \left(\frac{1}{2\sin(i)^2} - \frac{31}{8} + \frac{15}{4}\sin(i)^2\right)e^2\right]C_{30}$$

The periodic variations of the eccentricity vector are proportional to the sine of the inclination and to the odd zonal harmonics C_{30}, which make the polar orbit suitable for detecting the odd zonal harmonics from the reconstructed variations of the spacecraft orbital velocity (see section 1.5.2.3).

For higher degree l, the computation follows the same approach and eventually the periodic variations of the orbital elements are proportional to a linear combination of the $C_{2p+1,0}$ odd zonal harmonics C_{odd}, also called *lumped* odd zonal harmonics. The coefficients of this linear combination depend on *a, e, i* and each is proportional to

(R/a)^{2p} so that the effect of each higher degree odd zonal harmonics on the periodic variation amplitudes decreases with increasing degree. In other words (Equation B-25):

$$C_{odd} = \sum_{p=0}^{\infty} F_{2p+1}(e,i)\left(\frac{R}{a}\right)^{2p} C_{2p+1,0}$$

For instance, for e~0, $F_3(0,i) = \frac{5}{4}\sin(i)^2 - 1$, and $F_5(0,i) = \frac{5}{16}(8 - 28\sin(i)^2 + 21\sin(i)^4)$, both for *dp/dt* (Yoder et al., 2003).

In turn, it implies that one can only retrieve this *lumped* harmonic from the reconstructed orbit of the spacecraft, i.e. not to properly separate each odd zonal harmonic. This is particularly true for the high degrees for which the associated orbital velocity perturbations are at the level of the noise of the Doppler tracking data.

1.9 Glossary

Acronym	Full Name
ADEV	Allan Deviation
AMD	Angular Momentum Desaturation
CLTC	China Satellite Launch and Tracking Control
CNES	Centre National d'Etudes Spatiales
DPODP	Double Precision Orbit Determination Program
DSN	Deep Space Network
ESPaCE	European Satellite Partnership for Computing Ephemerides
EnVision	Europe's Revolutionary Mission to Venus
ESA	European Space Agency
ESTRACK	ESA Tracking network
GEODYN	GSFC Orbit Determination and Geodetic Parameter Estimation
GSFC	Goddard Space Flight Center
GINS	Géodésie par Intégration Numérique Simultanée
HGA	High Gain Antenna
IAU	International Astronomical Union
ICRF	International Celestial Reference Frame
IERS	International Earth Rotation and Reference Systems Service
IMCCE	Institut de Mécanique Céleste et de Calcul des Ephémérides
InSight	Interior Exploration using Seismic Investigations, Geodesy and Heat Transport
ISRO	Indian Space Research Organisation
ISTRAC	ISRO Telemetry Tracking and Command network
ITRF	International Terrestrial Reference Frame
JAXA	Japanese Aerospace Exploration Agency
JPL	Jet Propulsion Laboratory
LIDAR	LIght Detection And Ranging
LOS	Line-Of-Sight
MAVEN	Mars Atmosphere and Volatile EvolutioN
MEX	Mars Express
MGS	Mars Global Surveyor
MRO	Mars Reconnaissance Orbiter
NASA	National Aeronautics and Space Administration
NEAR	Near Earth Asteroid Rendezvous
OCM	Orbit Control Maneuver
ODY	Mars Odyssey
POD	Precise Orbit Determination
ROSCOSMOS	Russian space agency
TGO	Trace Gas Orbiter
USO	Ultra-Stable Oscillator
VEX	Venus Express
VLBI	Very Large Base Interferometry
WoL	Wheel off Loading

1.10 References

Anderson F.S., Smrekar S.E., 2006. Global mapping of crustal and lithospheric thickness on Venus. Journal of Geophysical Research 111 (E8), doi:10.1029/2004JE002395.

Andert T.P., Rosenblatt P., Pätzold M., Häusler B., Dehant V., Tyler G.L., Marty J.C., 2010. Precise mass determination and the nature of Phobos. Geophysical Research Letters 37 (9), doi: 10.1029/2009GL041829.

Arnold D., Bertone S., Jäggi A., Beutler G., Mervart L., 2015. GRAIL gravity field determination using the celestial mechanics approach. Icarus 261, 182-192.

Balmino G., Moynot B., Vales N., 1982. Gravity field model of mars in spherical harmonics up to degree and order eighteen. J. Geophys. Res. 87 (B12), 9735–9746.

Balmino G., Perosanz F., 1995. Comparison of geopotential recovery capabilities of some future satellite missions. Joint symposium of the international gravity commission and the international geoid commission, Graz, Austria, September 11-17, 1994. Edited by Hans Sünkel and Ininio Marson. Berlin, New York: Springer, 1995, P. 403.

Bar-Sever Y.E., Jacobs C.S., Keihm S., Lanyi G.E., Naudet C.J., Rosenberger H.W., Runge T.F., Tanner A.B., Vigue-Rodi Y., 2007. Proceedings of the IEEE 95 (11), 2180-2192.

Barriot J.P., Balmino G., Valès N., Rosenblatt P., 1998. A 180th degree and order model of the Venus gravity field from Magellan line-of-sight residual Doppler data. Geophysical Research Letters 25, 3743-3746.

Barriot J.P., Dehant V., Folkner W., Cerisier J.C., Ribes A., Benoist J., Van Hoolst T., Defraigne P., Warnant R., Preston R.A., Romans L., Wu S., Wernik A.W., 2001. The NetLander Ionosphere and Geodesy Experiment. Advances in Space Research 28 (8), 1237-1249.

Berthias J., 1990. Analysis of the Phobos 2 radiometric data set. JPL IOM 314.6-1129.

Beuthe M., Rosenblatt P., Dehant V., Barriot J.-P., Pätzold M., Häusler B., Karatekin Ö, Le Maistre S., and Van Hoolst T., Assessment of the Martian Gravity Field at Short Wavelength with Mars Express, Geophys. Res. Letters, 33, L03203, doi:10.1029/2005GL024317, 2006.

Beuthe M., Le Maistre S., Rosenblatt P., Pätzold M., Dehant V., 2012. Density and lithospheric thickness of the Tharsis province from MEX MaRS and MRO gravity data. Journal of Geophysical Research, Vol. 117 (4), doi:10.1029/2011JE003976.

Bocanegra-Bahamon T.M., Molera Calves G., Gurvits L.I., Duev D.A., Pogrebenko S.V., Cimo G., Dirkx D., Rosenblatt P., 2008. Planetary Radio Interferometry and Doppler Experiment (PRIDE) Technique: a test case of the Mars Express Phobos fly-

by. 2. Doppler tracking: formulation of observed and computed values, and noise budget. Astronomy & Astrophysics, Vol. 609, id.A59, 11 pp., 2018.

Borderies N., Yoder C.F., 1990. Phobos' gravity field and its influence on its orbit and physical librations. Astronomy and Astrophysics 233 (1), 235-251.

Bruinsma S., Lemoine F.G., 2002. A preliminary semiempirical thermosphere model of Mars: DTM-Mars. Journal Geophysical Research: Planets (1991–2012) 107 (E10), 15-1–15-13. doi:10.1029/2001JE001508.

Bruinsma S., Forbes J.M., Marty J.C., Zhang X., Smith M.D., 2014. Long-term variability of Mars' exosphere based on precise orbital analysis of Mars Global Surveyor and Mars Odyssey. Journal of Geophysical Research 119 (1), 210-218.

Chao B.F., Rubincam D.P., 1990. Variations of Mars gravitational field and rotation due to seasonal CO_2 exchange. Journal of Geophysical Research 95, 14,755-14,760.

Christensen E.J., Born G.H., Hildebrand C.E., Williams B.G. 1977. The mass of Phobos from Viking flybys. Geophysical Research Letters 4, 555-557.

Christensen E.J., Balmino G., 1979. Analysis of a Twelfth Degree and Order Gravity Model for Mars, Journal Geophysical Research, 84, B14, pp. 7943-7953.

Dehant V. et al., 2020. The radioscience LaRa instrument onboard ExoMars 2020 to investigate the rotation and interior of Mars. Planetary and Space Science, 180, doi:10.1016/j.pss.2019.104776.

DSN note 202: Doppler tracking, 2019. DSN No. 810-005, 202, Rev. C.

Dumoulin C., Tobie G., Verhoeven O., Rosenblatt P., Rambaux N., 2017. Tidal constraints on the interior of Venus. Journal of Geophysical Research: Planets, 122 (6), 1338-1352.

Dumoulin C., Rosenblatt P., and the RSE team, The science objectives of EnVision's radio-science experiment, EnVision conference, Paris, France, February 12-14th 2020.

Folkner, W.M., Yoder C.F., Yuan D.N., Standish E.M., Preston R.A., 1997. Interior structure and seasonal mass redistribution of Mars from radio tracking of Mars Pathfinder. Science 278 (Iss. 5344), p. 1749.

Folkner, W., 2007. Current developments in the JPL planetary ephemerides. In: First European Workshop on Solar System Dynamics and Ephemerides, ESOC, Darmstadt, Germany.

Folkner W.M., Dehant V., Le Maistre S., Yseboodt M., Rivoldini A., Van Hoolst T., Asmar S.W., Golombek M.P., 2018. The rotation and interior structure experiment on the InSight mission to Mars. Space Science Reviews, 214 (5), doi:10.1007/s11214-018-0530-5.

Forget F., Hourdin F., Fournier R., Hourdin C., Talagrand O., Collins M., Lewis S.R., Read P.L., Huot J.-P., 1999. Improved general circulation models of the Martian atmosphere from the surface to above 80 km. Journal of Geophysical Research 104 (E10), 24155-24176.

Ghail R. and the EnVision team, 2020. Envision: Understanding why our closest neighbor is so different. EnVision conference, Paris, France, February 12-14th 2020.

Genova A., Goossens S., Lemoine F.G., Mazarico E., Neumann G.A., Smith D.E., Zuber M.T., 2016. Seasonal and static gravity field of Mars from MGS, Mars Odyssey and MRO radio science. Icarus 272, 228-245.

Genova A., Goossens S., Mazarico E., Lemoine F.G., Neumann G.A., Kuang W., Sabaka T.J., Hauck S.A., Smith D.E., Solomon S.C., Zuber M.T., 2019. Geodetic evidence that Mercury has a solid inner core. Geophysical Research Letters 46 (7), 3625-3633.

Graziani A., Crewell S., Elgered G., Jarlemark P., Löhnert U., Martellucci A., Mercolino M., Rose T., Schween J., Tortora P., 2013. Media calibration system for deep space missions: Preliminary design and technical aspects. 6th ESA International workshop on tracking, telemetry and command systems for space applications, ESA-ESOC, 10-13 September 2013.

Haberle R.M., Joshi M.M., Murphy J.R., Barnes J.R., Schofield J.T., Wilson G., Lopez-Valverde M., Hollingsworth J.L., Bridger A.F.C., Schaeffer J., 1999. General circulation model simulations of the Mars pathfinder atmospheric structure investigation/meteorology data. Journal of Geophysical Research 104 (E4), 8957-8974.

Haberle R.M., Forget F., Colaprete A., Schaeffer J., Boynton W.V., Kelly N.J., Chamberlain M.A., 2008. The effect of ground ice on the Martian seasonal CO_2 cycle. Planetary and Space Science 56 (2), 251-255.

Hildebrand C., Born G. H., Duxbury T. C., 1979. In Natural and Artificial Satellite Motion, ed. P. E Nacozy & S. Ferraz-Mello (Austin, TX: Univ. Texas Press), 353.

Ho C.M., Morabito D.D., Woo R., 2008. Solar corona effects on angle of arrival fluctuations for microwave telecommunication links during superior solar conjunction. Radio Science 43: RS2003, March 2008. Doi: 10.1029/2007RS003620.

Holmes D.P., Simpson, R., Tyler G.L., Pätzold M., Dehant V., Rosenblatt P., Häusler B., Goltz G., Kahan D., Valencia J., Thompson T, 2008. The challenges and opportunities for international cooperative radio science; Experience with the Mars Express and Venus Express Missions. Proc. AIAA/AAS Astrodynamics Specialist Conference 18, 2008-6395, 2008.

Iess L., Di Benedetto M., James N., Mercolino M., Simone L., Tortora P., 2014. Astra: Interdisciplinary study on enhancement of the end-to-end accuracy for spacecraft tracking techniques. Acta Astronautica 94, 699-707.

Jacobson R.A., 2010. The orbits and masses of the Martian satellites and the libration of Phobos. The Astronomical Journal 139 (2), 668-679.

Justh H., Justus C., Ramey H., 2011. Mars-GRAM 2010: improving the precision of Mars-GRAM. Mars Atmos.: Model. Observ. 1, 265–267.

Kaula W.M. 1966. Theory of satellite geodesy. Blaisdell, Waltham, M.A.

Kolyuka Y.F., Efimov A.E., Kudryavtsev S.M., Margorin O.K., Tarasov V.P., Tikonov V.F. 1990. Refinement of the gravitational constant of Phobos from Phobos 2 tracking data, Soviet Astronomical Letters 16(March-April), 168-170.

Konopliv A.S., Yoder C.F., 1996. Venusian k_2 tidal Love number from Magellan and PVO tracking data. Geophysical Research Letters 23 (14), 1857-1860.

Konopliv A.S., Banerdt W.B., Sjogren W.L., 1999. Venus gravity: 180th degree and order model. Icarus 139 (1), 3-18.

Konopliv A.S., Miller J.K., Owen W.M., Yeomans D.K., Giorgini J.D., Garmier R., Barriot J.-P., 2002. A global solution for the gravity field, rotation, landmarks, and ephemeris of Eros. Icarus 160 (2), 289-299.

Konopliv A.S., Yoder C.F., Standish E.M., Yuan D.-N., Sjogren W.L., 2006. A global solution for the Mars static and seasonal gravity, Mars orientation, phobos and deimos masses, and Mars ephemeris. Icarus 182, 23–50.

Konopliv A.S., Asmar S.W., Folkner W.M., et al., 2011. Mars high resolution gravity fields from MRO, Mars seasonal gravity, and other dynamical parameters. Icarus 211, 401–428.

Konopliv A.S., Park R.S., Folkner W.M., 2016. An improved JPL Mars gravity field and orientation from Mars orbiter and lander tracking data. Icarus 274, 253-260.

Konopliv A.S., Park R.S., Ermakov A.I., 2020. The Mercury gravity field, orientation, Love number, and ephemeris from the MESSENGER radiometric tracking data. Icarus 335, article id. 113386.

Kuchynka P., Folkner W.M., Konopliv A.S., Parker T.J., Park R.S., Le Maistre S., Dehant V., 2014. New constraints on Mars rotation determined from radiometric tracking of the Opportunity Mars Exploration rover. Icarus 229, 340-347.

Kudryashova M., Rosenblatt P., Marty J.C., 2015. Phobos mass estimations from MEX and Viking-1 data: Influence of different noise sources and estimation strategies. Proceedings of the Journées 2014 "Systèmes de référence spatio-temporels": Recent developments and prospects in ground-based and space astrometry, held at Pulkovo Observatory on 22nd-24th September 2014. Eds. Malkin Z. and Capitaine N., ISBN 978-5-9651-0873-2 & ISBN 978-2-901057-70-3, pp. 100-103.

Lainey V., Dehant V., Pätzold M., 2007. First numerical ephemerides of the Martian moons. Astronomy and Astrophysics 465 (3), 1075-1084.

Lee D., 2002. Measurement error for two-way coherent Doppler for MRO, interoffice memorandum, 15 pp. Jet Propul. Lab., Pasadena, Calif.

Lemoine F.G., Smith D.E., Rowlands D.D., Zuber M.T., Neumann G.A., Chinn D.S., Pavlis D.E., 2001. An improved solution of the gravity field of Mars (GMM-2B) from Mars Global Surveyor. J. Geophys. Res. 106 (E10), 23359–23376.

Le Maistre S., Rosenblatt P., Rivoldini A., Dehant V., Marty J.C., Karatekin Ö., 2012. Lander radio science experiment with a direct link between Mars and the Earth. Planetary and Space Science, 68 (1), 105-122.

Le Maistre S., Rosenblatt P., Rambaux N., Castillo-Rogez J.C., Dehant V., Marty J.C., 2013. Phobos interior from librations determination using Doppler and star tracker measurements. Planetary and Space Science 85, 106-122.

Le Maistre S., 2013. The rotation of Mars and Phobos from Earth-based radio-tracking observations of a lander. PhD thesis of Université Catholique de Louvain.

Le Maistre S., Rivoldini A., Rosenblatt P., 2019. Signature of Phobos' interior structure in its gravity field and libration. Icarus, 321, 272-290.

Lemoine F.G., Bruinsma S., Chinn D.S., Forbes J.M., 2006. Thermospheric studies with Mars Global Surveyor. Paper Presented at AIAA/AAS Astrodynamics Specialist Conference. American Institute of Aeronautics and Astronautics, Keystone, Colorado.

Lemoine F.G., Luthcke S.B., Rowlands D.D., Chinn D.S., Klosko S.M., Cox C.M., 2007. The use of mascons to resolve time-variable gravity from GRACE. In: Tregoning P., Rizos C. (eds) Dynamic planet. International Association of Geodesy Symposia, vol. 130. Springer, Berlin, Heidelberg.

Liou Y.A., Pavelyev A.G.., Matyugov S.S., Yakovlev O.I., Wickert J., 2010. Radio occultation method for remote sensing of the atmosphere and ionosphere. Eds. Y.A. Liou, published by Intech.

Lorell J., Born G.H., Christensen E.J., Esposito P.B., Frank J.J., Laing P.A., Sjogren W.L., Wong S.K., Reasenberg R.D., Shapiro I.I., Slater G.L., 1973. Gravity Field of Mars from Mariner-9 tracking data (A. 6.2 and A. 6. 1). Icarus l8 (2), 304-316.

Love A.E.H., 1909. The yielding of the Earth to disturbing forces. Proceedings of the Royal Society of London. Series A, Containing Papers of a Mathematical and Physical character, 82 (551), 73-88.

Marty J.C., Balmino G., Duron J., Rosenblatt P., Le Maistre S., Rivoldini A.S., Dehant V., Van Hoolst T., 2009. Martian gravity field model and its time variations from MGS and Odyssey data. Planetary and Space Science 57, 350-363.

Marty J.C., Bruinsma S., Zittersteijn M., Le Maistre S., Rosenblatt P., 2013. Time variations of Mars' gravitational field using MGS, Mars Odyssey and MRO radio science data. AGU fall meeting, San-Francisco, CA, USA, December 9-13th, 2013.

Michel P., Cheng A., Küppers M., Pravec P., Blum J., Delbo M., Green S.F., Rosenblatt P., Tsiganis K., Vincent J.B., Biele J., Ciarletti V., Hérique A., Ulamec S., Carnelli I., Galvez A., Benner L., Naidu S.P., Barnouin O.S., Richardson D.C., Rivkin A., Scheirich P., Moskovitz N., Thirouin A., Schwartz S.R., Campo Bagatin A., Yu Y., Science case for the Asteroid Impact Mission (AIM): A component of the Asteroid Impact & Deflection Assessment (AIDA) mission. Advances in Space Research, 57 (12), 2529-2547.

Moyer T.D., 1971. Mathematical formulation of the double-precision orbit determination program (DPODP). JPL Technical Report 32-1527. Jet Propulsion Laboratory, California Institute of Technology, Pasadena, CA.

Moyer T.D., 2000. Formulation for observed and computed values of Deep Space Network data types for navigation, Monograph 2, Deep Space Communications and Navigation Series.

Müller-Wodarg, I.C.F., Bruinsma S., Marty J.C., Svedhem H., 2016. *In situ* observations of waves in Venus's polar lower thermosphere with Venus Express aerobraking. Nature Physics, 12 (8), 767-771.

Murchie S.D., and 13 colleagues, 1991. Color heterogeneity of the surface of Phobos: Relationships of geological features and comparison to meteorite analogs. Journal of Geophysical Research 96, 5925-5945.

Notaro V., Iess L., Armstrong J.W., Asmar S.W., 2020. Reducing Doppler noise with multi-station tracking: The Cassini test case. Acta Astronautica 173, 45-52.

Oberst J., Zubarev A., Nadezhdina I., Shishkina L., Rambaux N., 2014. The Phobos geodetic control point network and rotation model. Planetary and Space Science 102, 45-50.

Parisi M., Folkner W.M., Galanti E., Kaspi Y., Buccino D.R., Oudrhiri K., Bolton S.J., 2020. A mascon approach to estimating the depth of Jupiter's great red spot with Juno gravity measurements. Planetary and Space Science 181 (104781), doi:10.1016/j.pss.2019.104781.

Pätzold M., Wennmacher A., Häusler B., Eidel W., Morley T., Thomas N., Anderson J.D., 2001. Mass and density determinations of 140 Siwa and 4979 Otawara as expected from the Rosetta flybys. Astronomy and Astrophysics 370, 1122-1127.

Pätzold M., Andert T.P., Jacobson R., Rosenblatt P., Dehant V., 2014. Phobos: Observed bulk properties. Planetary and Space Science 102, 86-94.

Pätzold M., Andert T., Hahn M., Asmar S.W., Barriot J.-P., Bird M.K., Häusler B., Peter K., Tellmann S., Grün E., Weissman P.R., Sierks H., Jorda L., Gaskell R., Preusker F., Scholten F., 2016. A homogeneous nucleus for comet 67P/Churyumov-Gerasimenko from its gravity field. Nature 530 (7588), 63-65.

Pavlis D.E., Wimert J., McCarthy J.J., 2013. GEODYN II System Description, vols. 1–5 SGT Inc., Greenbelt, MD.

Pignatale F.C., Charnoz S., Rosenblatt P., Hyodo R., Nakamura T., Hidenori G., 2018. On the impact origin of Phobos and Deimos III: Resulting composition from different impactors. The Astrophysical Journal, doi.org/10.3847/1538-4357/aaa23e, 853:118, 12pp.

Reigber C., Mueller H., Bosch W., Balmino G., Moynot B., 1985. GRIM gravity model improvement using LAGEOS (GRIM3-L1). Journal of Geophysical Research 90 (B11), 9285-9300.

Rambaux N., Castillo-Rogez J.C., Le Maistre S., Rosenblatt P., 2012. Rotational motion of Phobos. Astronomy and Astrophysics, Vol. 548, id.A14, 11pp., doi:10.1051/0004-6361/201219710.

Rivoldini A., Van Hoolst T., Verhoeven O., Mocquet A., Dehant V., 2011. Geodesy constraints on the interior structure and composition of Mars. Icarus 213 (2), 451-472.

Rosenblatt P., Lainey V., Le Maistre S., Marty J.C., Dehant V., Pätzold M., van Hoolst T., Häusler B., 2008. Accurate Mars Express orbits to improve the determination of the mass and ephemeris of the Martian moons. Planetary and Space Science, 56, pp. 1043-1053.

Rosenblatt P., Rivoldini A., Dehant V., 2009. The interior structure of Phobos, 50th Vernadsky-Brown Symposium, Moscow, Russia, October 12-15, 2009.

Rosenblatt P., Rivoldini A., Dehant V., 2010. Inhomogeneous mass distribution inside Phobos, EPSC meeting, Rome, Italy, September 19-24, 2010

Rosenblatt P., 2011. The origin of the Martian moons revisited. Astronomy and Astrophysics Review, 19, (1), 19-44.

Rosenblatt P., Charnoz S., 2012. On the formation of the Martian moons from a circum-martian accretion disk. Icarus 221, (2), 806-815.

Rosenblatt P., Bruinsma S.L., Müller-Wodarg I.C.F., Häusler B., Svedhem H., Marty J.C., 2012. First ever in situ observations of Venus' polar upper atmosphere density using the tracking data of the Venus Express Atmospheric Drag Experiment (VExADE). Icarus, Special issue: "Advances in Venus science" 217, (2), 831-838.

Rosenblatt P., Dumoulin C., Tellmann S., Kaspi Y., Fienga A., Marty J.C., Withers P., Ghail R., Wilson C., Widemann T., 2019a. EnVision radio science experiment, EPSC-DPS2019-1475-1, Geneva, Switzerland, September 15-20th 2019.

Rosenblatt P., Dumoulin C., Marty J.C., Fienga A., 2019b. Geodesy and ephemeris experience with EnVision, International Venus Conference, Niseko, Hokkaido, Japan, May 31st – June 3rd 2019.

Rosenblatt P., Dumoulin C., Marty J.C., Genova A., 2020a, Assessment of the EnVision gravity experiment, EnVision conference, Paris, France, February 12-14th 2020.

Scanlon B. R., Zhang Z., Save H., Wiese D.N., Landerer F.W., Long D., Longuevergne L., Chen J., 2016. Global evaluation of new GRACE mascon products for hydrologic applications, Water Resour. Res., 52, doi:10.1002/2016WR019494.

Schrama E.J.O., Wouters B., Rietbroek R., 2014. A mascon approach to assess ice sheet and glacier mass balances and their uncertainties from GRACE data. Journal of Geophysical Research 119 (7), 6048-6066.

Serra D., Giacomo L., Giacomo T., Durante D., Gomez Casajus L., Notaro V., Zannoni M., Iess L., Tortora P., Bolton S.J., 2019. A solution of Jupiter's gravitational field from JUNO data with the ORBIT14 software. Monthly Notices of the Royal Astronomical Society 490 (1), 766-772.

Smith D.E., Lerch F.J., Chan J.C., Chinn D.S., Iz H.B., Mallama A., Patel G.B., 1990. Mars gravity field error analysis from simulated radio tracking of Mars Observer. Journal of Geophysical Research 95, 14155-14167.

Smith D.E., Lemoine F.G., Zuber M.T., 1995. Simultaneous estimation of the masses of Mars, Phobos, and Deimos using spacecraft distant encounters. Geophysical Research Letters 22, 2171-2174.

Smith D.E., Zuber M.T., Haberle R.M., Rowlands D.D., Murphy J.R. 1999. The Mars seasonal CO_2 cycle and the time variation of the gravity field: A general circulation model simulation. Journal of Geophysisal Research 104,1885-1896.

Smith D.E., Zuber M.T., Torrence M.H., Dunn P.J., Neumann G.A., Lemoine F.G., Fricke S.K., 2009. Time variations of Mars' gravitational field and seasonal changes in the masses of the polar ice caps. Journal of Geophysical Research, 114 (E5), doi: 10.1029/2008JE003267.

Smith D.E., Zuber M.T., Phillips R.J., Solomon S.C., Hauck S.A., Lemoine F.G., Mazarico E., Neumann G.A., Peale S.J., Margot J.-L., Johnson C.L., Torrence M.H., Perry M.E., Rowlands D.D., Goossens S., Head J.W., Taylor A.H., 2012. Gravity field and internal structure of Mercury from MESSENGER. Science 336 (6078), 214-(2012).

Standish E.M. 2006. JPL Planetary Ephemeris DE414. JPL Technical Report IOM 343R-06-002.

Thomas P.C., 1993. Gravity, tides, and topography of small satellites and asteroids: Application to surface features of the Martian satellites. Icarus 105, 326-344.

Tolson R.H., Blackshear W.T., Mason M.L. 1977. The mass of Phobos, Geophysical Research Letters 4, 551-554.

Usui T., Bajo K.-I., Fujiya W., Furukawa Y., Koike M., Miura Y.N., Sugahara H., Tachibana S., Takano Y., Kuramoto K., 2020. The importance of Phobos sample return for understanding the Mars-moon system. Space Science Reviews 216 (4), doi:10.1007/s11214-020-00668-9.

Verhoeven O., Rivoldini A., Vacher P., Mocquet A., Choblet G., Menvielle M., Dehant V., Van Hoolst T., Sleewaegen J., Barriot J.-P., Lognonné P., 2005. Interior structure of terrestrial planets: Modeling Mars' mantle and its electromagnetic, geodetic, and seismic properties. Journal of Geophysical Research 110 (E4), doi:10.1029/2004JE002271.

Walsh K.J., Richardson D.C., Patrick M., 2008. Rotational breakup as the origin of small binary asteroids. Nature 454 (7201), 188-191.

Wieczorek M.A., 2007. Gravity and topography of the terrestrial planets. In Treatise on Geophysics, Volume 10, 165-206, doi:10.1016/B978-044452748-6/00156-5.

Williams B.G., Duxbury T.C., Hildebrand C.E. 1988. Improved determination of Phobos and Deimos masses from Viking flybys, Lunar Planetary Science Conference XIX, 1274-1275(abstract).

Willner K., Shi X., Oberst J., 2014. Phobos' shape and topography models. Planetary and Space Science 102, 51-59.

Witasse O., Duxbury T., Chicarro A., Altobelli N., Andert T., Aronica A., Barabash S., Bertaux J.-L., Bibring J.-P., Cardesin-Moinelo A., Cichetti A., Companys V., Dehant V., Denis M., Formasino V., Futaana Y., Giuranna M., Gondet B., Heather D., Hoffmann H., Holmström M., Manaud N., Martin P., Matz K.-D., Montmessin F., Morley T., Müller M., Neukum G., Oberst J., Orosei R., Pätzold M., Picardi G., Pischel R., Plaut J.-J., Reberac A., Pardo Voss P., Roatsch T., Rosenblatt P., Remus S., Schmedemann N., Willner K., Zegers T., 2014. Mars Express investigations of Phobos and Deimos. Planetary and Space Science, 102, 18-34.

Yang X., Yan J.G., Andert T., Ye M., Pätzold M., Hahn M., Jin W.T., Li F., Barriot J.-P., 2019. The second-degree gravity coefficients of Phobos from two Mars Express flybys. Monthly Notices of the Royal Astronomical Society, 490 (2), 2007-2012.

Yoder C.F., Konopliv A.S., Yuan D.N., Standish E.M., Folkner W.M., 2003. Fluid core size of Mars from detection of the solar tide. Science 300, 299–303.

Yuan D.N., Sjogren W.L., Konopliv A.S., Kucinskas A.B. 2001. Gravity field of Mars: A 75th degree and order model. Journal of Geophysical Research 106, 23377-23402.

Zannoni M., Tommei G., Modenini D., Tortora P., Mackenzie R., Scoubeau M., Herfort U., Carnelli I., 2018. Radio science investigations with the asteroid impact mission. Advances in Space Research 62 (8), 2273-2289.

Zuber M.T., Lemoine F.G., Smith D.E., Konopliv A.S., Smrekar S.E., Asmar S.W., 2007. Mars Reconnaissance Orbiter radio-science gravity investigation. Journal of Geophysical Research 112 (E05S07), doi:10.1029/2006JE002833.

2 The formation of the Martian moons

Almost all the planets of our solar system have moons. Each planet-moon system however has a unique set of characteristics. The Martian system does not have one single big moon, like the Earth, nor several tens of moons of various sizes, observed around the giant planets, but two small moons: Phobos and Deimos. How did such a system form? This question is still being investigated using Earth-based and space-borne observations of the Martian moons and on the basis of more modern theories of moon formation elsewhere in the solar system.

The following sections are largely based on the publication [PR46], which compiles my achievements in the modeling of the formation of the Martian moons (publications [PR18], [PR24], [PR36], [PR37], [PR41], [PR43], see Section 4).

2.1 Introduction

The origin of the natural satellites or moons of the solar system is as challenging to unravel as the formation of the planets. Before the start of the space probe exploration era, this topic of planetary science was restricted to telescopic observations, which limited the possibility of testing different formation scenarios. This era has considerably boosted this topic of research, particularly after the Apollo missions returned samples from the Moon's surface to Earth. Observations from subsequent deep space missions such as Viking Orbiter 1 & 2, Voyager 1 & 2, Phobos-2, Galileo, Cassini-Huygens, and the most recent Mars orbiters such as Mars Express as well as from the Hubble space telescope have served to intensify research in this area.

Each moon system has its own specificities, with different origins and histories. It is widely accepted that the Earth's Moon formed after a giant collision between the proto-Earth and a body similar in size to Mars. The Galilean moons of Jupiter, on the other hand, appear to have formed by accretion in a circum-Jovian disk, while smaller, irregularly-shaped satellites were probably captured by the giant planet. The small and medium-sized Saturnian moons may have formed from the rings encircling the planet. Among the terrestrial planets, Mercury and Venus have no moons, the Earth has a single large moon and Mars has two very small satellites. This raises some challenging questions: what processes can lead to moon formation around terrestrial planets, and what parameters determine the possible outcomes, such as the number and size of moons? The answer to such fundamental questions necessarily entails a thorough understanding of the formation of the Martian system, and may have relevance to the possible existence of (exo)moons orbiting exoplanets. The formation of such exomoons is of great importance as they could influence conditions for habitability, or for maintaining life over long periods of time at the surface of Earth-like exoplanets, for example by limiting the variations of the orientation of the planet's rotation axis and thus preventing frequent changes of its climate.

This article summarizes our current knowledge concerning the origin of Phobos and Deimos, acquired from observational data as well as theoretical work. It describes why early observations led to the idea that the two satellites were captured asteroids and why the difficulties in reconciling the current orbits of Phobos and Deimos with those of captured bodies calls for an alternative theory. A detailed description of a giant-impact

scenario is then given, in which moons similar to Phobos and Deimos can be formed in orbits similar to those observed today. This scenario also restricts the range of possible composition of the two moons, providing a motivation for future missions that aim for the first time to bring material from the Martian system back to Earth.

2.2 Puzzling origin: Capture vs in-situ formation

2.2.1 The Martian moon system

The two natural satellites of Mars, Phobos and Deimos, were discovered in August 1877 by the American astronomer Asaph Hall[49] (Hall, 1878). They probably went unnoticed for a long time because of their low albedo and their proximity to Mars which makes them difficult to observe with Earth-based telescopes (Pascu et al., 2014). Subsequent telescopic observations determined that their orbits are near-equatorial and near-circular, with Phobos orbiting below the synchronous limit and Deimos orbiting above it (see Table 1). Furthermore, the secular acceleration of Phobos' longitude along its orbit, discovered by Sharpless (1945), indicates that its orbit is slowly decaying, with Phobos losing orbital energy and gradually approaching Mars due to tidal dissipation inside the planet (e.g. Burns, 1992). In contrast, Deimos lies above the synchronous limit and thus is receding from the planet, just as the Moon is receding from Earth. Deimos' secular acceleration has not yet been observed due to its low mass and greater distance from Mars (see Tables 1 & 2). On the basis of the brightness of the two moons, their sizes were first estimated to be a few tens of kilometers (e.g. Pascu et al., 2014). Phobos and Deimos are thus much smaller than the Earth's Moon, the Galilean satellites of Jupiter and the main moons of the other giant planets. Earth-based historical observations have thus highlighted the main challenge raised by the Martian system: how to explain the formation of two small moons in near-equatorial and near-circular orbits around their primary planet?

Moons	Phobos	Deimos
Semi-major axis	9375 km (2.76 R_M)	23458 km (7 R_M)
Eccentricity	0.01511	0.00027
Inclination to the equator	1.076°	1.789°
Orbital period	7h 39' 19.47"	30h 18' 1.36"
Secular acceleration along the orbit	1.273 +/- 0.003 mdeg/year^2	-

Table 1: Orbital architecture of the Martian system (Jacobson & Lainey, 2014). The synchronous limit is at 20400 km or around 6 RM, where 1 RM is Mars' mean radius, equal to 3400 km. This limit is the orbital position where the revolution period around Mars is equal to the spin of the planet (24h39').

[49] Asaph Hall was greatly supported by his wife Angeline Stickney in his quest of Martian satellites.

Moons	Phobos	Deimos
Radius (in km)	13.03 x 11.40 x 9.14 (1)	7.5 x 6.1 x 5.2 (2)
Mass (in 10^{16} kg)	1.066 +/- 0.013 (3)	0.151 +/- 0.003 (4)
Volume (in km^3)	5742 +/- 35 (1)	1017 +/- 130 (2)
Density (in g/cm^3)	1.856 +/- 0.034 (5)	1.48 +/- 0.22 (6)

Table 2: Bulk properties of the Martian moons. (1) Willner et al., 2014; (2) Thomas, 1993; (3) Paetzold et al. (2014); (4) Jacobson (2010); (5) using mass from (4) and volume from (1); (6) Rosenblatt, 2011. The radii are from the best fit ellipsoid to the shape of the body (1).

2.2.2 Are Phobos and Deimos small asteroids?

The investigation of the Martian moon system entered a new era with space probe explorations (Duxbury et al., 2014). The first missions to have made important observations of the two moons were Mariner 9, the Viking 1 and 2 orbiters and Phobos-2. These provided the first resolved images and spectroscopic observations of the surface of Phobos and Deimos (more recent images are shown in figures 1 & 2 and more up-to-date spectra in figure 3), as well as the first determination of their density (mass and volume, see updated values in Table 2). The data suggested that the two small moons resemble asteroids with irregular shape, cratered surface, low albedo (Figures 1 & 2) and low density (Table 2). Furthermore, the reflectance spectra of their surfaces in the near-infrared and visible wavelengths, around 0.4 to 4 microns, show an increasing slope toward infra-red wavelengths (reddening slope, figure 3) that match those of several primitive low-albedo asteroids (Pang et al., 1978; Pollack et al., 1978; Murchie et al., 1991; Murchie & Erard, 1996). Phobos' surface shows areas with different spectral slopes defining the so-called red and blue units while Deimos' surface shows only spectra similar to the Phobos red unit (Figure 2 & 3). The reflectance spectra of Phobos have been confirmed by the recent Mars Reconnaissance Orbiter (Fraeman et al., 2012), Mars Express (Fraeman et al., 2012; Witasse et al., 2014) and Rosetta (Pajola et al., 2012) missions as well as by observations obtained with the Hubble space telescope (Rivkin et al., 2002) and with the ground-based Mayall 4-m telescope of the Kitt Peak National Observatory (Fraeman et al., 2014). In addition, Mars Express has confirmed the low density of Phobos by improving estimates of its mass (Paetzold et al., 2014) and volume (Willner et al., 2014). The morphological, physical and spectroscopic similarities between the Martian moons and the primitive asteroids are the main arguments favouring the capture scenario, in which Phobos and Deimos are small low-albedo asteroids captured by the planet (e.g. Pang et al., 1978; Burns, 1992; Pajola et al., 2012; 2013). These asteroids would have formed from the condensation of carbonaceous material in the solar nebula beyond Mars' orbit.

No satisfactory spectral match between Phobos and Deimos and meteoritic material, recognized as the material of primitive asteroids, has however been found so far (e.g. Murchie et al., 1991; Murchie & Erard, 1996, Vernazza et al., 2010). In addition, the reflectance spectra do not clearly display absorption bands (Figure 3) which provide diagnostics for the composition, in terms of carbonaceous, silicate or hydrated material. Space weathering (alteration in space environment over time) on airless bodies may nonetheless suppress any of such possible bands. It is known that this process is responsible for darkening, reddening and suppression of absorption bands (as observed for Phobos and Deimos spectra, figure 3) in reflectance spectra of silicate material, for example on the Moon (Clark et al., 2002; Pieters et al., 2014). It

may therefore not be possible to determine the true surface composition of the two moons through spectroscopic observations alone (Rosenblatt 2011). Murchie & Erard (1996) indeed did not rule out that Phobos' spectra could be those of very highly weathered silicate material. It has been proposed more recently that dark silicate (anorthosite) terrains on the Moon can have low albedo similar to those of Phobos and Deimos (Yamamoto et al., 2018). On the other hand, a silicate-rich Phobos would not preclude the possibility of capture, since silicate asteroids can condense from material in the solar nebula closer to Mars' orbit than the region in which carbonaceous asteroids form.

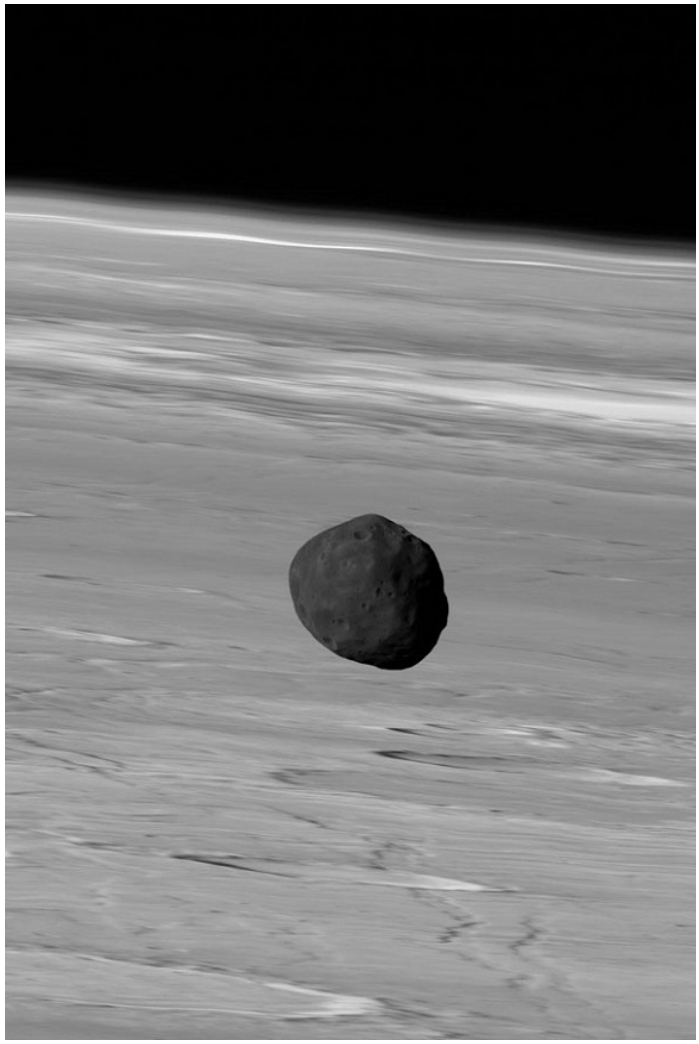

Figure 1: Phobos above Mars as seen by Mars Express, showing the darkness (low albedo) of the moon compared to the brightness of the planet (credit DLR/FU Berlin/ESA).

A tentative, very weak absorption band at around 0.65 microns in the spectra of Phobos has recently been detected (Pajola et al., 2013; Fraeman, et al. 2014; see also figure 3) and could be interpreted as the signature of a carbonaceous composition, although space weathering effects cannot be ruled out (Fraeman et al., 2014). Such effects on carbonaceous material are less well understood than on silicate material, and may give rise to red and even blue spectral slopes observed in reflectance spectra of carbonaceous asteroids (Lantz et al., 2013). The effect of space weathering on reflectance spectra was tentatively simulated for carbonaceous meteorite samples, but the result shared little

similarity with Phobos and Deimos (Moroz et al., 2004; Vernazza et al., 2010). Emissivity spectra in the thermal infra-red domain (wavelengths from 5 to 50 microns) of the surface of Phobos were also measured for the first time by Mars Odyssey (Roush and Hogan, 2000) and Mars Express (Giuranna et al., 2011; Witasse et al., 2014). In contrast to the reflectance spectra, these emissivity spectra show clear features more typical of silicate rather than carbonaceous meteorite material (Figure 3, Giuranna et al., 2011). They have however a coarser spatial resolution than the reflectance spectra and are also more affected by grain-size particles of the surface regolith, and to some extent by space weathering (Pieters, 2014).

Figure 2: Recent images of the Martian moons from the High Resolution Imaging Science Experiment (HiRISE) onboard the Mars Reconnaissance Orbiter. The individual colour images in near infra-red and blue-green channels have been combined to produce a false-colour representation where patches of high infrared reflectance appear in red while blue-green reflectance patches appear in blue (Thomas et al., 2011). Colour heterogeneities on the surface of the two moons may reveal variations of composition and/or of space weathering effects (Pieters, 2014). The 9 km impact crater Stickney on Phobos appears on the right-hand side of the image (Credit NASA/JPL/University of Arizona).

The ambiguity in the composition of the Martian moons derived from remote sensing spectral observations raises an intriguing question: are Phobos and Deimos made of asteroid material (either silicate, carbonaceous or something else) or do they incorporate some Martian material? The latter would suggest that Phobos and Deimos could have been formed in situ around Mars, thus weakening the asteroid capture scenario. In addition, the current near-equatorial and near-circular orbits of the two moons are unlikely to result from a capture (Burns, 1992; Rosenblatt, 2011).

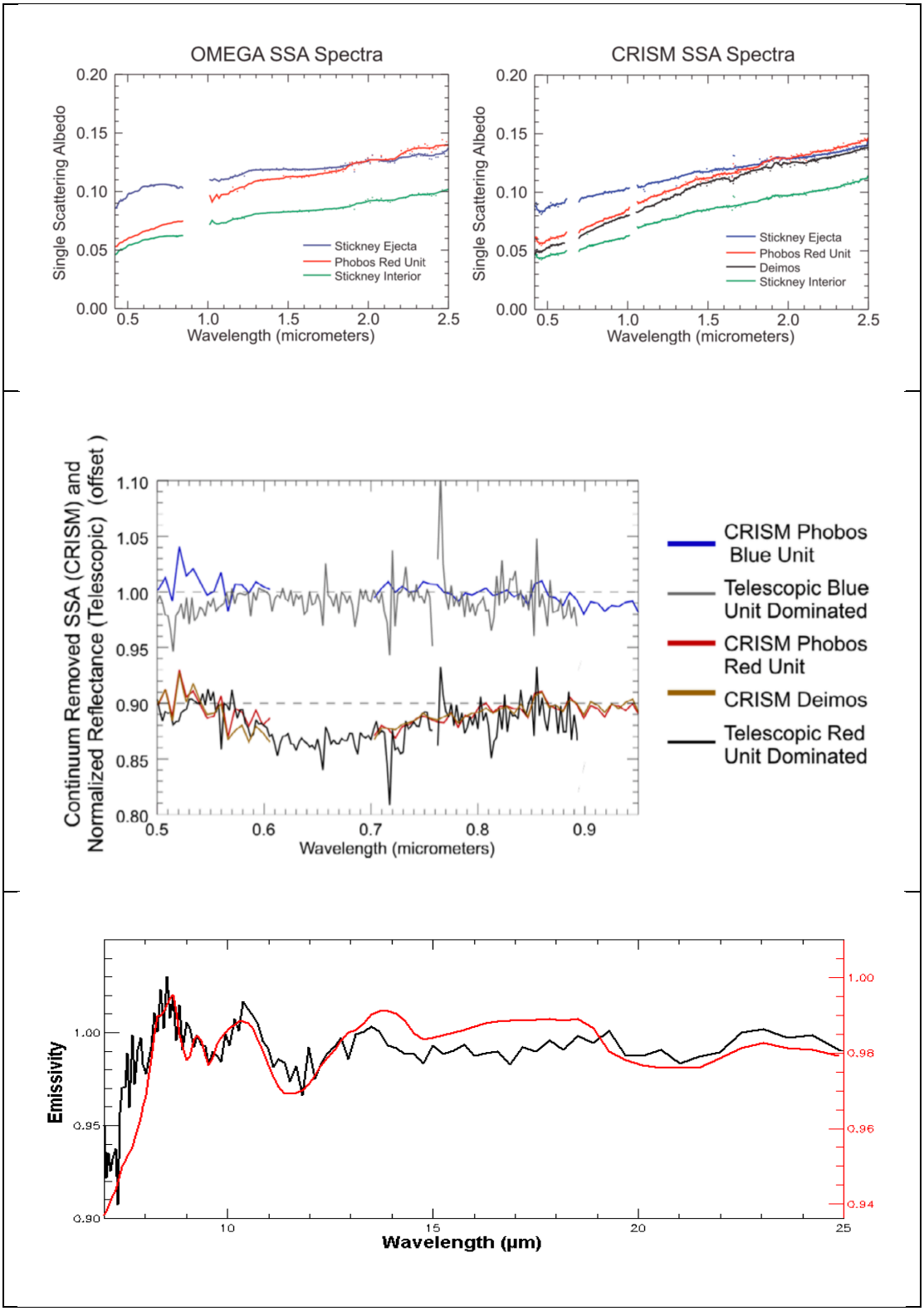

Figure 3: (Top) Most recent Reflectance (Solar Radiation Reflectance) spectra of Phobos and Deimos obtained by the Mars Express' OMEGA and the Mars Reconnaissance Orbiter's CRISM instruments. The Reflectance (Single Scattering Albedo) Spectra of the Stickney Crater area (Blue Unit) is flatter than that of Phobos Red Unit and of Deimos. Adapted from Fraeman et al., 2012. (Medium) CRISM and telescopic observations showing the tentative tiny absorption band at around 0.65 microns for Deimos and for the Red Unit of Phobos, which could be interpreted as the signature of carbonaceous material. Adapted from Fraeman et al. (2014). (Bottom) Emissivity (Thermal Radiation Emission) spectra of Phobos surface (black curve) compared to spectra of silicate material (red curve). Adapted from Giuranna et al. (2011).

2.2.3 Is capture dynamically possible?

While specific dynamical conditions are required for capture to occur (Pajola et al., 2012), it is not impossible to trap asteroids in a closed orbit around Mars. It can even be facilitated by a three-body capture mechanism, particularly in the early solar system when there was an abundance of planetesimals and other small debris (Hansen, 2018). The orbit of such a captured body is however expected to be significantly elliptical and non-equatorial, as is the case for example for the irregular satellites of Jupiter, in contrast to the actual orbits of Phobos and Deimos (see Table 1). The capture scenario thus requires a mechanism to change the post-capture orbit into the current near-equatorial and near-circular orbits observed today.

One possible mechanism is orbital tidal dissipation (Kaula, 1964). The tides raised by the captured satellite inside Mars and the tides raised by Mars inside the satellite contribute to the dissipation of the satellite orbital energy, and hence modify its orbit. Studies have shown however that this mechanism is not sufficient to change an elliptical and non-equatorial orbit into the almost circular and equatorial orbit of Deimos within the 5 billion years lifetime of the solar system (Szeto, 1983). Since Phobos is larger than Deimos (see Table 2), tidal dissipation has more effect on its orbit: a very elliptical post-capture orbit can be circularized over 5 billion years (e.g. Lambeck, 1979; Cazeneuve et al., 1980; Burns, 1992), assuming a bulk rigidity of rocky material with some degree of micro-porosity (for example, a carbonaceous chondrite material; Lambeck 1979) and a low tidal dissipation factor (Rosenblatt, 2011). Changing the inclination from the ecliptic plane (i.e. the mean orbital plane of the asteroids) to the equatorial plane however requires an even more dissipative material (Mignard, 1981), closer to icy rather than rocky material (Rosenblatt, 2011; Rosenblatt and Pinier, 2014).

A number of possible solutions to this problem have been proposed. One suggestion is that the small body was captured in an equatorial orbit; this however requires that the orbital distance to Mars decreases rapidly below roughly 13 R_M after capture in order to maintain the orbit in the equatorial plane, which seems difficult given how slowly the orbital eccentricity is modified by tidal effects (Burns, 1992). Others authors have proposed that the post-capture orbit was rapidly inclined into the equatorial plane and significantly circularized by drag dissipation in a primitive planetary nebula (Sasaki, 1989). Such a nebula would have been formed around a planet accreting from the solar nebula gas. Drag effect studies (Sasaki, 1989) however have so far been unable to show whether the density profile and survival time of this nebula are consistent with the requirements of the capture scenario.

2.2.4 Alternative scenarios: in-situ formation

The difficulty of reconciling the outcome of a capture scenario with the current orbital properties of the Martian moons has motivated the search for alternatives. Most of these assume that the moons have accreted in an equatorial disk of debris containing extra-Martian material in order to explain their possible primitive composition (Rosenblatt, 2011).

This idea of a gravitational aggregate of debris as the bulk structure of the Martian moons is based on their low bulk density (see Table 2), suggesting a large amount of porosity in their interior (Murchie et al., 1991; Andert et al., 2010; Rosenblatt, 2011), as well as on plausible explanations for Phobos' main geomorphological surface features such as the large impact crater Stickney (Bruck Syal et al., 2016) and some of its grooves (Hurford et al., 2016). These surface features would indeed require low rigidity that can be accounted for by porosity (Jaeger et al., 2007; Le Maistre et al., 2013).

Different mechanisms for the formation of the disk have been proposed. One idea is that a body much more massive than Phobos and Deimos might first have been captured by Mars. Its orbit would have rapidly decayed due to tidal forces and the body would have been destroyed when crossing the Roche limit (Singer, 2003). The resulting debris would have formed a ring around Mars below the Roche limit (as modelled later by Black & Mittal, 2015), from which small moons would have emerged. This relatively simple scenario however leads to another impasse: Mars' Roche limit is about three R_M, well inside the synchronous limit which is about six R_M (Table 1). It is difficult to find a mechanism by which the moons formed at the Roche limit could have migrated far from Mars and then stayed in orbit for a long time, in particular for Deimos which orbits at a distance of nearly seven R_M (see table 1, Rosenblatt & Charnoz, 2012, see also Section 2.3.4).

Another possibility is that the disk resulted from a giant impact, similar to that which led to the formation of the Earth's Moon. This was first proposed by Craddock (1994) but was disregarded by the scientific community until new data about Phobos' interior by Mars Express implying a significant amount of porosity and favoring a formation in an accretion disk (e.g. Andert et al., 2010; Rosenblatt, 2011) revived this scenario. A reapprasial of Phobos' origin from the data of the OMEGA spectrometer onboard Mars Express also favored such a scenario (Bibring, 2010). Craddock's (2011) study suggests that a large body (one quarter to one third the size of Mars) collided with the proto-Mars at least 4 billion years ago, blasting debris into space. Phobos and Deimos may be the last surviving moons that emerged from the resulting accretion disk (Figure 4). The problem still remains, however, of reconciling the migration of moons formed at the Roche limit with the current orbits of Phobos and particularly of Deimos today (Rosenblatt & Charnoz, 2012).

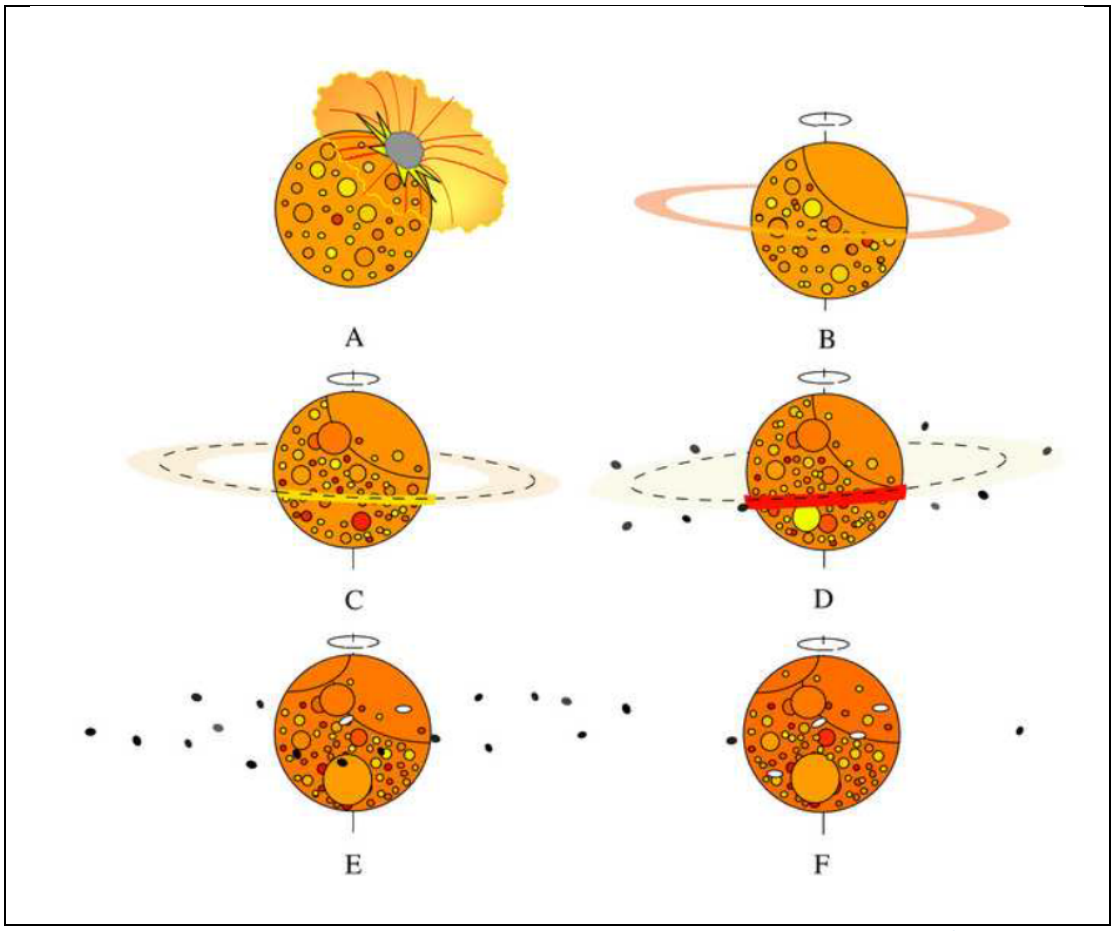

Figure 4: Sketch of the giant impact scenario leading to the formation of Phobos and Deimos (from Craddock, 2011).

2.3 A giant collision scenario

The giant impact scenario leading to the formation of moons can be divided into a number of stages (Figure 4), each of which must be carefully examined in order to build a robust model of the formation process, capable of reproducing the observed orbits and of providing information on the composition of the resulting moons.

2.3.1 A giant impact early in Mars history

The first question to be answered is whether or not there is any evidence for a giant impact; what effect would such an impact have on the planet and what traces would it leave today?

A giant impact (Figure 5) is thought to be responsible for Mars' current spin rate (Dones and Tremaine, 1993; Craddock, 2011); studies suggest that the mass of the impactor was at least 2% that of Mars, of the order of 10^{22} kg. Such an impact would also leave behind a large crater, which would subsequently have been filled to form a relatively flat basin: Borealis, Elysium and Daedalia basins have been identified as possible candidates (Craddock, 2011). An analysis of the elongated crater population on the surface of Mars, supposing that they are all due to impacts of debris from the disk or from the decaying orbit of moons (Schultz and Lutz-Garihan, 1982), suggested

that the mass of the disk was of the order of 10^{19} kg (Craddock, 2011). However, this elongated crater population may also result from grazing asteroid impacts (Bottke et al., 2000), which would allow for less massive disks.

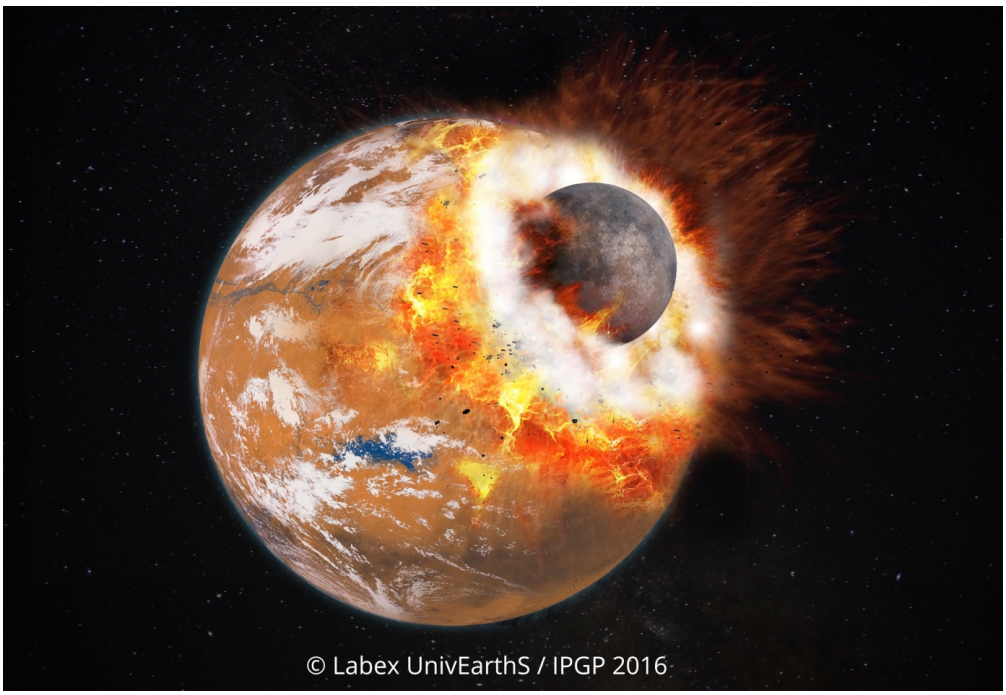

Figure 5: Illustration of a giant collision between the Proto-Mars and a smaller size body (1/3 to 1/4 the size of the impacted planet). Copyright Labex UnivEarthS – USPC – 2016.

On the other hand, the Borealis basin is the largest potential impact basin, measuring 10600 km by 8500 km and covering over 40% of the Martian surface, corresponding to the major hemispheric crustal dichotomy identified on the topography and gravity maps of Mars (Marinova et al., 2008). Numerical models based on the Smoothed Particle Hydrodynamics (SPH) approach conclude that a crater of the size of the Borealis basin can be formed by an object of mass 2.6% that of Mars, moving at about 6 km/s and impacting the surface at 45° (Marinova et al., 2008). These parameters are compatible with the kinds of impact thought to have occurred in the early history of the solar system (Wilhelms and Squyres, 1983) and can account for the spin rate of Mars (Dones and Tremaine, 1993). They have been used in subsequent, chemistry-focused SPH calculations of the nascent accretion disk just after the giant impact (Citron et al., 2015; Hyodo et al., 2017a; Pignatale et al., 2018). Others authors (Canup & Salmon, 2018) however argued for an impactor about ten times less massive with similar impact angle and a slightly higher impact velocity (7 km/s instead of 6 km/s), although still within the range of impactor size/energy estimates to form Borealis. However, these impact conditions cannot fully account for the spin of Mars.

2.3.2 Post-impact dynamical evolution of the debris cloud blasted in Mars' orbit: Formation of an accretion disk

Immediately after the giant impact, the ejecta that will eventually form Phobos and Deimos have highly elliptical orbits around Mars, with eccentricities between 0.1-0.9, and generally move at velocities different from those of their neighbours (Citron et al.,

2015; Hyodo et al. 2017a; Canup and Salmon 2018). At this stage, since the typical temperature is around 2000 K (Figure 6), the ejecta are mostly in the form of molten droplets whose size is determined by the interplay between their differential or shear velocity and the tension on the surface of the droplet. Assuming a surface tension of 0.3 N/m for a silicate melt yields a typical droplet size just after the giant impact of about 1.5 m (Hyodo et al. 2017a). The droplets will quickly solidify since their cooling time, several tens of minutes, is relatively quick compared to their orbital period. As they orbit, the ejecta may collide with each other and undergo further fragmentation, resulting in grains of the order of 100 micron in size (Hyodo et al. 2017a). The eccentricity of the orbits is damped by such collisions and eventually a thin circular disk of debris is formed (Hyodo et al., 2017b). When the midplane of the disk is initially not aligned with the equatorial plane of Mars, the dynamical flattening term J_2 of Mars' gravitational potential induces a precession of the disk particles symmetrically around the equatorial plane. Particle-particle inelastic collisions additionally damp their inclination, eventually forming an equatorial circular disk (Hyodo et al. 2017b).

SPH calculations modelling the Borealis-type impact indicate that the resulting disk would have a mass of several 10^{20} kg (Citron et al., 2015; Rosenblatt et al., 2016; Hyodo et al., 2017a), somewhat larger that the value estimated by Craddock (2011) and by Canup & Salmon (2018), about 10^{18} – 10^{19} kg. Crucially for the formation of Phobos and Deimos, the calculations also suggest that while most of the total ejected mass is confined below the Roche limit, roughly 1% lies beyond this, forming a tenuous outer disk of material that can extend past the synchronous limit (Rosenblatt et al., 2016; Canup & Salmon, 2018). The resolution of the SPH calculations however is not sufficient to provide a precise value for the outer disk mass, nor its density profile.

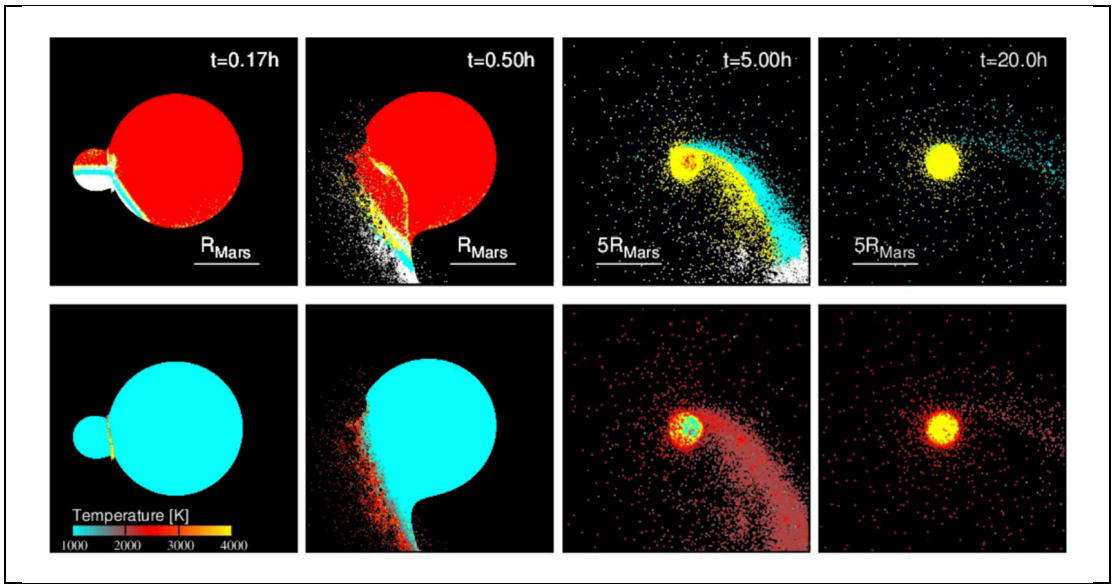

Figure 6: Snapshot of Smooth Particles Hydrodynamics (SPH) simulations of the Martian moons forming impact (adapted from Hyodo et al., 2017a). The orbital evolution of the orbit and temperature (color bar in Kelvin) of the blasted particles is shown on the top and bottom panels, respectively. The simulations run over 20 hours after the impact. The red, yellow, white and cyan dots of the top panel represent particles of Mars, falling on Mars, escaping from Mars, and forming a circum-Martian disk, respectively. Similar results have been obtained from other SPH simulations by Citron et al. (2015) and by Canup & Salmon (2018). The latter authors however considered a lower impactor mass and thus a lower-energy impact.

Furthermore, some impact-debris could have escaped from Mars' gravity field and started to orbit around the sun. If this ejecta hit a primordial asteroid with a high impact

velocity (> 5 km/s), the impact signatures (such as impact melt or/and ^{40}Ar-^{39}Ar resetting age) can be recorded (Hyodo & Genda 2018). Also, the Borealis-forming impact would excavate Martian mantle material (that is olivine-rich) and some of them are potentially implanted in the asteroid region as rare A-type asteroids (Polishook et al. 2017, Hyodo & Genda 2018).

2.3.3 Chemistry of the debris cloud

As SPH computations show that the disk material is initially made of a mixture of gas (vapour) and melt (Hyodo et al., 2017a), Phobos and Deimos should be formed from the condensation of these two components. SPH calculations also suggest that the basic building blocks of the two moons are composed of roughly half-Martian and half-impactor material (Hyodo et al., 2017a), assuming a high-energy Borealis-forming impact (Marinova et al., 2008). A lower-energy impact could result in a higher proportion, up to 80%, of Martian material (Canup & Salmon, 2018).

As the disk cools, the gas condenses into small crystalline dust grains and the melt solidifies (Ronnet et al., 2016). Thermodynamic calculations coupled with dynamical modeling can be used to predict the composition of the building blocks that will accrete into moons (Visscher and Fegley, 2013). In particular, since the impactor may originate far from where Mars itself formed, the question arises as to whether differences in the impactor's chemistry (such as cometary or carbonaceous chondrite) leave a detectable trace in the composition of Phobos and Deimos (Craddock, 2011; Ronnet et al.,2016; Pignatale et al., 2018). This is an important question since, as mentioned in section 2.2.2, spectral observations of the surfaces of Phobos and Deimos are unable to clearly determine their composition. Reflectance spectra suggest some carbonaceous material (Fraeman et al., 2014), while emissivity spectra strongly point to the presence of silicates (Giuranna et al., 2011).

The thermodynamic calculations, using different types of impactor, predict a great diversity of final compositions for impactors carrying different amounts of C, H, O, Fe, Si; changing the proportion of these elements can significantly modify the resulting chemistry of the dust and melt (Pignatale et al., 2018). For example, a CV-chondrite type (anhydrous carbonaceous) type impactor would bring metallic iron, silica, iron sulfides and carbon; a cometary object would bring the largest carbon and water ice content; an enstatite chondrite would bring the largest quantities of sulfides.

The presence or absence of compounds such as metallic iron, iron oxides and iron-rich silicates, sulfides, carbon and water ice can therefore hint at the nature of the impactor. Most of the impactors (carbonaceous-, enstatite-, and mars-type) produce iron-rich dust and some (carbonaceous-, cometary-type) also produce substantial quantities of carbon-rich dust, an opaque material, which thus lowers the albedo of the surface of the accreted bodies. Furthermore, as the grain size does not exceed 0.1~10 microns (Hyodo et al., 2017a), the reflectance of the surface is reduced (Ronnet et al., 2016). The solidified material also tends to lack a perfect crystalline structure, reducing the reflectance further. The small amount of dust (at most 5%) in the final material may nonetheless explain the low reflectance spectra of the surface of Phobos and Deimos (see section 2.2.2 and figure 3).

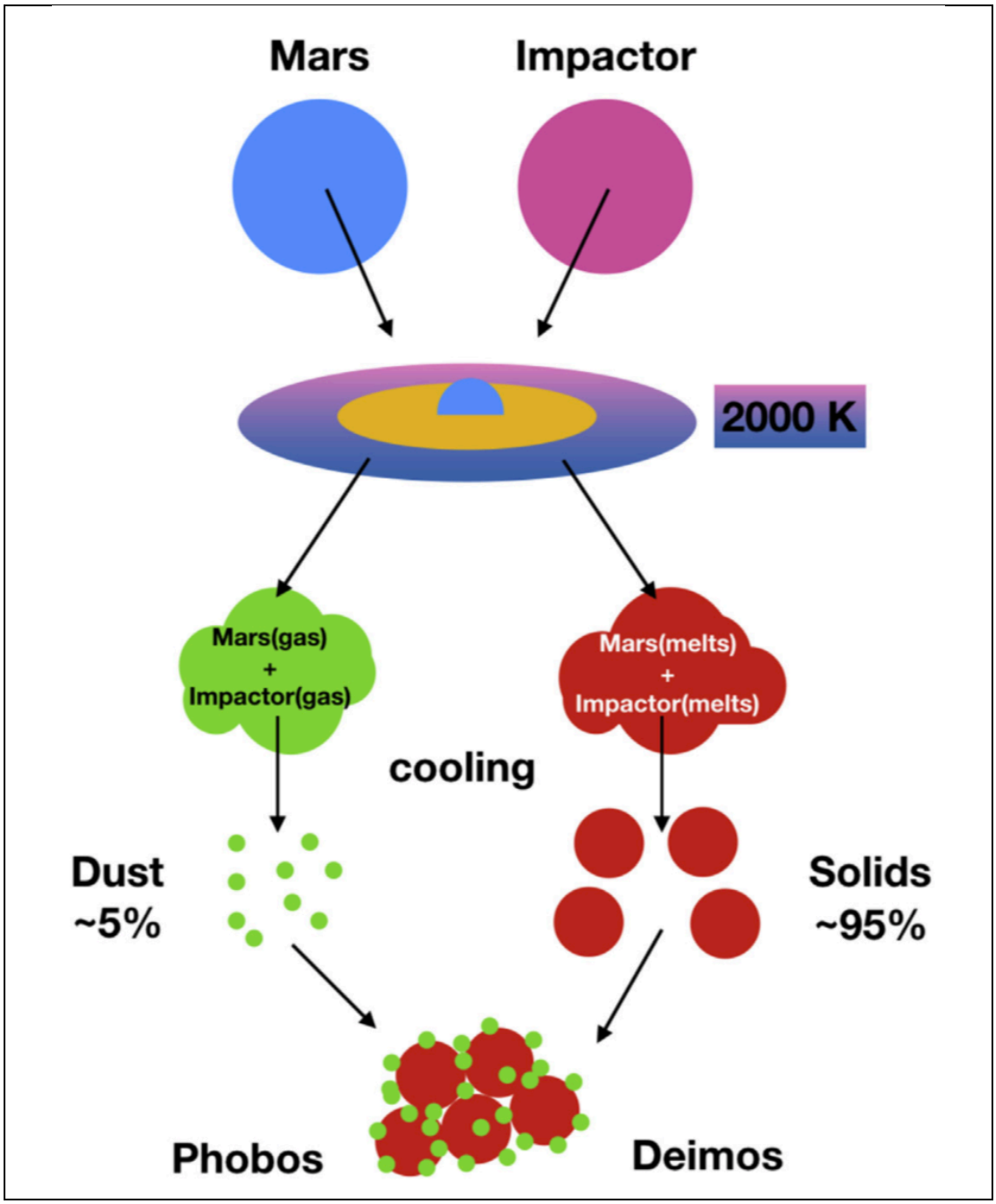

Figure 7: Schematic illustration of the chemical modeling of the giant impact scenario (from Pignatale et al., 2018). After the impact, some of the Martian material is ejected out at high temperature and vaporizes into gas, together with part of the impactor. The gas mixture then condenses into dust. On the other hand, the unvaporized material from Mars and the impactor forms a melt and then solidifies. Phobos and Deimos are the result of the accretion of these two components. The yellow region represents the part of the disk within the Roche limit (Hyodo et al. 2017a).

The possible imperfect crystallisation of melt could result in compositional variability for the building blocks of Phobos (Pignatale et al., 2018), which may reflect the so-called blue and red spectral units observed at the surface of Phobos (Murchie et al., 1991, see also figure 2). Indeed, such chemical variability seems necessary in order to explain the puzzling stratigraphic relationship between the blue and red units observed throughout the area of the large impact crater Stickney (Basilevsky et al., 2014).

Moreover, all types of impactor composition considered in Pignatale et al. (2018), except the CI-chondrite type (water-rich carbonaceous), produce a low amount of iron-rich silicates in the dust, which could explain the emissivity signature of Phobos' surface (Giuranna et al., 2011). In addition, the melt concentrates minerals of silicate-rich minerals that may explain the good match between Phobos's emissivity spectra and those of silicate material (Giuranna, 2011).

The material condensed in Mars orbit after a giant impact hence may not be incompatible with the spectral observations of the surface of the Martian moons, thus would not require any asteroidal material formed beyond Mars' orbit to account for these spectral observations. However, more detailed simulations of reflectance and emissivity spectra for the predicted condensed material are needed to assess the matching with Phobos' and Deimos' spectra. These studies are challenging since the additional space weathering effect is only well known for silicate material. The matching of simulated and observed spectra can therefore yield ambiguous results (Gaffey, 2010).

In their giant collision model, Canup & Salmon (2018) predict a disk debris temperature similar to the one in Hyodo et al. (2017a) but a different Mars-to-impactor ratio of the debris composition (80% Mars – 20% impactor). The final composition however should be quite similar to that predicted by Pignatale et al. (2018) for a Mars-like impactor (which results in a full Mars' composition). Nevertheless, a smaller amount of iron-rich silicate dust should be present, thus decreasing the darkening of the reflectance spectra that would hinder a comparison with observed reflectance spectra.

If the giant impact hypothesis is correct, depletion of volatile such as water vapour may occur since the impact is generally energetic (Hyodo et al. 2017a, Nakajima and Canup, 2017; Hyodo et al. 2018). Hyodo et al. (2018) consider two possible mechanisms for volatile depletion: hydrodynamic escape of vapour and blow-off of the volatile-rich condensates from the vapour by radiation pressure. The vapour temperature just after the impact is T_{VAP}~2000 K and the orbits of the debris are highly eccentric (Hyodo et al., 2017a), increasing their chance of escaping the system as the distance to Mars becomes larger. SPH calculations indicate that 10-40 % of the vapour satisfies the escape conditions during the first orbit from the impact point, depending on the impactor composition and vapour temperature between (1000-2000 K). Since the vapour contains more volatile elements than the melt, some fraction of the volatile may be lost from the original abundance by hydrodynamic escape (Hyodo et al., 2018).

Along the trajectory of the debris from impact point to apocenter (at the farthest distance from Mars), some fraction of the vapour may also condense and form small volatile-rich dust particles. The heat on Mars' surface generated by the impact (2000-6000 K) is strong enough to blow-off these small dust particles; "moderately" volatile elements, whose the condensation temperature is of 700-2000 K, and whose ratio of radiation pressure to gravitational forces is larger than 0.1, are most likely to be removed by radiation pressure (Hyodo et al. 2018). This loss of volatile elements has to be taken into account in any prediction of the final composition of the material condensed in Mars orbit from a giant collision.

2.3.4 Evolution of the accretion disk

SPH calculations of the initial impact and the nascent accretion disk are computationally very demanding, and 3D hydrodynamic simulations are therefore limited to 10-20 hours after the impact. This is however sufficient to study the orbital distribution of the blasted material around Mars that will then form the accretion disk (see section 2.3.2 and figure 6). Describing the long-term evolution of this multi-fluids disk (vapor mixed with solids) with a hydrodynamics code is however not feasible with the computing resources available today.

SPH calculations however provide material radial distributions whose density decreases with distance away from Mars. The calculations do not have enough resolution to provide fine details of the disk structure. Nevertheless, most of the mass is clearly concentrated below the Roche limit, and can form a dense inner disk, while the rest of the material, which extends slightly beyond the synchronous limit, forms a low-density outer disk (Rosenblatt et al., 2016; Hyodo et al., 2017; Canup and Salmon 2018).

The physics of the dense inner disk is similar to that of a viscous fluid (Salmon et al., 2010). The strong effective viscosity results from the formation of spiral self-gravitating wakes, owing to the large surface density of the inner disk. As a result, the inner disk spreads outwards from the planet. When material crosses the Roche limit, it can accrete into individual moons (low mass satellites, Charnoz et al., 2010). The orbital evolution of these moons is then driven by two opposite forces due to their gravitational interaction with the inner disk material (which transfers angular momentum to the moon orbits, thus repelling them) and with the planet (through tidal dissipation which reduces the angular momentum of the moon orbit, see section 2.3.6). The former interaction pushes the orbit of each moonlet outwards while the second pulls it back towards the planet when the orbit is below the synchronous limit. Beyond this limit, the two forces act in the same direction and the moonlet migrates outwards definitively, but very slowly. This mechanism has successfully explained the formation of the small moons of Saturn from the planets's ring system, where the synchronous limit is in fact slightly below the Roche limit (Charnoz et al., 2010).

In the case of Mars, the synchronous limit (6 R_M) is far beyond the Roche limit (about 2.45 R_M). After the giant impact, the inner disk is massive, and disk-satellite interactions dominate planet-satellite tidal interactions. Thus, any moonlet forming at the Roche limit is initially pushed outward. However, as the disk's edge is located at the Roche limit, disk-satellite interactions cannot push a satellite beyond the synchronous limit; the maximal outward migration distance is defined by the 2:1 Lindblad resonance with the outer edge of the inner disk (i.e. the Roche limit), which is about 4.5 R_M (Charnoz et al., 2010; Rosenblatt & Charnoz, 2012).

Over time, the dense inner disk empties, losing material either inwards to the surface of Mars or outwards across the Roche limit. As the disk density decreases, the Lindblad resonances become weaker (i.e. disk-satellites interactions decrease) and tidal dissipation eventually dominates, causing the orbits of any moonlet below the synchronous limit to decay. Eventually all these moonlets disappear below the Roche limit. The lifetime of the moonlet system depends on the mass of the inner disk; for a disk of mass 10^{19} kg, moonlets with the mass of Phobos of Deimos can form, but they

completely disappear after 200 Ma (Rosenblatt & Charnoz, 2012), which is much lower than the presumed age of Phobos' surface, which is estimated as old as 4 billion years (Schmedemann et al., 2014). A more massive disk would evolve even faster and would produce more massive moonlets, while a lighter disk would evolve more slowly but would produce moonlets less massive than Phobos and Deimos.

As the moons cross back below the Roche limit, they do not necessarily crash onto the surface of Mars. They can be disrupted by the tidal forces of Mars, breaking apart to form a new inner disk less massive than the initial disk (Black & Mittal, 2015). The whole process of moon formation can then restart from this new less massive disk. It has been suggested that Phobos today is the result of the latest iteration, 2.5 billion years ago, of such a cycle of disk formation and dispersal processes, initially triggered by a giant impact (Hesselbrock and Minton, 2017). However, a caveat of this scenario is the absence of a faint remnant ring around Mars.

These studies however do not take into account the low-density outer disk whose existence is suggested by SPH simulations. The question then is, could Phobos and Deimos have formed from the material in this outer disk?

2.3.5 How to form two small outer satellites from a circum-Martian accretion disk: A dynamical solution.

Since the density of the outer disk is low, it can be represented by a set of small bodies, or satellite embryos, rather than as a viscous fluid as was done for the dense inner disk. The evolution of these satellite embryos can be followed by numerically integrating the N-body equations of motion. A collision is commonly deemed to have occurred if two bodies approach each other to within their mutual Hill radius. The collision is treated as inelastic, resulting in accretion if the relative rebound velocity is smaller than the mutual escape velocity. One caveat is that disruption (i.e. the break-up of one or both colliding bodies) is neglected, based on the assumption that the resulting fragments remain close to each other and thus quickly recombine.

N-body simulations of the evolution of such an outer disk usually result in a stable configuration involving typically a dozen or so small moons whose orbits change little so that there are no more collisions (a dynamically ‘frozen’ system). The masses and orbits of these moons reflect the initial density profile of the disk due to the conservation of the center of mass (Rosenblatt et al. 2016). For instance, the moons tend to be homogeneously distributed if the accretion disk is uniform. In order to enhance accretion efficiency, and hence the possibility of forming Phobos and Deimos with their actual masses at the expected distances from Mars, it is necessary to somehow dynamically excite the outer disk.

Such an excitation is provided by the outward migration of the more massive transient inner moons that form at the Roche limit. The satellite embryos in the outer disk can be trapped in mean-motion resonances with the inner moons (when the ratio of their orbital period is a ratio of two integers), and follow concurrently their outward migration. The accumulation of embryos in a resonance favours accretion through collisions, while collisions also provide a mechanism of escaping the resonance. In approximately one third of the results reported by Rosenblatt et al (2016), two moons

were formed by this mechanism, the more massive lying below the synchronous orbit and the less massive lying above it as is the case in the Martian system (table 1 & 2).

Since more massive inner moons migrate more quickly, the rate of collisions and hence the possibility of accretion can increase, which can lead to cases where all the debris in the outer disk has been accreted onto one or more of the inner moons. This in turn suggests a limit for the mass of the inner disk and hence of the initial impactor (Canup and Salmon, 2018). These authors place this limit at around $2x10^{21}$ kg (impactor) and $2x10^{19}$ kg (disk) compared to the values of $2x10^{22}$ kg (impactor) and $5x10^{20}$ kg (disk) in Rosenblatt et al. (2016). Although the initial mass of the disk, and thus the energy of the impact in both studies differ significantly, the basic process of forming moons from re-accretion of debris after a giant collision with Mars is similar (Figure 8).

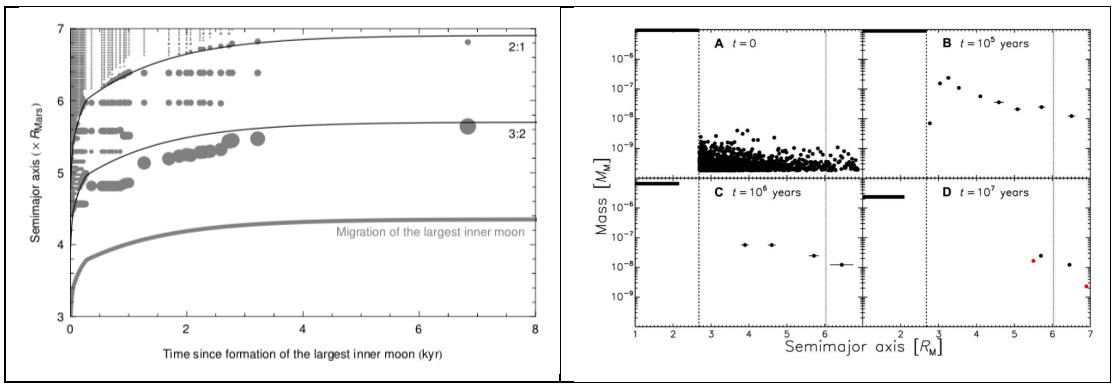

Figure 8: Accretion of satellite-embryos in the outer part of the accretion disk. (Left) from Rosenblatt et al. (2016): the accretion of embryos is facilitated by Mean Motion Resonances with the largest inner moon (1000 times the mass of Phobos) as it migrates outwards, requiring a high-energetic impact such as the canonical widely accepted Borealis-forming impact. After about 8000 years only two small satellites survive on each side of the synchronous limit at 6 RM. (Right) from Canup & Salmon (2018): the accretion of embryo follows same physical modeling as in Rosenblatt et al. (2016) but all inner moons and their resonance interactions are taken into account and the tidal dissipation of Mars is significantly higher. Similar results are obtained after 10 million years and a less energetic impact is required.

As well as increasing the semi-major axis of a trapped satellite embryo, mean-motion resonances can also increase its eccentricity. More massive inner moons migrate more quickly, leading to larger eccentricities for the satellite embryos. These can be reduced through collisions and accretion processes, but in numerical simulations (Rosenblatt et al., 2016) the final two outer moons often have eccentricities somewhat larger than those of Phobos and Deimos today. Tidal forces acting over billions of years can help damp these eccentricities, as discussed in the section 2.3.6. Alternatively, if the mass of the initial impactor is smaller, the inner disk and hence the moons formed from it will be less massive. The outward migration would then be less rapid, the mean-motion resonances would have less effect which could result in more numerous small moons in the outer disk with smaller eccentric orbits (Canup and Salmon, 2018).

2.3.6 Orbital evolution of the Martian satellites after the accretion period

If tidal evolution cannot allow capture scenarios (section 2.2.3), it also sets stringent constraints on accretion scenarios. Compared to other planets with moons in our solar system, for Mars the ratio of the centrifugal acceleration to gravitational acceleration is quite small, resulting in a relatively distant synchronous limit at about 6 R_M. In contrast

to the Earth, this ratio may have barely changed throughout Mars' history (Dones and Tremaine, 1993). The Martian system therefore best illustrates the following rule (Murray and Dermott, 1999): moons above the synchronous limit recede away and siphon off angular momentum from the planet (Deimos behaves like most moons in the solar system, including Earth's Moon), while moons below the synchronous limit fall back and restore angular momentum to the planet (Phobos is the most notorious example, but Mars likely had many more moons in the past, see section 2.3.4).

The precise orbital tidal evolution is controlled by gravitational torques from the tidal bulges raised on Mars by the moons, and from the tidal bulges raised on the moons by Mars. The evolution equations (Kaula, 1964) depend on a set of parameters $k_2/Q(\chi)$ describing tidal dissipation: k_2 is the degree-2 potential Love number and $Q(\chi)$ is the tidal quality factor at the principal tidal frequency χ (Efroimsky and Lainey, 2007). The Love number k_2 depends weakly on frequency; for Mars it can be estimated from tidal perturbations on the orbital motion of Martian spacecraft, which gives a k_2 value equal to 0.169 with an error of about 2% (Konopliv et al., 2016; Genova et al., 2016); for the moons, it has not been measured but models predict $k_2 \sim 10^{-4}$ for monoliths with a silicate composition (Lambeck 1979) and $k_2 \sim 10^{-3}$ for rubble piles also with a silicate composition; the porosity indeed decreases rigidity (Jaeger et al., 2007) and in turn increases k_2 (Rosenblatt et al.,2011; Le Maistre et al., 2013), which would be consistent with the high porosity inferred from the mass and volume of Phobos (Andert et al., 2010; Rosenblatt 2011). The quality factors $Q(\chi)$ depend strongly on the principal tidal frequency χ; for Mars it can be estimated at the current semi-diurnal frequency from the secular acceleration of the mean anomaly of Phobos' current orbit, which yields $Q = 82.8 \pm 0.2$ (Jacobson, 2010). The quality factors for Phobos and Deimos have not been measured but rubble piles are expected to be more dissipative than non-porous rocks, with $Q < 100$ (Goldreich and Sari, 2009).

In the course of tidal evolution, the orbit of the Martian moons shrinks or expands, according to whether it is within or beyond the synchronous limit, mainly due to dissipation within the planet, and circularises mainly due to dissipation within the moon (Goldreich, 1963); the inclination is barely affected (Mignard, 1981). As the orbit tidally evolves, it passes through several resonances, mainly between the mean motion and Mars's spin at 3.8 R_M (a 2:1 resonance) and 2.9 R_M (a 3:1 resonance), which will generally re-excite the eccentricity (Yoder, 1982). Other resonances, for example between the pericentre and Mars's mean motion, are harder to model (Yokoyama, 2002), given the chaotic variations of Mars' obliquity (Laskar and Robutel, 1993; Touma and Wisdom, 1993).

If Phobos and Deimos formed from a massive initial disc of debris, with a mass $\sim 10^{-3}$ M_M (where M_M is the mass of Mars), corresponding to an impactor of mass $\sim 10^{-1.5}$ M_M (Citron et al., 2015), mean motion resonances with large transient moons (see section 2.3.5) could facilitate the formation of exactly two moons with the correct semi-major axes, but with an eccentricity of around 10^{-2} for Deimos (Rosenblatt et al., 2016). Damping this eccentricity by tidal forces to that observed today would require k_2/Q to be of the order of 10^{-4} for Deimos, at the upper limit of the expected range for rubble piles, and of the order of 10^{-6} for Phobos, at the lower limit of the expected range for monolithic rocks, thus implying a different structure or composition for the two moons. If Phobos and Deimos formed from a less massive initial disk of debris, with a mass or around 10^{-5} M_M, corresponding to an impactor of mass about 10^{-3} M_M, mean motion

resonances would be largely ineffective, preventing undesirable excitation of eccentricities, but with the result that several moons could be left orbiting Mars (Canup and Salmon, 2018). For these to disappear, the value of k_2/Q for Mars would have to be an order of magnitude larger than that presently observed, which makes the current orbital configuration with exactly two moons much less likely. The current resolution of SPH simulations is however too coarse to model the distribution of mass in the outer region of the initial disc of debris.

2.4 Conclusion on the formation of the Martian moons

The formation of moons in the solar system is a long-standing topic of research (Peale & Canup, 2015). Each moon system has unique characteristics, making it difficult to envisage a common mechanism of formation. Recent spacecraft exploration of giant planets, in particular the Cassini mission around Saturn, have brought to light the role played by rings of debris and tidal forces on the formation and orbital evolution of small moons (Crida and Charnoz, 2012). Similar processes can explain the formation of Phobos and Deimos in a disk following a giant impact on Mars. A robust scenario must however be able to explain the formation of two small moons rather than a single massive one. The spin imparted to the planet by the impactor plays a major role, as this determines where the synchronous limit is, in particular if it is within or beyond the planet's Roche limit. A post-impact fast rotator will have a synchronous limit close to the planet, which favours the accretion of debris into a single body, as in the case of Earth's moon. A post-impact slow rotator such as Mars, with a spin of about 24 hours, corresponds to a relatively far synchronous limit; moons that form close to the Roche limit, by viscous spreading of the disk, migrate outwards through the interaction with the remnant disk, but under tidal forces they will eventually fall back towards Mars. Only small moons formed close to or beyond the synchronous limit are expected to remain in orbit for a long time. The current spin of Mars is an argument in favour of a relatively massive impactor, which could also be responsible for the formation of the Borealis basin (Hyodo et al., 2017b).

Numerical simulations for the complete scenario, from the initial impact to accretion and the long-term evolution of the two moons, yield better agreement with the present orbits than the previous widely-accepted capture hypothesis, and are still compatible with the observations concerning their composition. The amount of material blasted into orbit primarily depends on the mass of the impactor and on the angle of impact. This is crucial as it drives the evolution of the debris cloud into an accretion disk, as well as determining its eventual chemical composition. The various collision parameters are however difficult to constrain as they depend on the detailed dynamics of the early solar system (Hansen, 2018).

JAXA (Japan Aerospace eXploration Agency) plans a sample return mission from Phobos in the 2020s. The Martian Moons eXploration (MMX) probe will collect about 10 grams of material from Phobos' regolith. If the giant impact hypothesis is correct, MMX would collect not only material from the impactor but also from Mars, including ancient mantle material (Hyodo et al., 2017a). The detailed composition of these samples would help constrain the thermodynamical environment in which they formed and hence the parameters of the giant impact.

Further observations and analysis are thus required to test the giant impact hypothesis and future sample return missions such as MMX will give critical information about the composition (Murchie et al., 2014; Usui et al., 2020) and hence the origin of the Martian moons, Phobos and Deimos.

2.5 Perspectives and research project

The next step in the exploration of the Martian moons is obviously the JAXA-MMX sample return mission to test models of their formation, as well as models of early solar system dynamics since the Martian system may retain material exchanged between the inner and outer solar system (e.g. Usui et al., 2020).

For the preparation of the analysis of this Phobos surface sample and of MMX in-situ observations, further investigations can be led on the giant collision scenario.

2.5.1 Tidal dissipation properties of the Martian system throughout its history

The post-accretion tidal evolution of the orbit of the two small outer satellites requires tidal dissipation rate three orders of magnitude higher inside Deimos than inside Phobos to account for their current orbit (see Section 2.3.6). It is difficult to explain such a difference between two small rocky bodies supposed to form in a same accretion disk, and so to have the same composition. A higher tidal dissipation rate is however expected inside early Mars, which in turn would require less dissipation rate inside the moons to change their post-accretion orbits into the current orbits over four billion years.

I propose to investigate the plausible k_2 and Q values (k_2 is the potential Love number and Q the tidal quality factor) of Mars throughout its history in order to assess the impact on the tidal orbital evolution of its two moons[50]. This investigation will rely on modeling of the thermal evolution of Mars' interior, using the best constraints on the interior rheological properties of the planet (e.g. Samuel et al., 2019). Particular attention will be paid to the early Mars epoch, including the effect of a giant impact in the thermal state of the "collided" Mars.

The tidal dissipation rate of the moons is not expected to evolve with time since the two bodies are too small to generate any interior thermal activity. However, their k_2 and Q values also require investigation since they depend on both composition and internal structure. A large amount of porosity can indeed increase the k_2 value (see Le Maistre et al., 2013) but it is still unclear whether it will significantly affect the Q value (Rosenblatt, 2011).

This investigation of the evolution of the interior and of the rheological properties of Mars and its moons, should yield a plausible range for the k_2/Q values that will then be used to revise the orbital evolution of the Martian moon system after accretion. The possible dependence of Q with the orbital frequency will also be taken into account (e.g. Rosenblatt and Pinier, 2014).

[50] The rate of a moon orbital changes due to tidal dissipation inside the planet is proportional to the k_2/Q ratio of the planet (e.g. Kaula, 1964)

2.5.2 The non-tidal evolution of the Martian moon orbits

The high tidal dissipation rate inside Deimos, required by the giant collision scenario, is explained in part because of the very small eccentricity of Deimos' current orbit (0.00027, see table 1). This eccentricity could however change due to gravitational resonances with Phobos at time-scales shorter than billion years (as emphasized for Phobos by Yoder (1982)). As the resonances increase the eccentricity, the small current value would thus not be representative of the value to be reached by long-term evolution of the post-accretion orbit in the giant collision scenario. In turn, it may require less tidal dissipation inside Deimos than estimated in Rosenblatt et al. (2016).

I propose to study the variations of the orbital eccentricity of Phobos and Deimos over millions years in order to obtain possible ranges for their variations. The orbital motion will be numerically integrated as a 3-body system. The range of eccentricity will then be used as the values representative of the current orbit of the two moons to be taken into account in long-term evolution of the orbit from the post-accretion phase to present, yielding a range of required tidal dissipation in the giant collision scenario (see section 2.5.1).

This investigation is challenging since it requires the pertinent choice of the numerical integrator and would face issues with the current computer capabilities. An integration time step shorter than for long-term evolution computations is indeed required in order not to smooth the possible range of eccentricity variations.

2.5.3 The composition of the moons and their remote sensing data

In the giant collision scenario, the main part of the material (95%) forming Phobos and Deimos comes from the solidification of the melt phase, and its composition is dominated by olivine and pyroxene crystalline phases (see Table 3). Nevertheless, a complex of absorption bands around 1 and 1.9 microns, expected from these crystalline phases, is not observed in the reflectance spectra of both moon surfaces (Figure 3). If the moon material is indeed rich-olivine and pyroxene, then no satisfactory explanation has been given so far to explain this discrepancy (see Section 2.2.2).

Resulting CIPW-norm of the Melt Phase

	+Mars	+CV	+EH	+CI	+COMET	BSM	BSM (Ronnet et al. 2016)
Anorthite	8.08	9.69	8.24	8.35	1.39	3.16	
Diopside	3.08	3.63	2.97	3.13	0.00	6.89	6.97
Pyroxene	43.41	55.48	57.58	52.35	54.97	21.03	21.29
Albite	0.00	0.00	0.00	0.00	0.00	8.29	
Orthoclase	0.00	0.00	0.00	0.00	0.00	0.65	0.66
Olivine	45.19	29.68	31.05	35.98	34.66	58.50	59.22
Ilmenite	0.25	1.52	0.17	0.19	6.40	0.27	0.00
Corundum	0.00	0.00	0.00	0.00	2.59	0.00	0.00
Anorth+Alb	0.00	0.00	0.00	0.00	0.00	(11.45)	11.59
Oli/Pyr	1.04	0.53	0.62	0.68	0.63	2.78	2.78

Table 3: Predicted composition of the circum-Martian accretion disk material (giant collision scenario) resulting from the solidification of the melt phase (95% of the disk material). From Pignatale et al. (2018).

Ronnet et al. (2016) have proposed that the condensation of a gaseous phase produces very fine particles (2 microns or smaller), which in turn remove any absorption bands in the reflectance spectra. In their calculations, however, Hyodo et al (2017a) found larger particles (up to 100 microns) in the disk. On the other hand, particularly efficient space weathering may explain the complete removal of expected olivine and pyroxene absorption bands (e.g. Murchie and Erard, 1996). Such a process is however not documented since the actual composition of the Martian moons is unknown (Pieters et al., 2014). The melt phase could also have solidified fast enough to prevent the formation of crystals, i.e. amorphous solidification or a vitrification process. In that case, no crystalline phase can be formed and no absorption bands can be observed. This explanation is however challenging because the vitrification is not a permanent state of the matter (Zanotto and Mauro, 2017) and it is unclear whether it could be maintained over billion years at the surface of airless bodies.

I propose to test some of these possible explanations of the discrepancy between expected composition from a giant scenario and reflectance spectral data of the moon surfaces. Laboratory analogs of the material predicted by a giant collision (Pignatale et al., 2018) will be produced. Their reflectance spectra will then be measured depending on the particle sizes and others surface conditions (see Vernazza et al., 2010; Cipriani et al., 2011). The impact of both composition, particle size, and possible space weathering processes, on the reflectance spectra of Phobos and Deimos material predicted by the giant collision scenario will be tested. I also propose to perform these laboratory measurements in the thermal emissivity wavelength range since the emissivity spectra of Phobos surface support a silicate composition (Giuranna et al., 2011).

The vitrification process is an investigation that has not been performed so far for the study of the Martian moons. The first step of this investigation is to study the rate of cooling of the melt phase, i.e. the cooling of droplets of 1.5 meters size blasted into Mars' orbit by the giant collision (Hyodo et al., 2017a). This theoretical investigation will check the conditions needed to prevent the formation of crystals. Maintaining the vitrification (amorphous phase) is another problem which requires a collaboration with experts in the domain, especially for a rich-olivine pyroxene material.

2.5.4 The internal structure of accreted small size bodies

The giant collision scenario however missed an important part of the accretion process. This modeled process starts with a distribution of up to 100 satellite embryos. If we assume they have the same density as Phobos, their size should be about 2 km. Hyodo et al. (2017a) have however shown that the accretion disk should be made of particles with a much smaller size (0.1 microns to about 100 microns). How do these fine particles accrete together to form satellite embryos with a kilometer in size? Alternatively, could Phobos and Deimos be formed only from the continuous accretion of these fine particles?

A continuous accretion would support homogeneous internal mass repartition inside the two moons, while a final stage accretion of kilometer-size embryos should lead to a heterogeneous interior. Homogenous vs heterogenous interiors could be measured by the geodesy experiment of MMX. Theoretical models of accretion of

small bodies in the circum-Martian disk around the synchronous orbit are thus required to interpret the results of this future experiment.

2.5.5 The physical properties of the Phobos returned sample.

Chemical analyses will be at the heart of the investigations led on the sample of Phobos surface returned by the MMX mission (Usui et al., 2020). This sample could however be corrupted by impact-ejected Martian and/or Deimos surface material. It will thus be interesting to measure some physical properties of this sample in order to further test the formation scenarios independently of the chemical analyses.

The rheological properties of the sample are important since they drive the post-accretion evolution of the orbit of the two satellites formed at the synchronous limit. The rheological parameters to measure are the shear modulus (related to the k_2 value) and the tidal dissipation factor Q. Such a measurement is however destructive and thus unlikely to be performed with only 10 grams of soil (Usui et al., 2020).

Another physical property of interest to test the giant impact scenario, is the remanent magnetization of the Phobos material. The melted material in the accretion disk likely cooled in presence of a dipole magnetic field around Mars and must have recorded this field when cooling (i.e. when its temperature dropped below the Curie temperature). The remanent magnetization of this material is expected to be larger than the magnetization of meteoritic material condensed in the solar nebula because early Mars had probably a strong dipolar magnetic field (Langlais et al., 2019).

I propose to use the predictions of the typical size, orbital distribution and composition of the debris blasted into Mars orbit by a giant collision (Hyodo et al., 2017a) to compute the typical cooling time of these debris (see Section 2.5.3). When the temperature drops below the Curie temperature (which depends on the kind of magnetic mineral the cooling debris contains), the magnetic field strength of early Mars is recorded as remanent magnetization at the place where the debris are on its orbit around Mars. For the variety of possible magnetic materials (Pignatale et al., 2018), the range of remanent magnetisation of the Phobos material will then be computed. These magnetisation predictions will be compared with magnetization measurements of meteoritic material in order to provide a reference for magnetization measurements of the future Phobos soil sample.

2.6 References

Andert, T.P., Rosenblatt, P., Paetzold, M., Haeusler, B., Dehant, V., Tyler, G.L., & Marty, J.C. (2010). Precise mass determination and the nature of Phobos. *Geophysical Research Letters 37*(9). https://doi.org/10.1029/2009GL041829

Basilevsky, A.T., Lorenz, C.A., Shingareva, T.V., Head, J.W., Ramsley, K.R., & Zubarev A.E. (2014). The surface geology and geomorphology of Phobos. *Planetary and Space Science*, *102,* 95-118. http://dx.doi.org/10.1016/j.pss.2014.04.013

Bibring, J.P. (2010). Phobos' origin: A reappraisal. In EPSC, Vol 5, EPSC2010-554 (abstract)

Black, B.A., & Mittal, T. (2015). The demise of Phobos and development of a Martian ring system. *Nature Geoscience 8*(12), 913-917. https://doi.org/10.1038/ngeo2583

Bottke, W.F., Love S.G., Tytell, D., & Glotch, T. (2000). Interpreting the Elliptical Crater Populations on Mars, Venus, and the Moon. *Icarus 145*(1), 108-121. https://doi.org/10.1006/icar.1999.6323

Bruck Syal, M., Rovny, J., Owen, J.M., & Miller, P.L. (2016). Excavating Stickney crater at Phobos. *Geophysical Research Letters 43.* https://doi.org/10.1002/2016GL070749

Burns, J.A. (1992). Contradictory clues as to the origin of the Martian moons. In H.H. Kieffer, B.M. Jakosky, C.W. Snyder, & M.S. Matthews (Eds.), Mars (pp. 1283-1301). Tuscon, Arizona, USA: University of Arizona Press.

Canup, R., & Salmon, J. (2018). Origin of Phobos and Deimos by the impact of a Vesta-to-Ceres sized body with Mars. *Science Advances, 4*(4). https://doi.org/10.1126/sciadv.aar6887

Cazenave, A., Dobrovolskis, A., Lago, B. (1980). Orbital history of the Martian satellites with inferences on their origin. *Icarus 44*, 730–744. https://doi.org/10.1016/0019-1035(80)90140-2

Charnoz, S., Salmon, J., & Crida A. (2010). The recent formation of Saturn's moonlets from viscous spreading of the main rings. *Nature, 465*(7299), 752-754. https://doi.org/10.1038/nature09096

Citron, R.I., Genda, S., & Ida, S. (2015). Formation of Phobos and Deimos via a giant impact. *Icarus, 252,* 334-338. https://doi.org/10.1016/j.icarus.2015.02.011

Cipriani, F., Witasse, O., Leblanc, F., Modolo, R., & Johnson, R.E. (2011). A model of interaction of Phobos' surface with the Martian environment. *Icarus, 212,* 643-648. http://doi.org/10.1016/j.icarus. 2011.01.036.

Clark, B.E., Hapke, B., Pieters, C., & Britt, D. (2002). Asteroid space weathering and regolith evolution. In B. Bottke, A. Cellino, P. Paolocchi, R. Binzel (Eds), Asteroids III (pp. 585-589). Tuscon, Arizona, USA: University of Arizona Press.

Craddock, R.A. (1994). The origin of Phobos and Deimos. Lunar Planet Sci XXV:293–294

Craddock, R.A. (2011). Are Phobos and Deimos the result of a giant impact? *Icarus 211*(2), 1150–1161. https://doi.org/10.1016/j.icarus.2010.10.023

Crida, A., & Charnoz, S. (2012). Formation of Regular Satellites from Ancient Massive Rings in the Solar System. *Science, 338*(6111). https://doi.org/10.1126/science.1226477

Dones, L., & Tremaine, S. (1993). On the origin of planetary spins. *Icarus 103*(1), 67-92. https://doi.org/10.1006/icar.1993.1059

Duxbury, T.C., Zakharov, A.V., Hoffmann, H., & Guinness, E.A. (2014). Spacecraft exploration of Phobos and Deimos. *Planetary and Space Science*, *102,* 9-17. http://dx.doi.org/10.1016/j.pss.2013.12.008

Efroimsky M., & Lainey V. (2007). Physics of bodily tides in terrestrial planets and the appropriate scales of dynamical evolution. Journal of Geophysical Research 112(E12), http://doi.org/10.1029/2007JE002908

Fraeman, A.A., Arvidson, R.E., Murchie, S.L., Rivkin, A., Bibring, J.P., Choo, T.H., … Zabalueva, E.V. (2012). Analysis of disk-resolved OMEGA and CRISM spectral observations of Phobos and Deimos. *Journal of Geophysical Research*, *117*, https://doi.org/10.1029/2012JE004137

Fraemann, A.A, Murchie, S.L., Arvidson, R.E., Clark, R.N., Morris, R.V., Rivkin, A.S., & Vilas, F. (2014). Spectral absorptions on Phobos and Deimos in the visible/near infrared wavelengths and their compositional constraints. *Icarus, 229*, 196-205. https://doi.org/10.1016/j.icarus.2013.11.021

Gaffey, M.J. (2010). Space weathering and the interpretation of asteroid reflectance spectra. *Icarus*, *209*(2), 564-574. https://doi.org/10.1016/j.icarus.2010.05.006

Genova, A., Goossens, S., Lemoine, F.G., Mazarico, E., Neuman, G.A., Smith, D.E., & Zuber, M.T. (2016). Seasonal and static gravity field of Mars from MGS, Mars Odyssey and MRO radio science. *Icarus 272*, 228-245. https://doi.org/10.1016/j.icarus.2016.02.050

Giuranna, M., Roush, T.L., Duxbury, T., Hogan, R.C., Carli, C., Geminale, A., & Formisano, V. (2011). Compositional interpretation of PFS/MEX and TES/MGS thermal infrared spectra of Phobos. *Planetary and Space Science, 59*(13), 1308-1325. https://doi.org/doi:10.1016/j.pss.2011.01.019

Goldreich, P. (1963). On the eccentricity of satellite orbits in the solar system. *Monthly Notices of the Royal Astronomical Society, 126,* 257. https://doi.org/10.1093/mnras/126.3.257

Goldreich, P., & Sari, R. (2009). Tidal evolution of rubble piles. *The Astrophysical Journal, 691*(1), 54–60. https://doi.org/10.1088/0004-637X/691/1/54

Hall, A. (1878). Discovery of satellites of Mars. *Monthly Notices of the Royal Astronomical Society*, *38,* 205-209. https://doi.org/10.1093/mnras/38.4.205

Hansen, B.M.S. (2018). A dynamical context for the origin of Phobos and Deimos. *Monthly Notices of the Royal Astronomical Society*, *475*(2), 2452-2466. https://doi.org/10.1093/mnras/stx3361

Hesselbrock, A.J., & Minton D.A. (2017). An ongoing satellite-ring cycle of Mars and the origins of Phobos and Deimos. *Nature Geoscience, 10*(4), 266-269. https://doi.org/10.1038/ngeo2916

Hurford, T.A., Asphaug, E., Spitale, J.N., Hemingway, D., Rhoden, A.R., Henning, W.G., … Walker M. (2016). Tidal disruption of Phobos as the cause of surface features. *Journal of Geophysical Research Planets 121,* 1054-1065. https://doi.org/10.1002/2015JE004943

Hyodo, R., Genda, H., Charnoz, S., & Rosenblatt, P. (2017a). On the Impact Origin of Phobos and Deimos. I. Thermodynamic and Physical Aspects. *The Astrophysical Journal, 845*(2). https://doi.org/10.3847/1538-4357/aa81c4

Hyodo, R., Rosenblatt, P., Genda, H., & Charnoz, S. (2017b). On the Impact Origin of Phobos and Deimos. II. True Polar Wander and Disk Evolution. *The Astrophysical Journal, 851*(2). https://doi.org/10.3847/1538-4357/aa9984

Hyodo, R., Genda, H., Charnoz, S., Pignatale, F.C.F., & Rosenblatt, P. (2018). On the Impact Origin of Phobos and Deimos. IV. Volatile Depletion. *The Astrophysical Journal 860*(2). https://doi.org/10.3847/1538-4357/aac024

Hyodo, R., & Genda, H. (2018). Implantation of Martian Materials in the Inner Solar System by a Mega Impact on Mars. *The Astrophysical Journal Letters, 856*(2). https://doi.org/10.3847/2041-8213/aab7f0

Jacobson, R.A. (2010) The orbits and masses of the Martian satellites and the libration of Phobos. *The Astronomical* Journal, *139*(2), 668–679. https://doi.org/10.1088/0004-6256/139/2/668

Jacobson, R.A., & Lainey, V. (2014). Martian satellite orbits and ephemerides. *Planetary and Space Science*, *102,* 35-44. http://dx.doi.org/10.1016/j.pss.2013.06.003

Jaeger, J.C., Cook, N.G.W., & Zimmerman, R.W. (2007). Micromechanical Models. In Blackwell Publishing (Eds.), Fundamentals of rock mechanics fourth edition (pp. 281-320). Oxford, UK.

Kaula, W.M. (1964). Tidal Dissipation by Solid Friction and the Resulting Orbital Evolution. *Review of Geophysics and Space Physics, 2,* 661-685. https://doi.org/10.1029/RG002i004p00661

Konopliv, A.S., Park, R.S., & Folkner, W.M. (2016). An improved JPL Mars gravity field and orientation from Mars orbiter and lander tracking data. *Icarus 274*, 253-260. https://doi.org/10.1016/j.icarus.2016.02.052

Lambeck, K. (1979). On the orbital evolution of the Martian satellites. *Journal of Geophysical Research 84*, 5651–5658. https://doi.org/10.1029/JB084iB10p05651

Langlais B., Thébault E., Houliez A., Purucker M.E., Lillis R.J., 2019. A new model of the crustal magnetic field of Mars using MGS and MAVEN. Journal of Geophysical Research 124 (6), 1542-1569.

Lantz, C., Clark, B.E., Barucci, M.A. & Lauretta, D.S. (2013). Evidence for the effects of space weathering spectral signatures on low albedo asteroids. *Astronomy & Astrophysics, 554.* https://doi.org/10.1051/0004-6361/201321593

Laskar, J., & Robutel, P. (1993). The chaotic obliquity of the planets. *Nature 361*(6413):608–612. https://doi.org/10.1038/361608a0

Le Maistre, S., Rosenblatt, P., Rambaux, N., Castillo-Rogez, J.C., Dehant, V., & Marty, J.C. (2013). Phobos interior from librations determination using Doppler and star tracker measurements. *Planetary and Space Science, 85,* 106-122. https://doi.org/10.1016/j.pss.2013.06.015

Marinova, M.M., Aharonson, O., & Asphaug, E. (2008). Mega-impact formation of the Mars hemispheric dichotomy. *Nature, 453*(7199), 1216-1219. https://doi.org/10.1038/nature07070

Mignard, F. (1981). Evolution of the Martian satellites. *Monthly Notices of the Royal Astronomical Society, 194*, 365–379. https://doi.org/10.1093/mnras/194.2.365

Murchie, S.L., Britt, D.T., Head, J.W., Pratt, S.F., Fisher, P.C., Zhukov, B.S., … Robinson, M.S. (1991). Color heterogeneity of the surface of Phobos: Relationships of geological features and comparison to meteorite analogs. *Journal of Geophysical Research, 96,* 5925–5945. https://doi.org/10.1029/90JB02354

Murchie, S., & Erard, S. (1996). Spectral properties and heterogeneity of Phobos from measurements by Phobos 2. *Icarus*, *123*(1)*,* 63–86. https://doi.org/10.1006/icar/1996.0142

Murchie, S.L., Britt, D.T., & Pieters, C.M. (2014). The value of Phobos sample return. *Planetary and Space Science*, *102,* 176-182. https://doi.org/10.1016/j.pss.2014.04.014

Murray, C.D., & Dermott, S.F. (1999). Solar system dynamics. Cambridge Press University.

Moroz, L.V., Hiroi, T., Shingareva, T.V., Basilevsky, A.T., Fisenko, A.V., Semjonova, L.F., & Pieters, C.M. (2004). Reflectance spectra of CM2 chondrite Mighei irradiated with pulsed LASER and implications for low-albedo asteroids and Martian moons. Lunar Planetary Science Conference XXXV, 1279 (abstract)

Nakajima, M. & Canup, R.M. (2017). Origin of the Martian Moons and Their Volatile Abundances. *American Geophysical Union Fall Meeting, 2017,* abstract #P54B-05.

Paetzold, M., Andert, A., Jacobson, R., Rosenblatt, P., Dehant, V. (2014). Phobos: Observed bulk properties. *Planetary and Space Science*, *102,* 86-94. http://dx.doi.org/10.1016/j.pss.2014.01.004

Pajola, M., Lazzarin, M., Bertini, I., Marzari, F., Turrini, D., Magrin, S., … Sierks, H. (2012). Spectrophotometric investigation of Phobos with the Rosetta OSIRIS-NAC camera and implications for its collisional capture. *Monthly Notices of the royal Astronomical Society, 427*(4), 3230-3243. https://doi.org/10.1111/j.1365-2966.2012.22026.x

Pajola, M., Lazzarin, M., Dalle Ore, C.M., Cruikshank, D.P., Roush, T.L., Magrin S., … Barbieri, C. (2013). Phobos as a D-type captured asteroid, spectral modeling from 0.25 to 4.0 microns. *The Astrophysical Journal, 777,* https://doi.org/10.1088/0004-637X/777/2/127

Pang, K.D., Pollack, J.B., Veverka, J., Lane, A.L., Ajello, J.M. (1978). The composition of Phobos—evidence for carbonaceous chondrite surface from spectral analysis. *Science*, *199,* 64–66. https://doi.org/ 10.1126/science.199.4324.64

Pascu, D., Erard, S., Thuillot, W., & Lainey V. (2014). History of telescopic observations of the Martian satellites. *Planetary and Space Science*, *102,* 2-8. http://dx.doi.org/10.1016/j.pss.2013.07.006

Peale, S.J., & Canup, R.M. (2015). The origin of the natural satellites. In G. Schubert, & T. Spohn (Eds.), Treatise on geophysics: Second Edition, Volume 10, (pp 559-604). Elsevier B.V.

Polishook, D., Jacobson, S.A., Morbidelli, A., & Aharonson, O. (2017). A Martian origin for the Mars Trojan asteroids. *Nature Astronomy, 1*. https://doi.org/10.1038/s41550-017-0179

Pieters, C.M., Murchie, S., Thomas, N., & Britt, D. (2014). Composition of surface materials on the moons of Mars. *Planetary and Space Science*, *102,* 144-151. http://dx.doi.org/10.1016/j.pss.2014.02.008

Pignatale, F.C., Charnoz, S., Rosenblatt, P., Hyodo, R., Nakamura, T., & Genda, H. (2018). On the Impact Origin of Phobos and Deimos. III. Resulting Composition from Different Impactors. *The Astrophysical Journal, 853*(2). https://doi.org/10.3847/1538-4357/aaa23e

Pollack, J.B., Veverka, J., Pang, K.D., Colburn, D.S., Lane, A.L., Ajello, J.M. (1978). Multicolor observations of Phobos with the Viking lander cameras—evidence for a carbonaceous chondritic composition. *Science*, *199,* 66–69. https://doi.org/ 10.1126/science.199.4324.66

Rivkin, A.S., Brown, R.H., Trilling, D.E., Bell, J.F. III, & Plassman, J.H. (2002). Near-Infrared spectrophotometry of Phobos and Deimos. *Icarus 156*(1), 64-75. https://doi.org/10.1006/icar.2001.6767

Ronnet, T., Vernazza, P., Mousis, O., Brugger, B., Beck, P., Devouard, B., … Cipriani, F. (2016). Reconciling the Orbital and Physical Properties of the Martian Moons. *The Astrophysical Journal, 828*(2). https://doi.org/10.3847/0004-637X/828/2/109

Rosenblatt, P. (2011). The origin of the Martian moons revisited. *The Astronomy and Astrophysics Review*, *19*(1), 1-26. https://doi.org/10.1007/s00159-011-0044-6

Rosenblatt, P., & Charnoz, S. (2012). On the formation of the martian moons from a circum-martian accretion disk. *Icarus 221*(2), 806-815. https://doi.org/10.1016/j.icarus.2012.09.009

Rosenblatt, P., & Pinier, B. (2014). Phobos' origin: Revisiting the capture scenario. Tidal evolution of the post-capture orbit. 5th Moscow Solar System Symposium.

Rosenblatt, P., Charnoz, S., Dunseath, K.M., Terao-Dunseath, M., Trinh, A. Hyodo, R., … Toupin, S. (2016). Accretion of Phobos and Deimos in an extended debris disc stirred by transient moons. *Nature Geoscience, 9*(8), 581-583. https://doi.org/10.1038/ngeo2742

Roush, T.L., & Hogan, R.C. (2000). Mars global surveyor thermal emission spectrometer observations of Phobos. Lunar Planet Sci XXXII, 1598 (abstract)

Salmon, J., Charnoz, S., Crida, A., & Brahic, A. (2010). Long-term and large-scale viscous evolution of dense planetary rings. *Icarus 209*(2), 771-785. https://doi.org/10.1016/j.icarus.2010.05.030

Samuel H., Lognonné P., Panning M., Lainey V., 2019. The rheology and thermal history of Mars revealed by the orbital evolution of Phobos. Nature 569, 523-527.

Sasaki, S. (1990). Origin of Phobos—aerodynamic drag capture by the primary atmosphere of Mars. Lunar Planet Sci XXI:1069–1070 (abstract)

Schultz, P.H., & Lutz-Garihan, A.B. (1982). Grazing impacts on Mars - A record of lost satellites. In: Lunar and Planetary Science Conference, 13th, *Proceedings. Part 1. (A 83-15326 04-91),* A84–A96. https://doi.org/10.1029/JB087iS01p00A84

Sharpless, B.P. (1945). Secular accelerations in the longitudes of the satellites of Mars. *Astronomical Journal*, *51,* 185-186. https://doi.org/10.1086/105871

Schmedemann, N., Michael, G.G., Ivanov, B.A., Murray, J.B., & Neukum, G. (2014). The age of Phobos and its largest crater, Stickney. *Planetary and Space Science*, *102,* 152-163. http://dx.doi.org/10.1016/j.pss.2014.04.009

Singer, S.F. (2003). Origin of the Martian satellites Phobos and Deimos. In: Workhop on the exploration of Phobos and Deimos, p 7020 (abstract)

Szeto, A.M.K. (1983). Orbital evolution and origin of the Martian satellites. *Icarus 55*, 133–168. https://doi.org/10.1016/0019-1035(83)90056-8

Thomas, P.C. (1993). Gravity, tides, and topography on small satellites and asteroids - Application to surface features of the Martian satellites, *Icarus*, *105,* 326-344. https://doi.org/ 10.1006/icar.1993.1130

Thomas, N., Stelter, R., Ivanov, A., Bridges, N.T., Herkenhoff, K.E., & McEwen, A.S. (2011). Spectral heterogeneity on Phobos and Deimos: HiRiSE observations and comparisons to Mars pathfinder results. *Planetary and Space Science, 59*(13), 1281-1292. https://doi.org/10.1016/j.pss.2010.04.018

Touma, J., & Wisdom, J. (1993). The chaotic obliquity of Mars. *Science 259*(5099), 1294-1297. https://doi.org/10.1126/science.259.5099.1294

Usui T., Bajo K.-I., Fujiya W., Furukawa Y., Koike M., Miura Y.N., Sugahara H., Tachibana S., Takano Y., Kuramoto K., 2020. The importance of Phobos sample return for understanding the Mars-moon system. Space Science Reviews 216 (4), doi:10.1007/s11214-020-00668-9.

Vernazza, P., Cipriani, F., Dukes, C., Fulvio, D., Howard, K.T., Witasse, O., … Bland, P.A. (2010). Origin of the Martian moons: Investigating their surface composition. In EPSC, Vol 5, EPSC2010-262 (abstract).

Visscher, C., & Fegley B. Jr. (2013). Chemistry of Impact-generated Silicate Melt-vapor Debris Disks. *The Astrophysical Journal Letters, 767*(1). https://doi.org/10.1088/2041-8205/767/1/L12

Wilhelms, D.E., & Squyres, S.W. (1983). The martian hemispheric dichotomy may be due to a giant impact. *Nature, 309,* 138-140. https://doi.org/10.1038/309138a0

Willner, K., Shi, X., & Oberst, J. (2014). Phobos' shape and topography models. *Planetary and Space Science*, *102,* 51-59. http://dx.doi.org/10.1016/j.pss.2013.12.006

Witasse, O., Duxbury, T., Chicarro, A., Altobelli, N., Andert, T., Aronica, A., … Zegers, T. (2014). Mars Express investigations of Phobos and Deimos. *Planetary and Space Science*, *102,* 18-34. http://dx.doi.org/10.1016/j.pss.2013.08.002

Yamamoto S., Watanabe, S., & Matsunaga, T. (2018). Space-Weathered Anorthosite as Spectral D-Type Material on the Martian Satellites. *Geophysical Research Letters, 45*(3), 1305-1312. https://doi.org/10.1002/2017GL076612

Yoder, C.F. (1982). Tidal rigidity of Phobos. *Icarus 49*, 327–346. https://doi.org/10.1016/0019-1035(82)90040-9

Yokoyama, T. (2002). Possible effects of secular resonances in Phobos and Triton. *Planetary and Space Science 50*(1), 63-77. https://doi.org/10.1016/S0032-0633(01)00078-2

Zanotto E.D., Mauro J.C., 2017. The glassy state of matter: Its definition and ultimate fate. Journal of non-crystalline solids, 471, 490-495.

Afterword

In my research work, I have studied different topics and used different approaches. My education and training were not focused on any of these topics, but was not focused on any of these topics, but it gave me a strong basis in fundamental and applied physics. It helped me to understand and apply various (and sometimes complex) principles, methods and techniques used in modeling as well as observations of the solar system bodies. My training also gave me different views of the problems and issues concerning the solar system. I took care to keep an original approach to explore innovating paths of research.

This long research work allowed me to meet many people from different scientific domains, countries, cultures and ways of life. It is certainly from these meetings that I learned the most on how scientific thinking is developed. From this point of view, exploring the solar system is particularly challenging because even after more than 50 years of space exploration, any new mission always requires us to reconstruct our models and sometimes to revisit our fundamental knowledge. These long exchanges with so many different people convinced me, if that were necessary, that research is first a team-spirit work. This is definitively how I see research: an adventure just as human as it is scientific.

Today, more and more space agencies incorporate space exploration of our solar system in their national programs, promising new exciting discoveries and meetings.

To be continued …

3 Curriculum Vitae détaillé (au 19 juin 2020)

3.1 Position et responsabilité actuelles

Chercheur contractuel au laboratoire de Planétologie et Géodynamique (UMR-6112) situé sur le campus de l'Université de Nantes. Co-PI de l'expérience de radio-science sur la mission EnVision, candidate finaliste au call M5 du programme *cosmic vision* de l'ESA. Dans le cadre des études de phase-A, je participe à l'élaboration, pour l'expérience de radio-science, des documents nécessaires au processus de sélection. En tant qu'expert en géodésie planétaire, je suis également en charge des simulations de la détermination du champ de gravité de Vénus par les futures données de poursuite de la sonde EnVision en orbite autour de la planète. Pour mener à bien ces simulations j'utilise le logiciel GINS (Géodésie par intégration Numérique Simultanée) développé par le CNES. Je contribue à développer ce logiciel pour les applications planétaires en l'éprouvant sur des cas réels dans le cadre de mes responsabilités internationales dans les missions ExoMars2016 (TGO) de l'ESA, en tant que *Guest Investigator*, et MAVEN de la NASA, en tant que *Participating Scientist*.

3.2 Expérience d'encadrement

3.2.1 Stagiaire (Licence, M1, et M2)

2014-2015: Stage de +Césure, Aurélien Ancelin-Binet. *Etude de la formation des satellites de Mars par accrétion. Développement d'un simulateur N-corps.* Université de Rennes-1, Observatoire royal de Belgique.

2014 : Stage de Master-1, Loïc Strafella. *Intégration du mouvement d'un satellite naturel dans une nébuleuse planétaire.* Université de Rennes-1.

2014 : Stage de Master-2, Benoît Pinier. *Evolutions à long terme de l'orbite des lunes de Mars, Phobos et Deimos: Implications sur leur origine.* Université de Rennes-1, Observatoire royal de Belgique.

2012 : Stage Ecole d'ingénieur 1ère année, Giovanni Mion. *Simulation numérique du processus d'accrétion dans un disque de débris autour de Mars.* Ecole d'ingénieur Denis Diderot, Université Paris-7 Diderot, Observatoire royal de Belgique.

2011 : Stage de Master-2, Stéven Toupin. *Intégration numérique des équations de Lagrange et de Gauss pour le mouvement d'un satellite artificiel.* Université de Rennes-1, Observatoire royal de Belgique.

2009 : Stage de Master-2, Guillaume Lion. *Dynamique des orbites excentriques autour de Mars: Spectre des perturbations gravitationnelles et analyse de sensibilité de l'orbite.* Université de Paris-Sud 11.

2007 : Stage de Master-2, Ngoc-Tuyen Cao. *Etude de la structure interne de Phobos.* Université de Nantes, Observatoire royal de Belgique.

2007 : Stage de Master-2, Rose-Marie Baland. *Structure interne d'Europe à partir des mesures de poursuite Doppler d'un orbiteur.* Université Catholique de Louvain, Observatoire royal de Belgique.

2006 : Stage de licence, Antony Trinh. *Etude de faisabilité concernant l'utilisation de mesures altimétriques (MOLA) de la sonde Mars Global surveyor pour la détection des nutations de Mars.* Université Catholique de Louvain, Observatoire royal de Belgique.

2006 : Stage d'école d'ingénieur 2ème année, Jonathan Renault. *Simulations numériques de mesures LASER de distance entre la Terre et une sonde en orbite autour de Mars. Amélioration de la détermination du champ de gravité de la planète.* Ecole Nationale des Sciences Géographiques, Observatoire royal de Belgique.

2005 : Stage de DEA, Jordi Fondecaba i Baig. *Etude de la fonction de mesure de Mars Express et applications au calcul des variations temporelles du champ de gravité martien.* Observatoire de Paris, Université Notre Dame de la Paix Namur, Observatoire royal de Belgique.

3.2.2 Doctorant

- 2010-2013: Sébastien Le Maistre. *The rotation of Mars and Phobos from Earth-based radio-tracking observations of a lander.* Université Catholique de Louvain.

Encadrant : Véronique Dehant (ROB, Belgium)

Publications communes : Ce travail de thèse a donné lieu à trois publications communes dans des revues de rang A à comité de lecture [PR16], [PR22] et [PR26].

Taux d'encadrement : 50%

Devenir du candidat du Docteur: Après sa these, S. Le Maistre a effectué 2.5 years de PostDoc au JPL-NASA (California, USA). Il est ensuite revenu à l'ORB où il est à ce jour contractuel de recherche.

Résumé de la thèse: The knowledge of the interior structure of terrestrial planets is fundamental to our understanding of the Solar system and for our comprehension of the formation and evolution of those planets. The study of the rotation variations allows to explore such otherwise difficult to obtain global properties of those planets. Deep space missions involving landers are the most suitable ones to study the rotation of their host. Firstly, numerical simulations have been realized to assess the precision that can be obtained in the determination of the rotation parameters of Mars from Direct-To-Earth (DTE) Doppler data. Among other things, these simulations provided the precision and the accuracy that can be inferred on the physical properties of the liquid core of Mars

(size, moments of inertia and dynamical flattening) from future Mars nutation measurements. In the same way, the precision that can be achieved on the Phobos libration estimates has been predicted still using DTE Doppler data from a lander.
Secondly, we have analyzed Viking Lander 1, Pathfinder Spirit and Opportunity real Doppler data. From this dataset, we have estimated new Mars rotation parameters including a new precession rate solution appreciably smaller than the current one. The liquid core contribution to nutation has likely been observed, but the large error bars in the nutation parameter estimates prevent to constrain Mars interior models.

- 2002-2005: Julien Duron. *De la dynamique d'un satellite en orbite autour de Mars : Applications aux missions de radio science Mars Global Surveyor, Odyssey, Mars Express et NetLander.* Université Catholique de Louvain.

Encadrant : Véronique Dehant (ROB, Belgium)

Publications communes : Ce travail de thèse a donné lieu à deux publications dans des revues de rang A à comité de lecture [PR4] et [PR12].

Taux d'encadrement : 50%

Devenir du Docteur: Après sa thèse, Julien Duron a travaillé pour des entreprises privées de sous-traitance dans le domaine du spatial. Il est actuellement employé à Telespazio en tant que 'project manager' sur le contrôle d'orbite des satellites artificiels de la Terre.

Résumé de la thèse: Mars est entourée d'une atmosphère ténue, composée à 95% de dioxyde de carbone (CO_2). Au cours d'une année martienne, des transferts de masse (jusqu'à 30% du CO_2 atmosphérique) entre l'atmosphère et les calottes polaires produisent des variations temporelles à très grande longueur d'onde du champ de gravité, notamment des harmoniques zonaux de son développement en harmoniques sphériques (de fait les coefficients "composites" de degré 2 et 3). D'un autre côté, le potentiel gravitationnel du Soleil induit des déformations, dites de marée, du volume martien. Ces déformations produisent un potentiel perturbateur en tout point extérieur à la planète, proportionnel à son nombre de Love de degré 2 k_2. k_2 traduit la réponse élastique de la planète au potentiel solaire et permet de caractériser physiquement le noyau de Mars (sa nature, solide ou liquide, et son rayon). Une manière de quantifier les transferts de la masse atmosphérique et l'état du noyau est de déterminer les perturbations inhérentes sur le mouvement d'un satellite artificiel. Le cycle saisonnier du CO_2 et l'état du noyau impliquent aussi des variations de la rotation de Mars. Une autre manière de quantifier les transferts de la masse atmosphérique et l'état du noyau est donc d'observer leurs effets sur la rotation. Des simulations d'observations de trajectographie de satellites (comme celles de Mars Global Surveyor, MGS, Odyssey, MODY) et/ou de la position d'un réseau de stations à la surface de Mars (comme dans l'expérience NEIGE) nous ont permis de voir s'il est possible de restituer précisément les variations des harmoniques zonaux de gravité de bas degré et/ou la rotation. Avec les observations réelles de trajectographie des missions américaines MGS et MODY, on a restitué les variations des harmoniques zonaux de gravité de bas degré et k2.

3.2.3 Post-doctorant

- 2011-2014: Maria Kudryashova. Radio-science workpackage (WP2) of the European Satellite Partnership for Computing Ephemerides (ESpACE).

Publication commune : Ce travail a donné lieu à la publication d'un proceeding [P14] et à des communications dans des congrès internationaux.

- 2010-2011: Séverine Rosat. Mars and Mercury rotation variations from altimetry crossover data: Feasibility study. Observatoire royal de Belgique.

Publication commune : Ce travail a donné lieu à une publication dans une revue de rang A à comité de lecture [PR9] ainsi qu'à des communications dans des congrès internationaux.

Devenir du Post-Doctorant : Séverine Rosat est chargée de recherche au CNRS depuis 2011.

3.2.4 Participation à des jurys de thèse et de stage

2012 - 2017: Membre du comité d'encadrement de la thèse d'Alexis Coyette: *Variations de la rotation et structure interne des satellites de glace du système solaire.* Université Catholique de Louvain, Observatoire royal de Belgique.

2013 : Rapporteur de la thèse de Guillaume Lion: *Dynamique des orbites fortement elliptiques.* Observatoire de Paris, Institut de Mécanique Céleste et de Calcul des Ephémérides.

2012 : Rapporteur de la thèse d'Olivia Golle: *Convection mantellique, topographie et géoïde sur Mars et Vénus".* Université de Nantes, Laboratoire de Planétologie et Géodynamique.

2011 : Rapporteur de la thèse de Laurène Beauvalet: *Etude dynamique des systèmes multiples de petits corps. Application au système de Pluton.* Observatoire de Paris, Institut de Mécanique Céleste et de Calcul des Ephémérides.

2011 : Lecteur du mémoire d'Alexis Coyette: *Calcul des modes de Slichter de Mercure.* Université Catholique de Louvain, Observatoire royal de Belgique.

2009 : Rapporteur de la thèse de Josselin Desmars: *Précision d'extrapolation des éphémérides des objets du système solaire. Application aux satellites de Saturne.* Observatoire de Paris, Institut de Mécanique Céleste et de Calcul des Ephémérides.

3.3 Expérience de recherche

3.3.1 Participation à des propositions de missions spatiales

3.3.1.1 Proposition en cours de sélection

Oct. 2016: Co-*Principal Investigator (Co-PI)* de l'expérience de radio-science dans la proposition de mission EnVision soumise en réponse à l'appel d'offre *Medium-Class mission call#5* du *Cosmic Vision Program* de l'ESA.

Etude de phase-A (Juin 2018 – Juin 2021).

3.3.1.2 Proposition sélectionnée

Oct. 2014: *Collaborator* de la proposition *"Analysis of Magellan and Venus Express satellite tracking data for high-resolution gravity field determination"* soumise au programme *Planetary Missions Data Analysis Program (PMDAP)* de la NASA.

Juin 2013: *Participating Scientist* sur la mission MAVEN de la NASA. Projet MAGE (Maven Atmospheric and Gravity Experiment).

Nov. 2011: Proposition d'une expérience de radio-science visant à déterminer le champ de gravité et l'amplitude de libration de Phobos en utilisant les données de poursuite de la sonde PHOBOS-GRUNT de l'agence spatiale russe Roscosmos.

3.3.1.3 Proposition non sélectionnée

Mar. 2017: *Coordinator* de la proposition COMPARE (Combining Observations and Modeling to Promote upper Atmosphere Research and Exploitation) soumise à l'appel d'offre COMPET-4 du programme H2020 de la commission Européenne.

Oct. 2016: *Team Core Member* de la proposition DePhine soumise en réponse à l'appel d'offre *Medium-Class mission call#5* du *Cosmic Vision Program* de l'ESA.

Fév. 2015: *Co-Investigator (Co-I)* sur la proposition PADME soumise à l'appel d'offre du programme *Discovery* de la NASA. Détermination et modélisation de la structure interne de Phobos.

Jan. 2015: *Team leader* pour l'expérience de radio-science sur la partie atterrisseur de la proposition PHODEX soumise en réponse à l'appel d'offre *Medium-Class mission call#4* du *Cosmic Vision Program* de l'ESA.

Jan. 2015: Participation (Champ de gravité) à la proposition EnVision soumise en

réponse à l'appel d'offre *Medium-Class mission call#4* du *Cosmic Vision Program* de l'ESA.

Jan. 2015: *Instrument leader (radio-science)* sur la proposition NAUTILUS soumise en réponse à l'appel d'offre *Medium-Class mission call#4* du *Cosmic Vision Program* de l'ESA.

Nov. 2012: Proposition du transponder LaRa à l'appel d'offre à instrument pour la mission candidate MarcoPolo-R pour répondre à l'appel d'offre *Medium-Class mission call#3* du *Cosmic Vision Program* de l'ESA. PI de l'expérience de radio-science utilisant ce transponder.

Déc. 2010: Membre du *core Team* de la proposition de mission GETEMME (Gravity Field Studies, Tests of Einstein's Theory, and Exploration of the Martian Moons' Environment, soumise en réponse au *Medium-Class mission call#3* du *Cosmic Vision Program* de l'ESA.

Déc. 2010: *Co-investigator (Co-I)* de la proposition de mission EVE (European Venus Explorer), soumise en réponse au *Medium-Class mission call#3* du *Cosmic Vision Program* de l'ESA.

Juin 2009: *Co-investigator (Co-I)* de la proposition de mission *ODYSSEUS* soumise au *new frontiers program* de la NASA.

3.3.2 Responsabilités internationales

Depuis 2017: *Co-investigator* (Co-I) sur l'expérience NOMAD à bord de l'orbiteur ExoMars2016 (TGO, *Trace Gas Orbiter*) de l'ESA.

Depuis 2016: *Guest Investigator* (GI) sur la mission de l'ESA ExoMars2016 (orbiteur TGO, *Trace Gas Orbiter*).

Depuis 2015: Membre de la *Study Science Team* de la mission candidate *Phobos Sample Return (PhSR)* de l'ESA.

2015-2016: *Co-investigator* (Co-I) sur l'expérience de radio-science *LaRa* (Lander Radioscience) embarquée à bord de la plateforme russe, composante de la mission ExoMars 2018 de l'Agence Spatiale européenne et de l'agence spatiale russe (Roscosmos).

2015-2016: Membre du *Advisory Team* de la mission candidate AIDA (Asteroid Impact & Deflection Assessement). Expertise dans l'expérience de radio-science (champ de gravité et structure interne du système d'astéroides binaires Dydimos cible de la mission).

Depuis 2014: *Collaborateur* au projet "Analysis of Magellan and Venus Express satellite tracking data for high-resolution gravity field determination" du programme Planetary Mission Data Analysis Program (PMDAP) de la NASA.

Depuis 2013: *Co-Investigator (Co-I)* sur l'expérience PRIDE (Planetary Radio Interferometry and Doppler Experiment) embarquée sur la mission de classe L1 JUICE (JUpiter ICy moons Explorer) de l'ESA

Depuis 2013: *Participating Scientist* (PS) à la mission MAVEN (Mars Atmosphere and Volatile EvolutioN) de la NASA. Projet de recherche MAGE (Maven Atmosphere and Gravity Experiment): Mesure de la densité de la thermosphère et amélioration du champ de gravité de Mars à partir des données de poursuites de l'orbiteur MAVEN.

Depuis 2013: *Principal Investigator (PI)* de l'expérience GR035 utilisant les données PRIDE (Planetary Radio Interferometry and Doppler Experiment) effectuée lors du survol rapproché de Phobos par la sonde Mars Express de l'ESA en décembre 2013.

2012-2015: Membre du *Planetary Science Archive Group (PSA-UG)* de l'agence spatiale européenne (ESA).

2011-2015: Responsable du *workpackage radio-science (WP2)* du projet européen FP7 ESPaCE (*European Satellite Partnership for Computing Ephemerides*).

2011 : *Co-Investigator* (Co-I) de l'expérience de radio-science de la mission Phobos-Soil de l'agence spatiale russe (Roscosmos).

Depuis 2008: *Co-Investigator* (Co-I) des expériences de radio-science à bord des missions Mars Express et Venus Express de l'agence spatiale Européenne (ESA).

3.3.3 Responsabilités nationales

2010-2017: Membre du comité national belge de géodésie et géophysique.

1992-1997: Participation à des programmes de recherche Français: 1992-1997 Programme Dynamique et Bilan de la Terre II - Terre profonde. 1994 Programme IDYL - Structure globale de la lithosphère et interactions Lithosphère/Asthénosphère/Panaches.

3.3.4 Organisation de symposium, convener de session.

Juillet 2016: Membre du *Scientific Organizing Committee of the 3rd international conference on the exploration of Phobos and Deimos.* NASA-AMES, Moffet field, CA, USA.

Juin 2012: Membre du *Scientific Organizing Committee of the 46th ESLAB symposium "Formation and evolution of moons".* ESTEC/ESA, Noordwijk, The Netherlands.

Mai 2009: Co-organisateur de la session *Interior and subsurface of the international conference on comparative planetology: Venus-Earth-Mars,* ESTEC/ESA, Noordwijk, The Netherlands.

Déc. 2004: Co-convener (avec F. Lemoine, *Goddard space flight center*) de la session *"Geodesy, Gravity Field and Dynamics of Telluric Planets" of the American Geophysical Union meeting*. San Francisco, CA, USA.

3.3.5 Stage, post-doctorat, contrats

Sep. 2019-Aug. 2020: Chercheur au laboratoire de Planétologie et Géodynamique. Co-PI de l'expérience de radio-science à bord de la mission EnVision candidate au call M5 du programme *cosmic vision* de l'ESA. Responsable de l'étude de phase-A sur l'amélioration du champ de gravité de Vénus à partir des données de poursuite de la sonde en orbite autour de Vénus.

Mai 2019-Jul. 2019: Ingénieur de recherche au Laboratoire de Planétologie et Géodynamique. Pré-étude de faisabilité d'une expérience de gravité à bord de la mission EnVision candidate au call M5 du programme *cosmic vision* de l'ESA

Nov. 2001-Sep. 2017: Chercheur à l'observatoire royal de Belgique. Responsable de l'analyse et de l'interprétation scientifique des données de poursuite radio des atterrisseurs et orbiteurs planétaires.

Fev.-Oct. 2001: Chercheur au Laboratoire d'Etudes Geophysique et Océanographique spatiales (LEGOS, Toulouse, France). Simulations numériques d'orbites de satellites artificiels de la Terre pour améliorer le système de positionnement DORIS du CNES.

Oct. 1995-Sep.1998: Post-doctorat au laboratoire de dynamique terrestre et planétaire (DTP/CNRS, Toulouse, France). Sujet de recherche: Analyse quantitative des données radar (altimétrie et imagerie SAR) et des données de gravité de la sonde Américaine *Magellan* en orbite autour de Vénus. Interprétation de l'histoire géologique régionale et locale de la planète - Structure thermique et mécanique de sa lithosphère.
Séjour d'Octobre à Décembre 1996 et en mars 1997 à Brown University (Prof. James Head) pour l'analyse des images radar.

Mar-Jul 1990: Stage de DEA: Détermination de l'orbite de satellite artificiel de la Terre à partir de données de poursuite optique (Alcatel Espace, Toulouse, France).

Fev.-Sept. 1989: Stage à l'Observatoire Midi-Pyrénées. Observation et analyse des images CCD de galaxies allongées.

3.4 Collaborations

3.4.1 Laboratoires d'accueil

Ma première collaboration fut avec des astronomes de l'Observatoire Midi-Pyrénées lors de mon stage d'initiation à la recherche (Février-Septembre 1989). Cette collaboration a abouti à un article de rang A dont j'ai été co-auteur [PR1]. J'ai ensuite collaboré avec des chercheurs du laboratoire de Dynamique Terrestre et Planétaire où j'ai effectué ma thèse et mon post-doctorat ainsi qu'avec des ingénieurs du CNES, menant à deux publications de rang A [PR2] et [PR3] et à plusieurs proceedings [P1], [P2] et [P3] et à de nombreuses communications dans des congrès internationaux et nationaux.
De 2001 à 2017, j'ai développé mes recherches en géodésie planétaire au sein de l'équipe de planétologie de l'observatoire royal de Belgique. Une série d'article sur l'analyse et l'interprétation des mesures de poursuite des sondes planétaires ont été publiés dans des journaux de rang A à comité de lecture [PR7], [PR10], et [PR12] ainsi qu'à des proceedings [P10] et [P11] et à de très nombreuses communications. Cette collaboration a aussi conduit à des articles de rang A sur des simulations de futures missions [PR4], [PR5], [PR6], [PR9], [PR11], [PR16], [PR22] et [PR26] ainsi qu'à des proceedings [P4], [P5], [P6] et à des communications. J'ai également participé à des publications sur des aspects plus théoriques de la modélisation et de l'interprétation géophysique des données de poursuite ou encore sur la structure interne des corps du système solaire qui ont mené à des publications de rang A [PR8], [PR14], [PR15], [PR17], [PR21], et [PR25] ainsi qu'à des proceedings [P7], [P8] et [P9] et à des communications.

3.4.2 Nationales et internationales

Je collabore depuis plus récemment avec l'institut royale d'aéronomie spatiale sur l'interprétation conjointe des données de poursuite et des données d'occultation solaire réalisées par l'instrument belge SOIR qui a volé sur la mission européenne Venus Express. Ce travail a mené jusqu'à présent à des communications. Cette collaboration (Co-I ship) se poursuit avec la même équipe qui mène les investigations de leur instrument NOMAD sur TGO.

Mes collaborations internationales ont débuté dès mon post-doctorat avec un séjour à Brown University, RI, USA qui a donné lieu à des communications. A mon arrivée à l'observatoire royal de Belgique mes collaborations internationales se sont établies avec l'équipe de géodésie spatiale du CNES au travers du développement et de l'utilisation du logiciel d'orbitographie GINS. Cette collaboration continue depuis lors et a mené à des publications de rang A, à des proceedings et à des communications, aussi bien sur l'exploitation des données de poursuite des missions européennes (MEX, VEX) et américaines (MGS, ODY, MRO) que sur des simulations de missions candidates. Une collaboration supplémentaire sur des aspects théoriques de structure interne des planètes s'est aussi développée avec l'appui du laboratoire de Planétologie et de géodynamique de l'Université de Nantes (Prof. A. Mocquet).

Mes collaborations se sont étendues avec mes responsabilités internationales, en tant que Co-I, au sein des équipes de radio-science des missions MEX (Mars Express Radio-Science, MaRS) et VeX (Venus Express RAdio-science, VeRA). J'ai ainsi

participé à des publications de rang A [PR13], [PR27], [PR28] et [PR32], à un proceeding [P12] et à de nombreuses communications.

Je collabore également avec l'équipe du *JIVE-ERIC (Joint Institute for Vlbi in Europe)* pour l'exploitation des données de poursuite *PRIDE (Planetary Radio Interferometry and Doppler Experiment)* acquises avec les sondes européennes MEX et VEX. Cette collaboration récente a déjà donné lieu à une publication de rang A [PR33] et à un Co-I ship sur la mission JUICE de l'ESA.

Au fil des années, j'ai acquis une réputation internationale dans le domaine de la géodésie spatiale et j'ai ainsi été contacté à plusieurs reprises pour la partie radio-science de missions candidates au programme de l'ESA, de la NASA et de Roscosmos. Bien qu'aucune de ces missions n'aient été sélectionnée (ou ait échouée, Phobos GRUNT), ces collaborations ont mené à des publications de rang A [PR20], [PR23] et [PR31] et à des communications. J'ai été sélectionné comme *Participating Scientist* à la mission MAVEN de la NASA menant jusqu'à présent à une publication de rang A [PR29]. J'ai activement collaboré au projet européen ESPaCE menant à des proceedings [P13], [P14] et [P15].

Ces collaborations m'ont donné l'envie de fédérer des ressources pluri-disciplinaires afin d'ouvrir de nouvelles voies de recherche dans une problématique donnée. J'ai donc conçu un projet de recherche sur la question de l'origine des lunes de Mars en publiant un article de review dans une revue de rang A [PR18] et j'ai dirigé une équipe de chercheurs internationaux (Japon, France, Belgique) qui a produit une avancée marquante sur la question avec des publications de rang A [PR24], [PR34] , [PR36], [PR37], [PR41], [PR43] et [PR46] ainsi que des communications.

3.5 Récompense

2013: Prix Georges Van Der Linden de l'académie royale de Belgique.

3.6 Expérience d'enseignement

3.6.1 Cours universitaire et école d'été

2009-2015: Assistant professeur invité à l'Université Catholique de Louvain. Cours de "Géophysique interne: Application aux planètes et corps du système solaire" au niveau de Master-1. 15 heures par an.

Détail du cours:
Flux de chaleur de la Terre: Mesures et interprétations. Principes de Géologie et de Géophysique appliqués à Vénus. Géodésie planétaire: Données de poursuite Doppler de sondes et atterrisseurs dans le système solaire - Calcul précis d'orbite de sondes - Reconstruction du mouvement propre des corps du système solaire - Détermination du champ de gravité et de la densité de la thermosphère par freinage atmosphérique du mouvement des orbiteurs.

2016 : Enseignant à l'école d'été "Trajectoires planétaires et interplanétaires" organisée par le GRGS. Aussois, France, Septembre 2016.

Détail du cours: Mesures de poursuite interplanétaires - Analyse des orbites de sondes autour de Mars et de Vénus.

2013 : Enseignant au workshop: Planet Mars 4. Les Houches, France. Octobre 2013.

Détail du cours: The origin of the Martian moons.

2013 : Enseignant 3ème école d'été "Mars Advanced School in China" organisée par l'Agence Spatiale Européenne (ESA) et par le National Observatory Of China (NAOC). Pékin, Chine. Septembre 2013.

Détail du cours: Origin and dynamics of early solar system - The topography and the gravity of the terrestrial planets - Mars' geodesy and gravity - The Martian moons: Origin and fate.

3.6.2 Séminaires

Mai 2019: *"The formation of the Martian moons: Observation and model"*.
Seminar given at IPGP Paris, Université Denis Diderot, Paris, France.

Mai 2019: *"Spacecraft orbit reconstruction: A tool to probe planetary interior from space"*.
Seminar given at IPG Strasbourg, Strasbourg, France.

Dec. 2018: *"A giant collision to form Phobos and Deimos"*.
Seminar given at the GODDARD Space Flight Center, Greenbelt, MD, USA.

Nov. 2018: *"La mission EnVision"*.
Seminar given at Journée de l'OCA, Sofia-Antipolis, France.

Juin 2018: *"A giant collision scenario at the origin of the Martian moons"*.
Seminar given at IMCCE/Observatoire de Paris, Paris, France.

Mars 2018: *"A giant collision scenario to form Phobos and Deimos"*.
Seminar given at Université de Nice, Sophia-Antipolis, France.

Nov. 2017: *"Geodesy and ephemerides in the solar system: The role of VLBI"*.
Seminar given at Université de Bordeaux, Bordeaux, France.

Jan. 2017: *"Space geodesy in the solar system: State of the art and future ideas"*.
Seminar given at University of Bern, Bern, Switzerland.

Sep. 2016: *"The story of the moons of Mars"*. Seminar given at Université Libre de Bruxelles (ULB), Brussels, Belgium.

Juin 2016: *"Une nouvelle histoire des lunes de Mars"*. Seminar given at Laboratoire

de Planétologie et Géodynamique, Nantes University, Nantes, France.

Mai 2016: *"Expérience de géodésie dans le système solaire: Etat de l'art et futurs projets"*. Seminar given at SYRTE, Observatoire de Paris, Paris, France.

Déc. 2015: *"Spacecraft orbit reconstruction: A tool to probe planetary interior from space"*. Seminar given at IPG, Université Paris 7, Paris, France.

Nov. 2015: *"What can we say about the origin of the Martian moons (Phobos & Deimos)?"*. Seminar given at the NASA's GODDARD spaceflight center, Greenbelt, MD, USA.

Mars 2015: *"Precise orbit reconstruction of spacecraft from radio-tracking data: A tool to probe planetary interior and thermosphere"*. Seminar given at ESTEC/ESA, Noordwijk, The Netherlands.

Mars 2015: *"Precise orbit reconstruction of spacecraft from radio-tracking data: A tool to probe planetary interior"*. Seminar given at Laboratoire de Planétologie et Géodynamique, Nantes University, Nantes, France.

Déc. 2014: *"Probing Phobos' interior with a geodetic experiment"*. Seminar given at DLR, Berlin, Germany.

Oct. 2014: *"Quelques aspects de l'exploration du système solaire à l'observatoire royal de Belgique"*. Seminar given at Rennes University, Rennes, France.

Fév. 2014: *"VLBI for planetary research"*. Seminar given at JIVE, Dwingeloo, The Netherlands.

Déc. 2013: *"How did the Martian moons form?"*. Seminar given at the department of Physics and Astronomy, KU Leuven, Leuven, Belgium.

Avr. 2013: *"The Martian moons: Origin and fate"*. Seminar given at Brown University, Providence, RI, USA.

Fév. 2012: *"What can space geodesy tell us about Mars and its moons"*. Seminar given at the Earth and Life Institute (ELI), Université catholique de Louvain, Louvain-la-Neuve, Belgium.

Nov. 2008: *"Accurate spacecraft orbit to determine tides, rotation and gravity field of planets"*. Seminar given at Institut de Mécanique Céleste et de Calcul des Ephémérides (IMCCE) / SYRTE / Observatoire de Paris, Paris, France.

Mai 2008: *"Accurate spacecraft orbit to determine tides, rotation and gravity field of planets"*. Seminar given at Observatoire de la Côte d'Azur, Grasse, France.

3.6.3 Conférence grand public et interview aux medias

Juillet 2016: Interview à *Radio Première (RTBF)* sur l'origine des lunes de Mars.

Jan. 2015: *"Les lunes de Mars: Phobos et Deimos".* 24 heures Basiliennes d'Astronomie 2015, Baisieux, France.

Juin 2009: Interview à la télévision belge *RTL-TVI* au sujet de la mission LCROSS de la NASA.

Mai 2004: *"La planète Vénus".* Liége, Belgique.

Oct. 2003: *"Vénus".* Cercle Astronomique de Bruxelles, Bruxelles, Belgique.

Déc. 2003: *"Mars".* Cercle Astronomique de Bruxelles, Bruxelles, Belgique.

3.7 Autres expériences professionnelles

Oct. 2017-Mai 2018: Ingénieur dans la societé de service ACRI-ST.

Mar. 1999-Fév. 2000: Ingénieur dans la societé de service Noveltis.

Juin-Déc. 2000: Ingénieur au Bureau Gravimétrique International.

3.8 Formation

1991-1995: Thèse de doctorat, spécialité planétologie comparée: *Hypsométrie comparée Terre/Vénus: Implications sur la géodynamique et la structure convective du manteau de Vénus.* UPR234/GRGS/OMP, Université Paul Sabatier, Toulouse.

1989-1990: DEA d'Astrophysique, Géophysique et Techniques Spatiales, Université Paul Sabatier, Toulouse.

1984-1989: DEUG, licence et Maîtrise de Physique fondamentale et appliquée, Université Paul Sabatier, Toulouse.

4 Publications

4.1 Peer-Reviewed Publications

[PR46] **Rosenblatt, P.,** Hyodo, R., Pignatale, F., Trinh, A., Charnoz, S., Dunseath, K., Dunseath-Terao, M., & Genda, H.,
The formation of the Martian moons.
In *Oxford Research Encyclopedia of Planetary Science*. Oxford University Press. doi: http://dx.doi.org/10.1093/acrefore/9780190647926.013.24

[PR45] Bocanegra-Bahamon T.M., Molera Calves G., Gurvits L.I., Cimo G., Dirckx D. Duev D.A., Pogrebenko S.V., **Rosenblatt P.,** Limaye S., Cui L., Li P., Kondo T., Sekido M., Mikahailov A.G., Kharinov M.A., Ipatov A.V., Wang W., Zheng W., Ma M., Lovell J.E.J., McCallum J.N.,
Venus Express radio occultation observed by PRIDE.
Astronomy & Astrophysics, Vol. 624, id.A59, 14 pp., 2019.

[PR44] Le Maistre S., Rivoldini A., **Rosenblatt P.**
Signature of Phobos' interior structure in its gravity field and libration.
Icarus, vol. 321, p. 272-290, 2019.

[PR43] Hyodo R., Hidenori G., Charnoz S., Pignatale F.C., **Rosenblatt P.**
On the impact origin of Phobos and Deimos IV: Volatile depletion.
The Astrophysical Journal, Vol. 860, Issue 2, id.150, 10 pp., 2018.

[PR42] Le Maistre S., **Rosenblatt P.,** Dehant V., Marty J.C., Yseboodt M.
Mars rotation determination from a moving rover using Doppler tracking data: What could be done?
Planetary and Space Science, Vol. 159, p. 17-27, 2018.

[PR41] Pignatale F.C., Charnoz S., **Rosenblatt P.,** Hyodo R., Nakamura T., Hidenori G.
On the impact origin of Phobos and Deimos III: Resulting composition from different impactors.
The Astrophysical Journal, doi.org/10.3847/1538-4357/aaa23e, 853:118, 12 pp., 2018.

[PR40] Bocanegra-Bahamon T.M., Molera Calves G., Gurvits L.I., Duev D.A., Pogrebenko S.V., Cimo G., Dirckx D., **Rosenblatt P.**
Planetary Radio Interferometry and Doppler Experiment (PRIDE) Technique: a test case of the Mars Express Phobos fly-by: II. Doppler tracking: formulation of observed and computed values and noise budget.
Astronomy & Astrophysics, Vol. 609, id.A59, 11 pp., 2018.

[PR39] Bertone S., Le Poncin-Lafitte C., **Rosenblatt P.,** Lainey V., Marty J.C., Angonin M.C.
Impact analysis of the transponder time delay on radioscience observables.
Advances in Space Research, Vol. 61, Issue 1, p. 89-96, 2018.

[PR38] Oberst J., Wickhusen K., Willner K., Gwinner K., Spiridonova S., Kahle R., Caotes A., Herique A., Plettemeier D., Michelena-Diaz M., Zakharov A., Futaana Y. Paetzold M., **Rosenblatt P.,** Lawrence D.J., Lainey V., Gibbings A., Gerth I.
DePhine – The Deimos and Phobos Interior Explorer.
Advances in Space research, Vol. 62, Issue 8, pp. 2220-2238, 2018.

[PR37] Hyodo R., **Rosenblatt P.,** Genda H., Charnoz S.,
On the impact origin of Phobos and Deimos I: Thermodynamic and physical properties of the proto-Martian moons disk.
The Astrophysical Journal, doi.org/10.3847/1538-4357/aa81c4, 845:125, 8 pp., 2017.

[PR36] Hyodo R., Genda H., Charnoz S., **Rosenblatt P.,**
On the impact origin of Phobos and Deimos I: Thermodynamic and physical properties of the proto-Martian moons disk.
The Astrophysical Journal, doi.org/10.3847/1538-4357/aa81c4, 845:125, 8 pp., 2017.

[PR35] Dumoulin C., Tobie G., Verhoeven O., **Rosenblatt P.,** Rambaux N.,
Tidal constraints on the interior of Venus.
Journal of Geophysical Research: Planets; Vol. 122, issue 6, pp. 1338-1352, 2017.

[PR34] **Rosenblatt P.,** Charnoz S., Dunseath K.M., Terao-Dunseath M., Trinh A., Hyodo R., Genda H., Toupin S.
Accretion of Phobos and Deimos in an extended debris disc stirred by transient moons.
Nature Geoscience, DOI 10.1038/NGEO2742, 2016.

[PR33] Duev D.A., Pogrebenko S.V., Cimo G., Molera Calvés G., Bocanegra Bahamon T.M., Gurvits L.I., Kettenis M.M., Kania J., Tudose V., **Rosenblatt P.,** Marty J.C., Lainey V., de Vincente P., Quick J., Nickola M., Neidhardt A., Kronschnabl G., Plötz C., Haas R., Lindqvist M., Orlati A., Ipatov A.V., Kharinov M.A., Mikhailov A.G., Lovell J., McCallum J., Stevens J., Gulyaev S.A., Natush T., Weston S., Wang W., Xia B., Yang W., Long-Fei H., Kallunki J., Witasse O.
Planetary Radio Interferometry and Doppler Experiment (PRIDE) technique: A test case of the Mars Express Phobos flyby.
Astronomy & Astrophysics, DOI 10.1051/0004-6361/201628869, 2016.

[PR32] Pätzold M., Häusler B., Tyler G.L., Andert T., Asmar S.W., Bird M.K., Dehant V., Hinson D.P., **Rosenblatt P.,** Simpson R.A., Tellmann S., Withers P., Beuthe M., Efimov A.I., Hahn M., Kahan D., Le Maistre S., Oschlisniok J., Peter K., Remus S.
Mars Express 10 years at Mars: Observations by the Mars Express Radio Science Experiment (MaRS).
Planetary and Space Science, Vol. 127, pp. 44-90, 2016.

[PR31] Michel P., Cheng A., Küppers M., Pravec P., Blum J., Delbo M., Green S.F., **Rosenblatt P.,** Tsiganis K., Vincent J.B., Biele J., Ciarletti V., Hérique A., Ulamec S., Carnelli I., Galvez A., Benner L., Naidu S.P., Barnouin O.S., Richardson D.C., Rivkin A., Scheirich P., Moskovitz N., Thirouin A., Schwartz S.R., Campo Bagatin A., Yu Y.
Science case for the Asteroid Impact Mission (AIM): A component of the Asteroid Impact & Deflection Assessment (AIDA) mission.
Advances in Space Research, Vol. 57, Issue 12, pp. 2529-2547, 2016.

[PR30] Dehant V., Asael D., Baland R.M., Baludikay B.K., Beghin J., Belza J., Beuthe M., Breuer D., Chernonozhkin S., Claeys Ph., Cornet Y., Cornet L., Coyette A., Debaille V., Delvigne C., Deproost M.H., De Winter N., Duchemin C., El Atrassi F., François C., De Keyser J., Gillmann C., Gloesener E., Goderis S., Hidaka Y., Höning D., Huber M., Hublet G., Javaux E.J., Karatekin O., Kodolanyi J., Revilla L. Lobo, Maes L., Maggiolo R., Mattielli N., Maurice M., McKibbin S., Morschhauser A., Neumann W., Noack L., Pham L.B.S., Pittarello L., Plesa A.C., Rivoldini A., Robert S., **Rosenblatt P.,** Spohn T., Storme J.-Y., Tosi N., Trinh A., Valdes M., Vandaele A.C., Vanhaecke F., Van Hoolst T., Van Roosbroek N., Wilquet V., Yseboodt M.
PLANET TOPERS: Planets, Tracing the transfer, Origin, Preservation, and Evolution of their ReservoirS.
Origins of Life and Evolution of Biospheres, DOI 10.1007/s11084-016-9488-z, 2016.

[PR29] Grebowsky J., Fast K., Talaat E., Combi M., Crary F., England S., Ma Y., Mendillo M., **Rosenblatt P.,** Seki K., Stevens M., Withers P.
Science Enhancements by the MAVEN Participating Scientists.
Space Science Reviews, Vol. 195, issue 1-4, pp. 319-355, 2015.

[PR28] Witasse O., Duxbury T., Chicarro A., Altobelli N., Andert T., Aronica A., Barabash S., Bertaux J.-L., Bibring J.-P., Cardesin-Moinelo A., Cichetti A., Companys V., Dehant V., Denis M., Formasino V., Futaana Y., Giuranna M., Gondet B., Heather D., Hoffmann H., Holmström M., Manaud N., Martin P., Matz K.-D., Montmessin F., Morley T., Müller M., Neukum G., Oberst J., Orosei R., Pätzold M., Picardi G., Pischel R., Plaut J.-J., Reberac A., Pardo Voss P., Roatsch T., **Rosenblatt P.**, Remus S., Schmedemann N., Willner K., Zegers T.,
Mars Express investigations of Phobos and Deimos. Planetary and Space Science, Vol. 102, pp.18-34, 2014.

[PR27] Pätzold M., Andert T., Jacobson R., **Rosenblatt P.,** Dehant V.
Phobos: Observed bulk properties.
Planetary and Space Science, Vol. 102, pp. 86-94, 2014.

[PR26] Le Maistre S., **Rosenblatt P**., Rambaux N., Castillo-Rogez J.C., Dehant V., Marty J.C.
Phobos interior from librations determination using Doppler and star tracker measurements.
Planetary and Space Science, Vol. 85, p. 106-122, 2013.

[PR25] Rambaux N., Castillo-Rogez J.C., Le Maistre S., **Rosenblatt P.,**
Rotational motion of Phobos
Astronomy and Astrophysics, Vol. 548, id.A14, 11pp., doi:10.1051/0004-6361/201219710, 2012.

[PR24] **Rosenblatt P.** and Charnoz S.
On the formation of the Martian moons from a circum-martian accretion disk.
Icarus, Vol. 221, Issue 2, p. 806-815, 2012.

[PR23] Oberst J., Lainey V., Le Poncin-Lafitte C., Dehant V., **Rosenblatt P.,** Ulamec S., Biele J., Spurmann J., Kahle R., Klein V., Schreiber U., Schlicht A., Rambaux N., Laurent P., Noyelles B., Foulon B., Zakharov A., Gurvits L., Uchaev D., Murchie S., Reed C., Turyshev S.G., Gil J., Graziano M., Willner K., Wickhusen K., Pasewaldt A., Wählisch M., Hoffmann H.
GETEMME – a mission to explore the Martian satellites and the fundamentals of solar system physics.
Experimental Astronomy, DOI 10.1007/s10686-012-9307-0, 2012.

[PR22] Le Maistre S., **Rosenblatt P.**, Rivoldini A., Dehant V., Marty J.C., Karatekin Ö.
Lander radio science experiment with a direct link between Mars and the Earth.
Planetary and Space Science, Vol. 68, Issue 1, p. 105-122, 2012.

[PR21] Beuthe M., Le Maistre S., **Rosenblatt P.**, Pätzold M., Dehant V.,
Density and lithospheric thickness of the Tharsis province from MEX MaRS and MRO gravity data.
Journal of Geophysical Research, Vol. 117, Issue E4, doi:10.1029/2011JE003976, 2012.

[PR20] Lamy P., Vernazza P., Poncy J., Martinot V., Hinglais E., Canalias E., Bell J., Cruikshank D., Groussin O., Helbert J., Marzari F., Morbidelli A., **Rosenblatt P.**, Sierks H.
Trojans' Odyssey: Unveiling the early history of the Solar system.
Experimental Astronomy, Vol. 33, Issue 2-3, p. 685-721, 2012.

[PR19] **Rosenblatt P.,** Bruinsma S.L., Müller-Wodarg I.C.F., Häusler B., Svedhem H., Marty J.C.
First ever in situ observations of Venus' polar upper atmosphere density using the tracking data of the Venus Express Atmospheric Drag Experiment (VExADE).
Icarus, Special issue: "Advances in Venus science", Vol. 217, No 2, p. 831-838, 2012.

[PR18] **Rosenblatt P.**
The origin of the Martian moons revisited.

Astronomy and Astrophysics Review, Vol. 19, No 1, p. 19-44, doi:10.1007/s00159-011-0044-6, 2011.

[PR17] Mocquet A., **Rosenblatt P.**, Dehant V., Verhoeven O.
The deep interior of Venus, Mars, and the Earth: A brief review and the need for planetary surface-based measurements.
Planet. Space Sci., Vol. 59, issue 10, p. 1048-1061, doi:10.1016/j.pss.2010.02.002., 2011.

[PR16] Dehant V., Le Maistre S., Rivoldini A., Yseboodt M., **Rosenblatt P.,** Van Hoolst T., Mitrovic M., Karatekin Ö., Marty J.C., and Chicarro A.
Mars' deep interior from future radioscience missions with landers and orbiters.
Planetary and Space Science, Vol. 59, issue 10, p. 1069-1081, doi:10.1016/j.pss.2010.03.014, 2011.

[PR15] Karatekin Ö, de Viron O., Lambert S.B., Dehant V., **Rosenblatt P.,** Van Hoolst T.
Atmospheric angular momentum variations of Earth, Mars and Venus at seasonal time scales.
Planetary and Space Science, Vol. 59, issue 10, p. 923-933, doi:10.1016/j.pss.2010.09.010, 2011.

[PR14] **Rosenblatt P.** and Dehant V.,
Mars geodesy, rotation and gravity.
Research in Astronomy and Astrophysics, Vol. 10, No. 8, p. 713-736, 2010.

[PR13] Andert T. P., **Rosenblatt P.**, Pätzold M., Häusler B., Dehant V., Tyler G.L., Marty J.C.
Precise mass determination and the nature of Phobos.
Geophysical Research Letters, 37, L09202, doi:10.1029/2009GL041829, 2010.

[PR12] Marty J.C., Balmino G., Duron J., **Rosenblatt P.,** Le Maistre S., Rivoldini A., Dehant V., Van Hoolst T.,
Martian gravity field model and its time variations from MGS and ODYSSEY data.
Planetary and Space Science, 57(3), pp. 350-363, DOI: 10.1016/j.pss.2009.01.004, 2009.

[PR11] Dehant V., Folkner W., Renotte E., Orban D., Asmar S., Balmino G., Barriot J.P., Benoist J., Biancale R., Biele J., Budnik F., Burger S., de Viron O., Häusler B., Karatekin Ö., Le Maistre S., Lognonné P., Menvielle M., Mitrovic M., Pätzold M., Rivoldini A., **Rosenblatt P**., Schubert G., Spohn T., Tortora P., Van Hoolst T., Witasse O.,Yseboodt M.,
Lander Radioscience for obtaining the rotation and orientation of Mars.
Planetary and Space Science, 57, pp. 1050-1067, DOI: 10.1016/j.pss.2008.08.009, 2009.

[PR10] **Rosenblatt P.,** Lainey V., Le Maistre S., Marty J.C., Dehant V., Pätzold M.,

van Hoolst T., and Häusler B.,
Accurate Mars Express orbits to improve the determination of the mass and ephemeris of the Martian moons.
Planetary and Space Science, 56, pp. 1043-1053,
DOI:10.1016/j.pss.2008.02.004, 2008.

[PR9] Rosat S., **Rosenblatt P.** Trinh A., and Dehant V.,
Mars and Mercury rotation variations from altimetry crossover data: Feasibility study.
Journal of Geophysical Research, vol. 113, E12014,
doi:10.1029/2008JE003233, 2008

[PR8] Pireaux S., Barriot J.P., **Rosenblatt P.,**
(SC)RMI: A (S)emi-(C)lassical (R)elativistic (M)otion (I)ntegrator, to model the orbits of space probes around the Earth and other planets,
Acta Astronautica, Vol. 59, pp. 517-523, DOI:
10.1016/j.actaastro.2006.04.006, 2006

[PR7] Beuthe M., **Rosenblatt P.,** Dehant V., Barriot J.-P., Pätzold M., Häusler B., Karatekin Ö, Le Maistre S., and Van Hoolst T.,
Assessment of the Martian Gravity Field at Short Wavelength with Mars Expres.,
Geophys. Res. Letters, 33, L03203, doi:10.1029/2005GL024317, 2006.

[PR6] Karatekin O., Duron J., **Rosenblatt P.,** Dehant V., Van Hoolst T., Barriot J.P.,
Martian Time-Variable Gravity and its Determination; Simulated Geodesy Experiments,
J. Geophys. Res. (Planets), 110(E6), E06001, DOI: 10.1029/2004JE002378, 2005.

[PR5] **Rosenblatt P.,** Marty J.C., Perosanz F., Barriot J.P., Van Hoolst T., Dehant V.,
Numerical simulations of a Mars geodesy network experiment: Effect of orbiter angular momentum desaturation on Mars' rotation estimation.
Planet. Space Sci., vol. 52, pp. 965-975,
doi:10.1016/j.pss.2004.07.017, 2004.

[PR4] Duron J., **Rosenblatt P.,** Yseboodt M., Karatekin O., Dehant V., Van Hoolst T**.,** J.P. Barriot,
Joint estimation of Martian C_{20} and rotation variations from simultaneous geodetic measurements : Numerical simulations of a Network Science Experiment.
Geophys. Res. Lett., DOI: 10.1029/2003GL018353, 2003.

[PR3] Barriot J.P., G. Balmino, N. Valès, **P. Rosenblatt**,
A 180th degree and order model of the Venus gravity field from Magellan line-of-sight residual Doppler data.
Geophys. Res. Lett., 25, p. 3743-3746, 1998.

[PR2] **Rosenblatt P.,** P.C. Pinet, E. Thouvenot,

Comparative hypsometric analysis of Earth and Venus.
Geophys. Res. Lett., 21, p. 465-468, 1994.

[PR1] Nieto J.L., Poulain P., Davoust E., **Rosenblatt P.,**
Isophotal shapes of early-type galaxies. I – Elongated ellipticals.
Astronomy and Astrophysics Supplement Series, vol. 88, Issue 3, p. 559-613, 1991.

4.2 Peer-Reviewed Proceedings

[P15] Thuillot W., Lainey V., Meunier L.E., Normand J.,
Arlot J.E., Dehant V., Oberst J., **Rosenblatt P.,** Vermeersen B., Dirkx D., Gurvits L., Marty J.C., Hussmann H., and the FP7-ESPaCE team, *Data mining, ingestion and distribution of planetary data on natural satellites.*
ADASS XXIV, Proceedings of a conference held on 5-9th October 2014 at Calgary, Alberta, Canada. Eds. Taylor A.R. and Rosolowsky E., San Francisco: Astronomical Society of the Pacific, pp. 583-586, 2015.

[P14] Kudryashova M., **Rosenblatt P.,** Marty J.C.,
Phobos mass estimations from MEX and Viking-1 data: Influence of different noise sources and estimation strategies. Proceedings of the Journées 2014 "Systèmes de référence spatio-temporels": Recent developments and prospects in ground-based and space astrometry, held at Pulkovo Observatory on 22nd-24th September 2014. Eds. Malkin Z. and Capitaine N., ISBN 978-5-9651-0873-2 & ISBN 978-2-901057-70-3, pp. 100-103, 2015.

[P13] Thuillot W., Lainey V., Dehant V., De Cuyper J.P.,
Arlot J.E., Gurvits L. Hussmann H., Oberst J., **Rosenblatt P.,** Marty J.C., Vermeersen B., Robert V., Dirckx D., Kudryashova M., Le Maistre S.
ESPaCE: European Satellite Partnership for Computing Ephemerides.
In: Proc. “Let’s embrace space”, Volume II, Space Research achievements under the 7th Framework Programme is published by the Space Research and Development Unit in the European Commission’s Directorate-General for Industry and Enterprise, Chapter 25, pp. 291-297, Luxembourg Publications Office of the European Union, DOI: 10.2769/31208.

[P12] Pätzold M., Tellmann S., Andert T., Carone L., Fels M.,
Schaa R., Stanzel C., Audenrieth-Kersten I., Gahr A., Müller A.-L., Stracke B., Stupar D., Walter C., Häusler B., Remus S. Selle J., Griebel H., Eidel W., Asmar S., Goltz G., Kahan D., Barriot J.-P., Dehant V., Beuthe M., **Rosenblatt P.**, Karatekin Ö, Lainey V., Tyler G.L., Hinson D., Simpson R., Twicken J. *The observations of the Mars Express orbiter Radio-Science (MaRS) experiment after one year in orbit. ESA* Scientific Publication, ESA-SP, in press, 2009.

[P11] Holmes D.P., Simpson, R., Tyler G.L., Pätzold M.,
Dehant V., **Rosenblatt P.,** Häusler B., Goltz G., Kahan D., Valencia J., and Thompson T. *The challenges and opportunities for international cooperative radio science; Experience with the Mars Express and Venus Express*

Missions. Proc. AIAA/AAS Astrodynamics Specialist Conference 18, 2008-6395, 2008.

[P10] **Rosenblatt P.**, Lainey V., Le Maistre S., Marty J.C., Dehant V., Pätzold M., Häusler B., and van Hoolst T. *Accurate Mars Express orbit determination to improve Martian Moon ephemerides***.** 2007, Proc. Société Francaise d'Astronomie et d'Astrophysique (SF2A), Grenoble, France, 2-7 July 2007.

[P9] Pireaux S., Barriot J.P., **Rosenblatt P.,** 2005, *(SC)RMI: A (s)emi-(c)lassical (r)elativistic (m)otion (i)ntegrator, to model the orbits of space probes around the Earth and other planets.* Proceedings of the IAC Space Generation Congress (Vancouver, Canada, 1-8th October 2004).

[P8] Pireaux S., Barriot J.P., **Rosenblatt P**., and Benna M., 2005, *Integrating the motion of satellites in a consistent relativistic framework: the SCRMI prototype software,* Proc. NASA Flight Mechanics Symposium, October 2005.

[P7] Karatekin O., Duron J., **Rosenblatt P.,** Dehant V., 2004, *Martian time-varying gravity field and its detection; Observations and simulations*. Proceedings of the IAG international symposium - Gravity, Geoid and Space Missions – GGSM2004 (Porto, Portugal, August 30th – September 3th) 2004.

[P6] Vienne J., Barriot J.P., **Rosenblatt P.,** Yseboodt M., Duron J., Dehant V., 2003, *Numerical simulations of the Netlander Ionosphere and Geodesy Experiment (NEIGE) : Landing site positions determination from Doppler tracking between an orbiter and landers.* Proceedings of the international workshop on planetary probe atmospheric entry and descent trajectory analysis and science, 6-9th October, Lisbon, Portugal, ESA-SP 544, 2003.

[P5] Duron J., **Rosenblatt P.,** Karatekin O., Yseboodt M., Dehant V., J., Barriot J.P., Vienne J., 2003, *Simultaneous estimate of the Martian rotation and the C_{20} gravity coefficient variations in the frame of a network science experiment.* Proceedings of the "Société Française d'Astronomie et d'Astrophysique (SF2A)", Scientific highlights 2003 (Bordeaux, France, June 16-20, 2003), Eds: F. Combes, D. Barret, T. Contini and L.Pagani, p. 59-62, 2003.

[P4] Yseboodt M., **Rosenblatt P.,** Dehant V., Barriot J.P., Van Hoolst T., 2002, *Mars Geodesy with NEIGE: Simulation of the Martian orientation parameters estimation.* Proc. 36th ESLAB Symposium - "Earth-like Planets and Moons", ESTEC, Noordwijk, 3-8 June 2002 (ESA SP-514, October 2002).

[P3] **Rosenblatt, P.,** E. Mestre, P.C. Pinet, P. Masson,

J.P. Barriot, 1998, *Géologie régionale des points chauds vénusiens présumés: Western Eistla, Bell et Ovda*. Acte du 2ème colloque national de planétologie de l'I.N.S.U., vol. 1, p. S1-24, 1998.

[P2] **Rosenblatt, P**., and P.C. Pinet, 1994,
Isostasie thermique: Implications sur la structure lithosphérique de Vénus. Acte du colloque national de planétologie de l'INSU, p. S8-27, 1994.

[P1] Pinet P.C., **P. Rosenblatt** and E. Thouvenot, 1994,
Géodynamique globale comparée de Vénus. Acte du colloque national de planétologie de l'INSU, p. S14-1, 1994.